The Application of Thin Film Ionic Self-assembled Multilayer (ISAM) Nanostructures in the Electromechanical Bending Actuators and Micro-fabricated Gas Chromatography (μGC) Devices

Dong Wang

Dissertation submitted to the faculty of the Virginia Polytechnic Institute and State University in partial fulfillment of the requirements for the degree of

Doctor of Philosophy

In

Department of Physics

James R. Heflin, Committee Chair
Harry W. Gibson
Jean J. Heremans
Hans Robinson

December 4th, 2014
Blacksburg, Virginia, USA

Keywords: Ionic Self-Assembled Multilayers, Layer-by-Layer Self-Assembled Nanostructures, Ionic Electroactive Polymeric Actuators, Microelectromechnical Gas Chromatography Devices

The Application of Thin Film Ionic Self-assembled Multilayer (ISAM) Nanostructures in the Electromechanical Bending Actuators and Micro-fabricated Gas Chromatography (μGC) Devices

Dong Wang

ABSTRACT

Ionic self-assembled multilayer (ISAM) thin film nanostructures, including highly porous and conductive gold nanoparticles (GNP), and highly porous and thermally stable silica nanoparticles (SNP), were fabricated via the layer-by-layer (LbL) self-assembly technique. Their application in ionic polymer-metal composite (IPMC) electromechanical bending actuators and microfabricated gas chromatography (μGC) devices were investigated and significant performance improvements of these devices were achieved.

IPMC bending actuators, consisting of an ionic electroactive polymer (*i*EAP) membrane as backbone, ionic liquids (IL) as electrolyte, and ISAM GNP thin film as porous electrode, were fabricated and investigated. The influences of humidity, conductive network composite (CNC), and IL uptake on the bending performance were examined and discussed. An equivalent circuit model to simulate both the electrical and mechanical responses was also proposed and experimentally verified. Moreover, IPMC actuators made from other newly synthesized *i*EAP membranes were fabricated and tested. Some of them showed promising performance that was comparable or even better as compared to the ones made from Nafion.

LbL fabricated ISAM SNPs thin film coatings were also applied in the μGC devices including micro fabricated thermal preconcentrators (μTPC) and separation columns (μSC) as adsorbent and stationary phase materials, respectively. New fabrication approaches were developed to selectively coat uniform conformal ISAM SNP coatings in these devices with different 3D microstructures. Thus, functionalized μTPCs and μSCs showed good performance, which can be further improved by using the ISAM SNPs coating as a nanotemplate for modifying additional polymer adsorbents or as the anchor sites for incorporating functional molecules for targeting detection.

Acknowledgements

The two multidisciplinary and multi-group projects I was working on during PhD study involved many collaborations with researchers in different departments at Virginia Tech and other universities. I really appreciate all the guidance, collaborations, assistance, and help I have been receiving in last five years.

First and foremost, my deepest appreciation and gratitude go to my advisor—Professor James R. Heflin. He gave me the great opportunity to work in these two very interesting and highly productive projects, and always willingly offered all the guidance, advices and supports to me on the study and research. I am so impressed by his profound knowledge in both physics and material science, as well as his acute insights and thoughtful ideas into many problems. I have learned a lot from him in critical thinking and problem solving abilities for scientific research, both theoretically and experimentally. In the meantime, Professor Heflin provided the freedom environment to me in conducting the actual research work, which would also be greatly beneficial to my future career.

Two formal students of our group working on these projects—Dr. Vaibhav Jain and Dr. Reza Montazami had given me tremendous help when I just joined the group. They were not only my colleagues, but also my mentors in guiding me through the theoretical concepts and experimental processes. Without their help, it was not possible for me to fit in the researches quickly and smoothly.

I would also like to express my deep appreciation to my dissertation committee members—Professor Harry Gibson, Professor Jean Heremans, and Professor Hans Robinson. I thank Professor Gibson for his thorough review and many valuable suggestions on my dissertation. I am grateful to Professor Heremans for all of his guidance and help in my coursework and

research. I also thank Professor Robinson for the insightful discussions and advices on my research work.

I am also very grateful to my collaborators. For the actuator project, I want to especially thank Dr. Timothy Long and his research group including Dr. Matthew Green, Dr. Renlong Gao, Dr. Tianyu Wu, and Chainika Jangu for providing newly synthesized polymer membranes for actuator studies. I would like to thank Professor Lou Madson and his research group at including Dr. Jianbo Hou, Xiaoling Wang, Ying Chen and Dr. Zhiyang Zhang for the very helpful discussions and collaborations. I thank Professor Gibson for his guidance and the collaboration with his student Terry Price. I would also like to thank the collaborators in other universities including Professor Karen Winey in University of Pennsylvania, Professor Yossef Elabd in Drexel University and Professor Ralph Colby in Pennsylvania State University and their research groups. I learned a lot and got inspired from many constructive discussions with them. Moreover, I would like to express my special appreciation to Professor Qiming Zhang and his research group in Pennsylvania State University including Dr. Yang Liu and Dr. Sheng Liu for the host and training in their lab.

For the GC project, I would like to express my deep gratitude to Professor Masoud Agah and his research group at VT MEMS LAB, for offering me the chance to take part in this great and fruitful project. I appreciate the guidance and advices from Professor Agah, and really enjoy the collaboration with his students including Hamza Shakeel, Akbar Muhammad, Dr. Shree Narayanan and Vaishnavi Srinivasaraghavan.

I thank Steve McCartney and John McIntosh at NCFL ICTAS for training me on SEM, AFM, and FIB. I appreciate Donald Leber's for his help in my work conducted in the microelectronics clean room facility. I would also like to thank Professor Robert Moore and his student Ninad Dixit and Jeremy Beach in the Department of Chemistry, Professor Eugene Joseph

and Dr. Naresh Budhavaram in the Department of Chemical Engineering, Professor Abby Whittington and her student Andre Stevenson in the Department of Material Science and Engineering, as well as Professor Michael Ellis in the Department of Mechanical Engineering for their generous help on device fabrications and characterizations.

I would also like to say thank you to the former and current members of our research group including Dr. Jason Ridley, Dr. Chalongrat Daengngam, Dr. Manpreet Kaur, Dr. Ziwei Zuo, Moataz Khalifa, Jonathan Metzman, Jeong-Ah Lee, Anna Skinner, Kelly Mccutcheon and Yanlong Li. Thank them all for the valuable helps and collaborations, interesting discussions, and a lot of fun during the last five years. Together we made our group like a family and that is one of my best memories in my life.

I am very grateful to the late Graduate Program Coordinator Mrs. Christa Thomas. She was the first people I knew and contacted here at U.S. when I was preparing for my PhD study aboard many years ago. Her warm heart gave me the feeling of family when I was far away from it. I will always miss her. And I want to thank our new coordinator Ms. Betty Wilkins, for all of her help on my academic and graduation processes.

The actuator project was supported by U.S. Army Research Office for funding the actuator project under Grant No. W911NF-07-1-0452 Ionic Liquids in Electro-Active Devices (ILEAD) MURI. The μGC project was primarily supported by the National Science Foundation (NSF), under award No. ECCS-1002279, 0925945 and No. CBET-0854242.

Finally, I want to thank my real family, for always being there to give me all the love and support, in both work and life. Thank you!

Table of Contents

List of Figures

CHAPTER 1

CHAPTER 2

CHAPTER 3

CHAPTER 4

List of Tables

List of Multimedia Files

CHAPTER 1 INTRODUCTION

1.1 Introduction

This dissertation discusses the fabrication and characterization of ionic self-assembled multilayer (ISAM) thin film nanostructures, and their application in two different projects—ionic electroactive polymer (*i*EAP) based ionic polymer-metal composite (IPMC) electromechanical bending actuators and silicon based micro electromechanical systems (MEMS) micro gas chromatography (μGC) devices.

In these studies, the ISAM nanostructures were fabricated via the layer-by-layer (LbL) self-assembly technique. While being conceptually simple, practically straightforward and economically inexpensive, the LbL self-assembly can produce ISAM thin films from a wide range of macromolecular and nanostructured materials with homogeneous distribution and fine thickness control on substrates with a variety of configurations. Using this technique, ISAM thin film gold nanoparticles (GNP) were fabricated as the conductive network composite (CNC) layers for IPMC actuators. Due to its high porosity and conductivity, the GNP CNC provides extra storage volume for the ions of the working electrolyte in the actuator, and in the meantime helps to maintain sufficient electric potential gradient for driving the ion transport. Because the bending actuation results from the imbalanced ion transportation and accumulation within the IPMC actuators, GNP CNC largely improve the actuation performance in terms of both response speed and bending amplitude. On the other hand, ISAM thin films containing silica nanoparticles (SNP) have high porosity (same as GNP) and great thermal stability, which make them ideal for the functional stationary phases in the MEMS μGC devices. While their large surface area from the high porosity greatly enhances the interaction between the gas molecules and the stationary

phases of μGC devices, the good thermal stability of SNP is crucial for the testing and application of such devices where many large temperature cycles are usually involved.

Extensive work on property investigation and performance improvement of the IPMC actuators and MEMS μGC devices were also discussed in this dissertation. For the IPMC actuators, the effect of CNC thickness, ionic liquid (IL, working electrolyte that was used to provide ions to generate mechanical response) uptake and the environmental relative humidity (RH) were investigated. A modified equivalent circuit model was proposed to account for both mechanical and electrical responses of the actuators. Good agreement was discovered among parameters of this model obtained from different experiments. For the μGC devices, ISAM SNP coatings were not only used directly as the functionalization material, but also as the nanoscale template for further polymeric adsorbent coating or anchor sites of functional polymers for targeting detection. With the use of highly porous and stable SNP coatings, the performance of the μGC devices were significantly improved.

1.2 Ionic self-assembled multilayers (ISAM)

1.2.1 Self-assembly

Just as its name implies, self-assembly refers to a process in which disordered components "automatically" form connections with each other to form a new aggregate structure in an arranged way. It happens almost everywhere in the natural world and is widely used in research and manufacturing. Self-assembly is valuable in fabricating ordered structures from the components at nano- to micro- scales. It is one of the most commonly used strategies to fabricate

nanomaterials into a diverse range of nanostructures and is therefore an important practical tool in nanoscience and technology.

As a type of bottom-up manufacturing technique, the characteristics of self-assembled composites are inherited in part from the properties of their components (shape, size, charge, electrical and thermal conductivity, etc.), and from the nature of the interaction(s) among them. Thus, tailoring the components and manipulating their interactions are essential to the application of self-assembly. The scale of the components used for self-assembly ranges from molecular,[1,2] meso (nano to micro),[3,4] and macro.[5,6] The bonding forces among them can be various noncovalent intermolecular forces including hydrogen bonds,[7,8] as well as van der Waals,[9,10] capillary,[11,12] and electrostatic[13-16] interactions.

1.2.2 Layer-by-layer (LbL) electrostatic self-assembly

While being conceptually simple, practically straightforward and economically inexpensive, LbL electrostatic self-assembly is a versatile bottom-up nanofabrication technique used to produce ionic self-assembled multilayer (ISAM) thin films from a wide range of macromolecular and nanostructured materials with homogeneous distribution and fine thickness control on substrates with a variety of configurations. Coulombic electrostatic force is the key player in LbL self-assembly: A layer of charged material "A" attracts and bonds with another material "B" carrying opposite electric charge from the surrounding environment; as more and more material "B" reaches and binds to the surface, a thin layer of "B" is formed and starts repelling any more material "B" from attaching to the surface. When sufficient material "B" completely covers the previous "A" layer, the surface charge has been reversed. Thus, by

alternately repeating this process, stacks of uniformly distributed thin layers of materials with opposite charges can be self-assembled. The thickness of each individual layers is automatically controlled by charge reversal and thus can be tailored through the surface charge manipulation by adjusting the fabrication environment (which will be discussed later in this dissertation) and the total thickness of such a structure is simply determined by the fabrication cycles.

1.2.3 ISAM thin film nanostructures

Using the LbL self-assembly technique, ISAM thin film nanostructures can be easily fabricated on the surface of substrates with a variety of configurations. In many cases, nanoscale materials (such as nanoparticles or nanotubes) were used as the "building blocks" with their oppositely-charged polymeric counterparts as the "adhesive" between two adjacent thin layers of them to electrostatically bind them together. In these cases, the nanoscale materials were usually prepared as a colloid or dispersion in a liquid, and the polymeric counterparts were chosen based on the ζ potential (a measurable electrical potential at the near surface region) of the nanoscale materials to ensure opposite charge association of those two components. The pH values of the solutions and colloids of the polyions and nanomaterials used for LbL self-assembly were usually adjusted in order to get the maximum charge difference and therefore to achieve a more efficient ISAM nanostructure deposition. With versatile fabrication processes and unique features from the combination of material properties and potential for porous nanostructures (especially important in this work), ISAM thin film nanostructures can be applied in a wide range of devices to achieve a variety of functionalities.

1.3 Ionic polymer-metal composite (IPMC) electromechanical bending actuators

1.3.1 Laminate structure of IPMC electromechanical bending actuators

The IPMC actuators studied in this dissertation consisted of five layers: an ionic electroactive polymer (*i*EAP) membrane in the middle as the ion conductive backbone, two GNP containing CNC on both sides of the membrane to provide extra storage volume for the ions of the electrolyte, and gold foils hot-pressed on both sides of the outer surface to be connected to the external power supply. All IPMC actuators studied in this dissertation were cut into 1 mm × 1 cm strips for testing. The final five-layer laminate structure is illustrated in Figure 1.1.

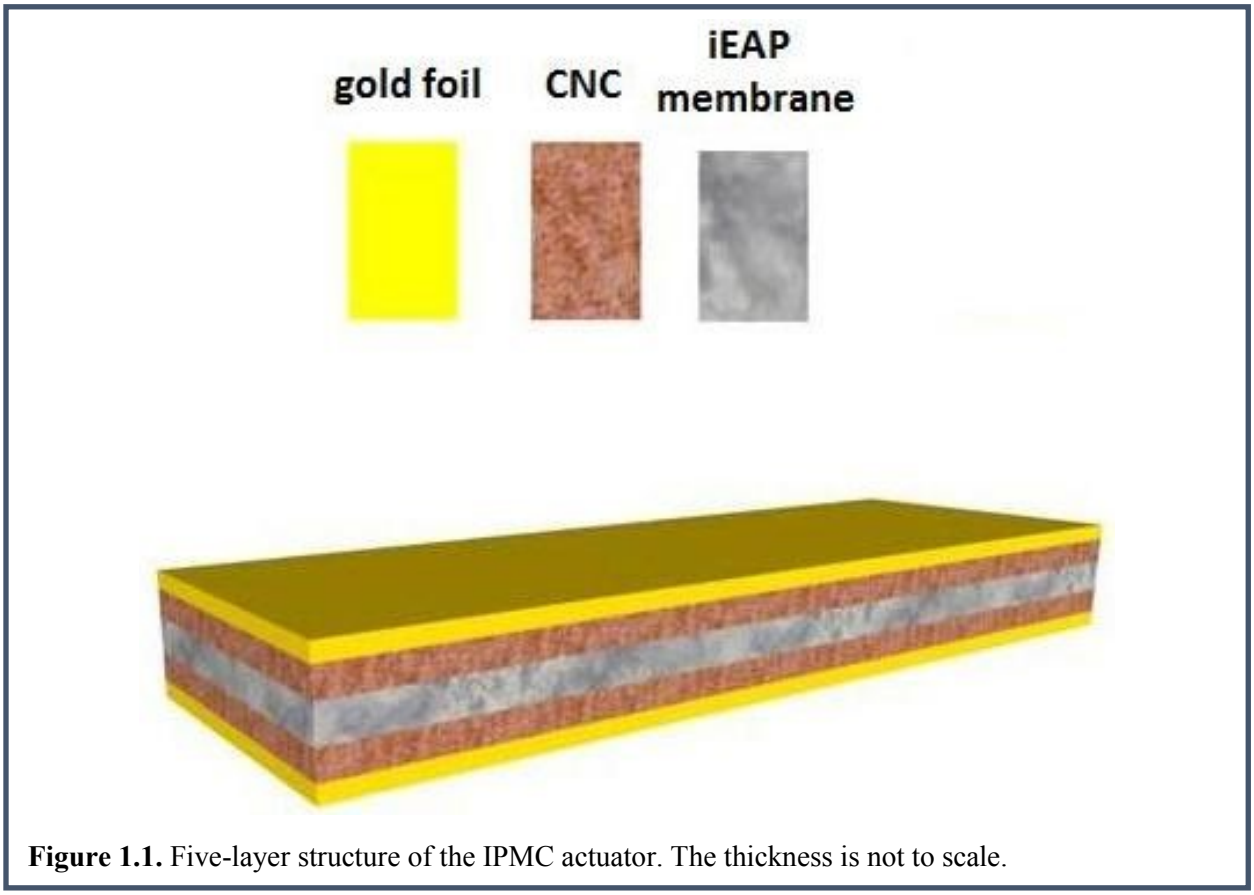

Figure 1.1. Five-layer structure of the IPMC actuator. The thickness is not to scale.

1.3.2 Ionic electroactive polymers (iEAPs)

As a major focus of so-called "smart materials", electroactive polymers (EAPs) can either experience mechanical response under an electrical stimulus as an actuator, or vice versa as a sensor, or both. Unlike traditional electroactive materials, such as ceramic piezoelectric materials and shape memory alloys,[17,18] these polymers are typically lightweight, low-cost, and more flexible and bio-compatible, all of which has led to some researchers to refer these polymers as "artificial muscles". They have promising potential applications as sensors, actuators, robotic components and other MEMS devices. The EAPs can be divided into two main categories: electronic and ionic. The electronic EAPs generally include dielectric elastomers and piezoelectric polymers. When an external electric field is applied, dielectric elastomers expand due to the electrostatic attraction between the two sides of the polymer.[19] The internal polarization of piezoelectric polymers [(primarily poly(vinylidene fluoride) or PVDF family polymers) can be enhanced or reduced by an external electric field in the same or opposite polarization direction, respectively. The resulting change of the distance between the polarized side groups on the polymer chain causes the change in length of the polymer along the polarization direction.[20]

Although electronic EAPs have an advantage in the speed of the response and the capability of being operated in ambient environment, they usually require high operation voltages and generate small actuation amplitudes. In comparison, another group of EAPs—ionic EAPs or *i*EAPs (which include conductive polymers,[21,22] ionic polymer gels,[23,24] CNTs,[25,26] and ionic polymer-metal composites (IPMCs)) deform as a result of the ionic motion within the polymer, and much lower voltage (<10 V) is needed to generate high elastic energy densities.[27-29] Within all the types of *i*EAPs, IPMCs have especially attracted increased attention because of the

large strain they generate and their versatility brought in by the combination of ion conductive polymers as a working backbone and noble metal as an electrode. Recent developments targeting novel electrolytes,[30-32] electrode materials,[33] and optimized polymer backbones[34-37] have reduced many of the limitations constraining their application as actuators. These efforts make the IPMC a very promising candidate for electromechanical actuator applications.

1.3.3 Conductive network composite (CNC)

The mechanical bending of IPMC actuators results from the imbalanced ion accumulation near the surface of one or both sides. Intuitively, the more ions reach to and store in the surface region, the larger bending performance that can be obtained. The simplest form of an IPMC actuator is a polymeric membrane directly sandwiched between two planar outer electrodes connected to the input circuit. Under the effect of the external electric field, the motion and accumulation of the ions, either the counterions of the charged side groups on the polymer chains or the exchanged ions, results in the bending actuation.[38] However, such a configuration suffers from limited bending amplitude due to insufficient ion accumulation near the electrode interface, which is caused by the screening effect wherein the accumulated ions along the electrode interface repel more ions from moving into that region. As a result, only a thin layer of the ions with a thickness of about a Debye length along the electrode surface can contribute to the bending actuation, as depicted in Figure 1.2. This is also confirmed by the discovery that the bending actuation is proportional to the capacitance of the actuator, a larger capacitance means more ion (charge) separation and accumulation.[39] As a result, the bending performance of IPMC actuators directly relates to the total effective surface area of the electrode.

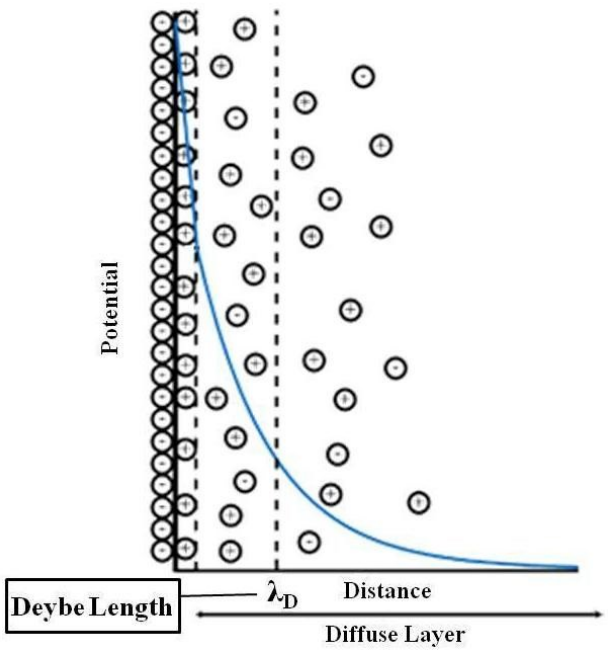

Figure 1.2. Ions accumulate within the region defined by Deybe Length along the planar electrode.

To overcome this limitation, a micro- to nano- structured CNC can be fabricated on both sides of the *i*EAP membrane as porous electrodes with high surface area working as a reservoir to enhance the accumulation of the ions. Due to its high porosity and good conductivity, a CNC provides extra storage volume for the ions of the working electrolyte in the IPMC actuators, and at the same time helps to maintain sufficient potential gradient for driving the ion transport. As a result, the bending performance can be largely enhanced.

1.3.4 Outer electrodes

A thin coating of materials with very high conductivity was applied to the very outer surface of both sides of IPMC actuator to act as the outer electrodes to be connected to the external power source. During testing, one tip of an IPMC actuator was clamped between the anode and cathode of the external circuit connecting to the power source while the other tip is

left free to move. So these outer electrodes guaranteed good connection between the external circuit and the IPMC actuator and in the meantime generated an electric field in the thickness direction that was evenly distributed from tip to tip.

1.3.5 Ionic liquids (ILs)

Recently, a novel type of electrolyte has been recognized and is quickly becoming popular in a wide range of traditional electrolyte-based studies and applications, including electroplating, fuel cells, electric double layer capacitors, sensors and actuators.[40-42] Room temperature ionic liquids, or ionic liquids (ILs) for short, are salts with low melting point so that they are in liquid form under room temperature. In other words, it is a "pure" electrolyte without solvent and is ideal for the IPMC actuator application due to its good ionic conductivity and thermal stability, high electrochemical window (can be higher than 4 V) and usually negligible vapor pressure. In addition, they usually consist of large organic ions which would be beneficial in promoting the bending efficiency. More attractively, the IL compound can be tailored easily and thus result in countless combinations of cations and anions, to obtain desirable properties to accommodate a variety of requirements and applications.[32]

1.4 Microelectromechanical systems (MEMS) gas chromatography (GC) devices

1.4.1 MEMS GC

Gas chromatography (GC) is an analytical technique to separate and independently detect the components of a mixture of volatile and/or semi-volatile organic compounds in their gas

phase. A modern GC system typically consists of a sample injector, a preconcentrator (optional), a separation column in a temperature controlled GC oven, a detector, and data acquisition and analysis equipment(s).[43] As schematically described in Figure 1.3, the mixture is first introduced into the sample injector either completely or partially (sample splitting), where it starts being transported through the system by a carrier gas, which is usually an inert gas such as nitrogen or helium. The preconcentrator then collects the sample over a time period to concentrate the analytes before introducing them into the GC column for separation. When travelling through the separation column, the mixed analytes are separated into individual components because of their different elution rate caused by differences in their interaction with the stationary phase. Finally, the separated components are picked up by the detector, such as a flame ionization detector (FID) or thermal conductivity detector (TCD), and signals in the form of discrete peaks representing the individual components are generated and acquired for further analysis.[43]

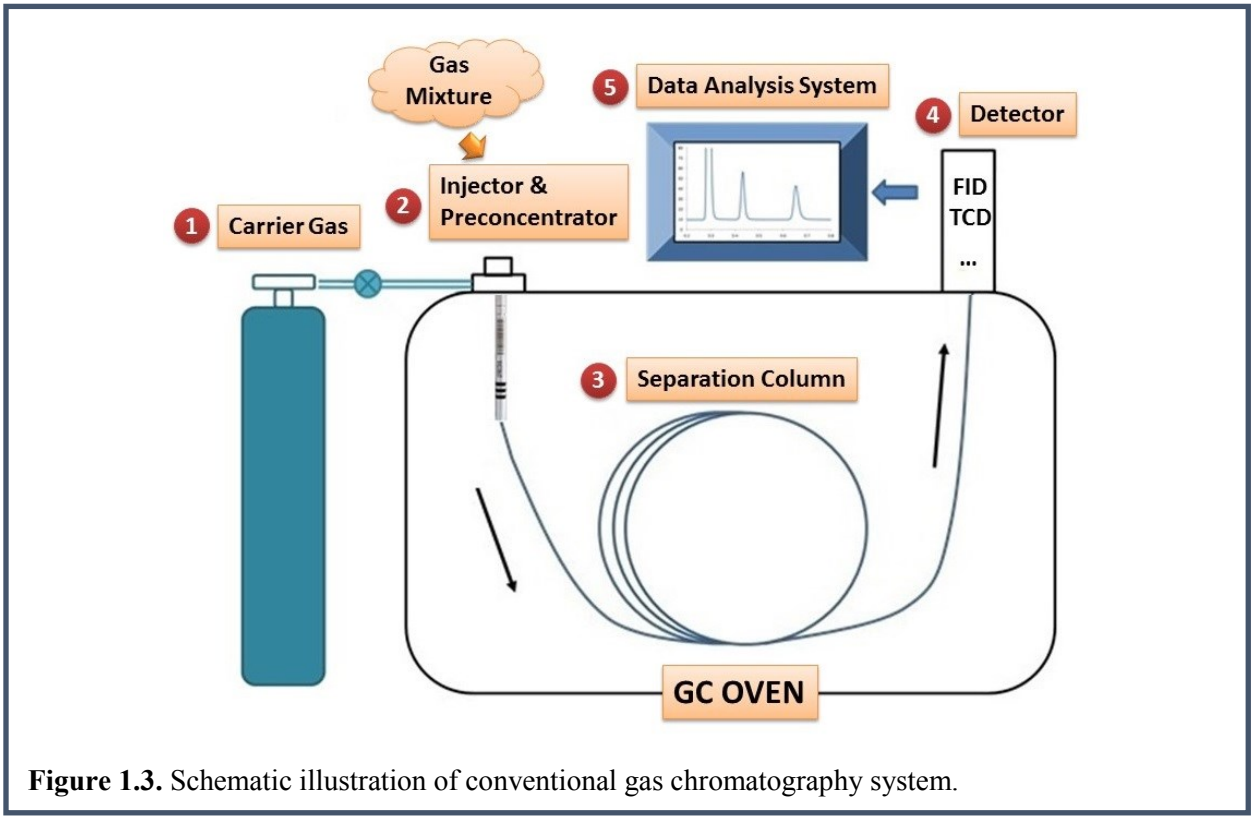

Figure 1.3. Schematic illustration of conventional gas chromatography system.

However, conventional bench-top GC systems are cumbersome and expensive, as well as time and energy consuming. Due to recent advancements and emergence of microelectromechanical systems (MEMS), energy-efficient integrated micro gas chromatography (μGC) systems have attracted considerable attention. Moreover, by etching the micro-preconcentrator, micro-separation column, integrated heating element and detector in a single silicon chip, "lab-on-a-chip" μGC systems with temperature programming ability are achieved.[44] This system upon complete realization could expand the range of applications for real-time and rapid on-site analysis at a lower cost, and thus could be widely used in air quality monitoring, breath analysis, hazardous chemical detection, forensic analysis etc.[45-54] Figure 1.4 shows a couple of silicon-based μGC devices that were used in the current study as an example.

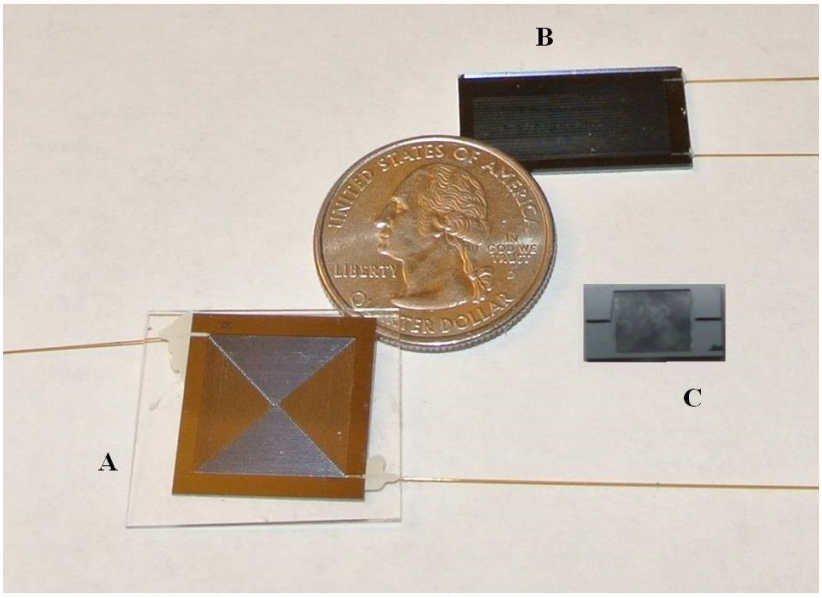

Figure 1.4. Photo of the μGC devices fabricated and used in this study: (A) Single capillary separation column; (B) Multi capillary separation column; (C) Micro thermal preconcentrator. Their sizes are compared to a US quarter coin.

1.4.2 Micro thermal preconcentrator (μTPC)

The preconcentration of the analytes by trapping or adsorbing the target gas molecules on the adsorbent phase over a period of time can significantly enhance the performance of GC system. This collection process accumulates the target analytes and eliminates interference from other irrelevant components in the gas mixture. It thus generates a highly concentrated analyte "plug" for the following GC separation column and significantly enhances the detection limit and helps to generate sharper and more distinctly separated peaks. To achieve effective adsorbance, an adsorbent with a porous structure and large surface area is highly desired.[55] The selectivity of the target gas molecules can also be achieved by carefully selecting an adsorbent that would only or preferentially trap the target gas molecules.[56]

A MEMS-based micro thermal pre-concentrator (μTPC) consists of an etched cavity in a silicon chip filled with adsorbent material. The chip cavity is then sealed by bonding it to another substrate, with heaters and sensors deposited or attached on the backside of the chip afterwards. Analytes are typically desorbed from a μTPC in the form of a sharp sample plug via controlled thermal desorption.

1.4.3 Micro separation column (μSC)

The separation column is the "heart" of the GC system, which is basically a long "channel" for gas to flow through and in which the gas components of the mixture in the carrier gas (mobile phase) interact with the functional material inside the column (stationary phase). When the mobile phase is introduced into the column, the different mass transfer rates between the components in the mobile phase and the stationary phase results in the difference in time that the

individual constituents take to migrate through the column, and thus the components of the mixture are separately eluted.

By utilizing microfabrication approaches including wet chemical,[57,58] laser,[59,60] and plasma etching techniques,[60-62] miniaturized GC columns can be achieved by etching channels in silicon, metal and polymer substrates. More recently, a series of high-aspect-ratio (HAR) rectangular μGC column designs, including the nail-sized etched square[63,64] and spiral[65] channel structures etched in a silicon wafer were developed and tested. Besides the single channel design, multi-capillary,[64,66,67] and semi-packed[68,69] μGC column configurations were also developed in order to further enhance the separation efficiency.

1.5 Document Organization

The rest of the dissertation is structured as follows.

Chapter 2 provides an overview and literature review of the major topics covered in this dissertation. First, the fabrication and application of ISAM nanostructures will be discussed in detail, including the fabrication technique—LbL self-assembly, as well as a wide variety of ISAMs made of different nanomaterials with unique properties, and their applications reported in the literatures. Next, an overview of the development of the key components of an IPMC actuator are presented, including different types of *i*EAPs for the actuator application, the fabrication and characterization of CNCs with varied constituents and structure, and the development and incorporation of novel IL electrolytes. In the last part, the general features of a MEMS GC system are discussed, different designs of μTPCs and μSCs are presented, and commonly used adsorbent and functional materials in these devices are reviewed.

Chapter 3 reports the fabrication of ISAM GNP thin films and their application in IPMC actuators as CNC layers. For the IPMC actuator fabrication, an improved apparatus used in the LbL process was found to achieve better quality ISAM GNP thin films, as well as improved time and cost efficiency. The factors that affect IL incorporation rate were also discussed. A unique bidirectional bending behavior was revealed and modeled with microscopic ion transport and accumulation. The dependences of electrical and mechanical responses of the IPMC actuator to an external DC voltage input on CNC thickness, IL uptake and ambient humidity were investigated. A modified equivalent circuit model of IPMC actuators was then proposed to account for these correlations and general agreements between key fitting parameters from different measurements were obtained. Moreover, the correlation between microscopic ion diffusion coefficients and macroscopic bending performance was also directly demonstrated. Finally, IPMC actuators from other newly synthesized *i*EAPs were also fabricated and tested. Some of them showed comparable or even better performance than the ones made from widely used Nafion.

In Chapter 4, a new approach for selective deposition of ISAM SNP thin films in the micro 3D structures of μGC devices is reported. By combining the LbL self-assembly and photolithography, uniform and robust ISAM SNP coatings were achieved conformally on the inner surface of the micro 3D structures with good repeatability and thickness consistency. In the μTPCs, ISAM SNP were either used directly as the adsorbent or as the nanotemplate to generate novel nanostructuring of a conventional polymer adsorbent. The increase of surface area of the polymer adsorbent resulted in greatly enhanced adsorption capacity of μTPCs. Besides, ISAM SNP thin films incorporated into μSCs with multiple designs were demonstrated to show good separation capability of micro gas components with a wide range of boiling points. The

consistency and durability of the devices were also tested and confirmed. Especially, an alternate approach for conducting LbL fabrication was used for very narrow channels in μSCs and successfully generated an ISAM SNP coating with equally high quality. A preliminary study using an ISAM GNP coating for incorporating a thiol stationary phase for μSC was also presented.

The major studies and achievements reported in this dissertation are summarized in Chapter 5, and suggested future work including improvement in device fabrication, exploration of new materials used for ISAM fabrication, and more complete probing of the devices from different perspectives are also discussed.

References

1 P. T. Tanev and T. J. Pinnavaia, *Science* **267,** 865 (1995).

2 J. R. Heflin, C. Figura, D. Marciu, Y. Liu, and R. O. Claus, *Applied Physics Letters* **74,** 495 (1999).

3 S. E. Yancey, W. Zhong, J. R. Heflin, and A. L. Ritter, *Journal of Applied Physics* **99,** 034313 (2006).

4 D. H. Gracias, V. Kavthekar, J. C. Love, K. E. Paul, and G. M. Whitesides, *Advanced Materials* **14,** 235 (2002).

5 K. Chen, C. Durak, J. R. Heflin, and H. D. Robinson, *Nano Letters* **7,** 254 (2007).

6 G. S. Zhu, S. L. Qiu, F. F. Gao, D. S. Li, Y. F. Li, R. W. Wang, B. Gao, B. S. Li, Y. H. Guo, R. R. Xu, Z. Liu, and O. Terasaki, *Journal of Materials Chemistry* **11,** 1687 (2001).

7 W. B. Stockton and M. F. Rubner, *Macromolecules* **30,** 2717 (1997).

8 R. S. Pontes, M. Raposo, C. S. Camilo, A. Dhanabalan, M. Ferreira, and O. N. Oliveira, *Physica Status Solidi a-Applied Research* **173,** 41 (1999).

9 P. N. Dickerson, A. M. Hibberd, N. Oncel, and S. L. Bernasek, *Langmuir* **26,** 18155 (2010).

10 Y. Zhao and Z. Hu, *The Journal of Physical Chemistry B* **117,** 10540 (2013).

11 U. Srinivasan, D. Liepmann, and R. T. Howe, *Microelectromechanical Systems, Journal of* **10,** 17 (2001).

12 N. Bowden, I. S. Choi, B. A. Grzybowski, and G. M. Whitesides, *Journal of the American Chemical Society* **121,** 5373 (1999).

13 J. H. Cheung, W. B. Stockton, and M. F. Rubner, *Macromolecules* **30,** 2712 (1997).

14 F. Caruso, H. Lichtenfeld, E. Donath, and H. Mohwald, *Macromolecules* **32,** 2317 (1999).

15 T. Serizawa, H. Takeshita, and M. Akashi, *Langmuir* **14,** 4088 (1998).

16 V. Jain, H. M. Yochum, R. Montazami, J. R. Heflin, L. Hu, and G. Gruner, *Journal of Applied Physics* **103** (2008).

17 J. E. Huber, N. A. Fleck, and M. F. Ashby, *Proceedings: Mathematical, Physical and Engineering Sciences* **453,** 2185 (1997).

18 I. W. Hunter and S. Lafontaine, in *A comparison of muscle with artificial actuators*, 1992, p. 178.

19 R. Pelrine, R. Kornbluh, Q. B. Pei, and J. Joseph, *Science* **287,** 836 (2000).

20 Q. M. Zhang, V. Bharti, and X. Zhao, *Science* **280,** 2101 (1998).

21 M. R. Gandhi, P. Murray, G. M. Spinks, and G. G. Wallace, *Synthetic Metals* **73,** 247 (1995).

22 T. F. Otero and J. M. Sansinena, *Advanced Materials* **10,** 491 (1998).

23 Z. S. Liu and P. Calvert, *Advanced Materials* **12,** 288 (2000).

24 T. Hirai, J. M. Zheng, and M. Watanabe, in *Smart Structures and Materials 1999: Electroactive Polymer Actuators and Devices*; *Vol. 3669*, edited by Y. BarCohen (1999), p. 209.

25 R. H. Baughman, C. Cui, A. A. Zakhidov, Z. Iqbal, J. N. Barisci, G. M. Spinks, G. G. Wallace, A. Mazzoldi, D. De Rossi, A. G. Rinzler, O. Jaschinski, S. Roth, and M. Kertesz, *Science* **284,** 1340 (1999).

26 A. M. Fennimore, T. D. Yuzvinsky, W.-Q. Han, M. S. Fuhrer, J. Cumings, and A. Zettl, *Nature* **424,** 408 (2003).

27 Y. Bar-Cohen, S. Sherrit, and S. S. Lih, in *Smart Structures and Materials 2001: Electroactive Polymer Actuators and Devices*; *Vol. 4329*, edited by Y. BarCohen (2001), p. 319.

28 K. M. Newbury and D. J. Leo, *Journal of Intelligent Material Systems and Structures* **13,** 51 (2002).

29 S. Nemat-Nasser and J. Y. Li, *Journal of Applied Physics* **87,** 3321 (2000).

30 S. Nemat-Nasser, *Journal of Applied Physics* **92,** 2899 (2002).

31 M. Shahinpoor and K. J. Kim, *Applied Physics Letters* **80,** 3445 (2002).

32 M. D. Bennett and D. J. Leo, *Sensors and Actuators a-Physical* **115,** 79 (2004).

33 N. Fujiwara, K. Asaka, Y. Nishimura, K. Oguro, and E. Torikai, *Chemistry of Materials* **12,** 1750 (2000).

34 R. Gao, D. Wang, J. R. Heflin, and T. E. Long, *Journal of Materials Chemistry* **22,** 13473 (2012).

35 M. D. Green, D. Wang, S. T. Hemp, J.-H. Choi, K. I. Winey, J. R. Heflin, and T. E. Long, *Polymer* **53,** 3677 (2012).

36 T. Wu, D. Wang, M. Zhang, J. R. Heflin, R. B. Moore, and T. E. Long, *Acs Applied Materials & Interfaces* **4,** 6552 (2012).

37 C. Jangu, J.-H. H. Wang, D. Wang, S. Sharick, J. R. Heflin, K. I. Winey, R. H. Colby, and T. E. Long, *Macromolecular Chemistry and Physics* **215,** 1319 (2014).

38 M. Shahinpoor, Y. Bar-Cohen, J. O. Simpson, and J. Smith, *Smart Materials & Structures* **7,** R15 (1998).

39 B. J. Akle, D. J. Leo, M. A. Hickner, and J. E. McGrath, *Journal of Materials Science* **40,** 3715 (2005).

40 M. Galinski, A. Lewandowski, and I. Stepniak, *Electrochimica Acta* **51,** 5567 (2006).

41 R. Hagiwara and J. S. Lee, *Electrochemistry* **75,** 23 (2007).

42 M. Armand, F. Endres, D. R. MacFarlane, H. Ohno, and B. Scrosati, *Nat Mater* **8,** 621 (2009).

43 C. F. Poole, *Gas chromatography* (Elsevier, Amsterdam; Boston, 2012).

44 S. Narayanan, B. Alfeeli, and M. Agah, *Ieee Sensors Journal* **12** (2012).

45 K. Reddy, Y. Guo, J. Liu, W. Lee, M. K. Khaing Oo, and X. Fan, *Lab on a Chip* **12,** 901 (2012).

46 R.-S. Jian, R.-X. Huang, and C.-J. Lu, *Talanta* **88,** 160 (2012).

47 H. Shakeel, G. Rice, and M. Agah, in *First reconfigurable MEMS separation columns for micro gas chromatography*, Paris, France, 2012, p. 823.

48 S. Narayanan, B. Alfeeli, and M. Agah, *IEEE Sensors Journal* **12,** 1893 (2012).

49 G. Serrano, D. Paul, S.-J. Kim, K. Kurabayashi, and E. T. Zellers, *Analytical chemistry* **84,** 6973 (2012).

50 J. A. Potkay, G. R. Lambertus, R. D. Sacks, and K. D. Wise, *IEEE Journal of Microelectromechanical Systems* **16,** 1071 (2007).

51 P. R. Lewis, R. P. Manginell, D. R. Adkins, R. J. Kottenstette, D. R. Wheeler, S. S. Sokolowski, D. E. Trudell, J. E. Byrnes, M. Okandan, J. M. Bauer, R. G. Manley, and C. Frye-Mason, *IEEE Sensors Journal* **6,** 784 (2006).

52 A. D. Radadia, R. I. Masel, M. A. Shannon, J. P. Jerrell, and K. R. Cadwallader, *Analytical Chemistry* **80,** 4087 (2008).

53 R. Manginell, J. Bauer, M. Moorman, L. Sanchez, J. Anderson, J. Whiting, D. Porter, D. Copic, and K. Achyuthan, *Sensors* **11,** 6517 (2011).

54 B. C. Kaanta, H. Chen, and X. Zhang, *Journal of Micromechanics and Microengineering* **20,** 055016 (2010).

55 K. Dettmer and W. Engewald, *Analytical and Bioanalytical Chemistry* **373,** 490 (2002).

56 J.-R. Li, R. J. Kuppler, and H.-C. Zhou, *Chemical Society Reviews* **38,** 1477 (2009).

57 C. M. Yu, *High performance hand-held gas chromatograph* (1998).

58 E. S. Kolesar and R. R. Reston, *Ieee Transactions on Components Packaging and Manufacturing Technology Part B-Advanced Packaging* **21,** 324 (1998).

59 M. L. Ngan, K. C. Lee, and K. W. Cheah, *Journal of Applied Physics* **83,** 1637 (1998).

60 H. S. Noh, P. J. Hesketh, and G. C. Frye-Mason, *Journal of Microelectromechanical Systems* **11,** 718 (2002).

61 G. Frye-Mason, R. Kottenstette, P. Lewis, E. Heller, R. Manginell, D. Adkins, G. Dulleck, D. Martinez, D. Sasaki, C. Mowry, C. Matzke, and L. Anderson, *Hand-held miniature chemical analysis system (mu ChemLab) for detection of trace concentrations of gas phase analytes* (2000).

62 C. M. Matzke, R. J. Kottenstette, S. A. Casalnuovo, G. C. Frye-Mason, M. L. Hudson, D. Y. Sasaki, R. P. Manginell, and C. C. Wong, in *Micromachining and Microfabrication Process Technology Iv*; *Vol. 3511*, edited by J. H. Smith (1998), p. 262.

63 G. Lambertus, A. Elstro, K. Sensenig, J. Potkay, M. Agah, S. Scheuering, K. Wise, F. Dorman, and R. Sacks, *Analytical Chemistry* **76,** 2629 (2004).

64 D. Wang, H. Shakeel, J. Lovette, G. W. Rice, J. R. Heflin, and M. Agah, *Analytical Chemistry* **85,** 8135 (2013).

65 P. R. Lewis, R. P. Manginell, D. R. Adkins, R. J. Kottenstette, D. R. Wheeler, S. S. Sokolowski, D. E. Trudell, J. E. Byrnes, M. Okandan, J. M. Bauer, R. G. Manley, and G. C. Frye-Mason, *Ieee Sensors Journal* **6,** 784 (2006).

66 M. A. Zarejan-Jahromi, M. Ashraf-Khorassani, L. T. Taylor, and M. Agah, *Journal of Microelectromechanical Systems* **18,** 28 (2009).

67 M. A. Zareian-Jahromi and M. Agah, *Journal of Microelectromechanical Systems* **19,** 294 (2010).

68 T. Nakai, S. Nishiyama, M. Shuzo, J. J. Delaunay, and I. Yamada, *Journal of Micromechanics and Microengineering* **19** (2009).

69 S. Ali, M. Ashraf-Khorassani, L. T. Taylor, and M. Agah, *Sensors and Actuators B-Chemical* **141,** 309 (2009).

CHAPTER 2 BACKGROUND AND LITERATURE REVIEW

2.1 Ionic self-assembled multilayers (ISAM)

2.1.1 Self-assembly

Self-assembly can be found almost everywhere around us, and one of the most prevalent self-assembly processes occurs in our body and within all other life forms—mitosis; the structure and components of a cell are replicated and assembled into another cell. It is the biological basis of most living forms. The formation of proteins based on genetic sequences in DNA is another prime example of biological self-assembly. Moreover, as small as bacterial colonies,[1] or as large as insect swarms and fish schools,[2,3] many biological systems at different scales involve self-assembly processes, in which large numbers of components dynamically aggregate to form groups with certain structures and functions. Beyond the domain of biology, such types of self-assembly can be found at even larger scales. The formation of weather patterns, stellar systems and even the galaxies are the result of such prominent processes.

In all of the aforementioned processes, an energy dissipation is always associated with the system throughout its formation and existence and they are thus called "dynamic self-assembly."[4-6] Seemingly universal though, dynamic self-assembly is less studied because of the lack of practical controllability over the parameters that determine the nature and behavior of the components, and the interaction between them, and thus over the structure and properties of the resulting aggregates.[7]

On the contrary, if the resulting aggregate structure or system eventually reaches an equilibrium state with no further energy dissipation, such process is so-called static self-assembly (which will be simply referred to as self-assembly hereafter) and has been extensively

studied.[8-12] To make the self-assembly process feasible, its components must be able to move freely to interact and aggregate, so it is usually performed in a liquid or vapor environment. In those cases where the self-assembly occurs on a substrate, the surface of the substrate needs to be reasonably smooth to ensure effective bonding. Moreover, some equilibrium state must be achieved between the components of the free phase and the assembled phase for self-control, and the components should have the ability to self-arrange to target and bond to certain locations in order to obtain the desired ordered structure. By applying appropriate templates and/or boundary conditions, further control and manipulation of the assembled structure can be achieved.

Those requirements can be fulfilled primarily by two different approaches. One is called the "self-assembled monolayer" or SAM. It usually involves weak hydrogen or van der Waals bonds or stronger dative bonds between the constituent molecules and the surface of substrate. Two of the most popular SAM systems are silanes on silicon and silica[13,14] and thiols on gold.[15,16] These long alkyl chain organic molecules have a reactive head group that chemically bonds to the surface group of the substrate and a variety of tail groups can be chosen to get desired physical and chemical properties of the SAM coatings. These two parts are connected with an alkylene chain in the middle whose length has significant effects on the mechanical properties of the SAM. For example, silanes can interact with the hydroxyl group (-OH) usually found on silicon and silica surfaces to form a Si-O-Si bond; and the sulfur-gold (S-Au) interaction forms a bond between thiols (sulfhydryl headgroup, -C-SH) and a gold surface to make SAMs of thiols, one of the most widely studied self-assembled organic molecules on metal surfaces.

The incorporation of SAM layers provides feasibility in surface property modification and functionalization with different functional groups.[17] For instance, Towrfe *et al*.[18] studied the

incorporation of SAMs of organic silanes including 3-aminopropyltriethoxysilane (APTES), triethoxysilylpropyl succinic anhydride (TESPSA) and glycidoxypropyl trimethoxysilane (GPTMS) on oxidized silicon wafers to create amine ($-NH_2$), carboxyl (-COOH) and hydroxyl (-OH) functionalized surfaces, respectively. These functional groups act as the nucleation sites for the low temperature precipitation of a calcium phosphate (Ca-P) layer to mimic the precipitation of calcium and phosphate in bone formation. Moreover, by functionalizing a GNP with a SAM of 4-methylbenzenethiol, 1-hexanethiol and 1-dodecanethiol, Hanwell *et al*.[19] established an approach to sensitively probe gas and vapor concentrations. Because the conductivity of the insulating thiol/air gap between the GNP is highly dependent on the separation and the permittivity of such medium between the nanoparticles, the conductivity of the thin film layers containing SAM thiol encapsulated GNP are very sensitive to the environmental change caused by the fluctuation of gas and vapor concentration. In this dissertation, thin film SAM silanes and thiols were also applied as the surface deactivation layers on the ISAM SNP, and as a stationary phase coating on the ISAM GNP in the μSCs. More detailed information will be mentioned in the later parts of this dissertation.

Widely used though, a SAM has a limitation in fabrication of multilayer structures. Another approach involves the non-covalent electrostatic self-assembly and has the ability to deposit coatings with a large number of stacked multilayers on surfaces with more general profiles, both chemically and geometrically. It is the method used throughout the studies reported in this dissertation.

2.1.2 LbL electrostatic self-assembly for ISAM thin film fabrication

Developed first in 1991 by Decher *et al*.,[20,21] the LbL method is used to fabricate ISAM thin films, which have a wide range of applications including electromechanical actuators,[22-26] chemical and biological sensors,[27-33] optical[34-38] and electrochromic devices.[39-45]

In short, by alternately exposing the substrate to oppositely-charged materials (usually two but can be multiple different materials) in a fluid environment, which is essential to ensure sufficient material-substrate and material-material interactions, LbL thin films of the materials are electrostatically bound together and can be built up to very large numbers of multilayers (a pair of such layers is referred as one bilayer or BL). Thorough rinsing in between each deposition step washes away excess material from the previous stage, while leaving enough surface charge for the next material to be electrostatically deposited and bonded. Thus, uniform, dense, and robust stacks of layers can be deposited conformally on the substrates with a wide variety of surface characteristics and configurations. A desired total film thickness can be achieved by simply terminating the procedure after the completion of a certain number of bilayers (BLs). It was also found that, by adjusting the pH of the solutions, not only the thickness of the individual layers can be tailored, but also the properties of the assembled thin films including the interpenetration between the layers and the surface composition.[46-48] Besides, more complicated and even novel 3-D structures can be built via LbL self-assembly with the assistance of templates and carefully designed fabrication procedures, which have opened an even wider range of applications of this technique.[49-51]

In recent years, mesoscale (nano- to micro-sized spheres or particles) LbL self-assembly has attracted more and more attention along with exploding research in the areas of synthesis, functionalization, assembly and application of nanoparticles and nanostructures. The resulting

uniform and dense ISAM thin films of nanoscaled materials can be fabricated with fine thickness control (down to a single layer of the components—nanoscale), and have the unique properties (electrical, optical or thermal) and structures of the nanoscaled components incorporated within. For instance, ISAM thin films containing carbon nanotubes (CNT),[52,53] GNP[54] and SNP[55,56] have been deposited via LbL self-assembly on flat as well as etched micro-fluidic surfaces[57,58] for diverse nanotechnology-driven applications. A more detailed description of these ISAM nanostructures and their application can be found in next section. As an example, a schematic illustration of the LbL self-assembly of ISAM nanoparticles (NP) with poly(allylamine hydrochloride) (PAH) polycation used as intermediate bonding layers on a planar substrate is illustrated in Figure 2.1. Figure 2.2 shows images of the automatic dipping system used for fabricating the ISAM thin film nanostructures reported in this dissertation.

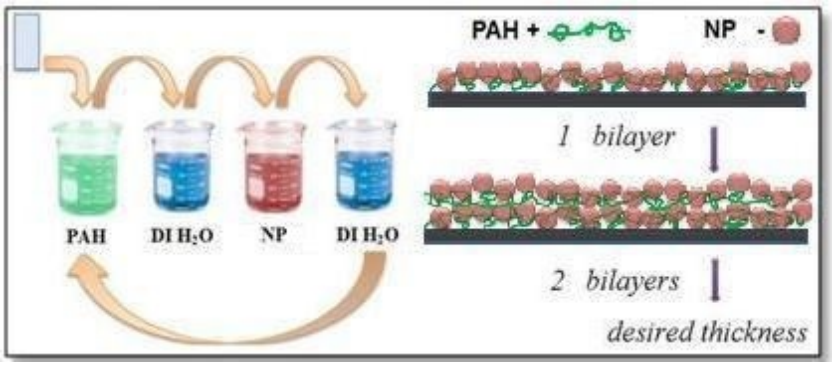

Figure 2.1. Schematic demonstration of LbL self-assembly of nanoparticles (NP) on a substrate. The polycation used here is poly(allylamine hydrochloride) (PAH), an inactive, long-chain polymer.

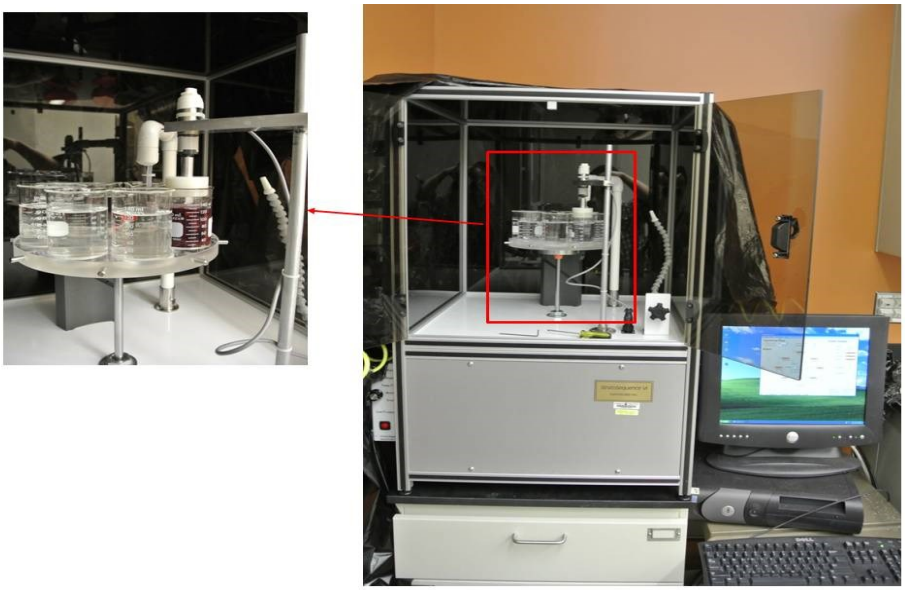

Figure 2.2. Photos of the automatic dipping system (StratoSequence VI Robot, nanoStrata Inc.) used for the LbL thin film ISAM nanostructure fabrication.

2.1.3 ISAM thin film nano/micro structures

As discussed in the last section, by simply utilizing electrostatic interactions, ISAM thin film nano/micro structures can be easily fabricated using the LbL self-assembly technique. It is a powerful approach to create novel nanostructures (either "pure" or "hybrid", based on the materials used for LbL fabrication) with a wide range of applications.

For example, Kotov *et al*.[59] reported the LbL fabrication of ISAM thin films made from a series of negatively-charged semiconductor nanoparticles, including lead sulfide (PbS), titanium dioxide (TiO_2), cadmium sulfide (CdS), or their combinations. They demonstrated the successful deposition of these thin film ISAM nanostructures on a variety of substrates. Cationic poly(diallylmethylammonium chloride) was used as the intermediate "adhesive" layers in between the negatively-charged nanoparticle layers because it was found to adhere strongly to the different substrates they used, including quartz, ITO glass, mica, platinum and gold. This

study demonstrates the impressive versatility and flexibility of the ISAM composition and substrate applicability.

Using the LbL technique, Dotzauer *et al*.[60] developed a convenient way to produce porous catalytic membranes by depositing ISAM films of polyelectrolytes and GNP on the internal pore surface. They first deposited a layer of poly(acrylic acid) (PAA) polyanion on the inner pore surface of an alumina membrane with 0.2 μm diameter pores by flowing the PAA solution through the membrane. This step reverses the surface charge on the substrate from the original positive to negative. Then, using the same method, 1~3 BL of ISAM of PAH polycation and GNP with negative surface charge were deposited on the previous PAA layer by repeatedly flowing the solution or solutions of the corresponding material through the membrane, as shown in Figure 2.3. The porous aluminum membrane with GNP immobilized on the internal surface of the pore structures showed highly efficient catalytic ability, due to the very large surface area of the GNP and high catalytic activity that bulk gold does not have. Their study provides examples of the formation of ISAM nanostructures on a substrate with micro 3D features.

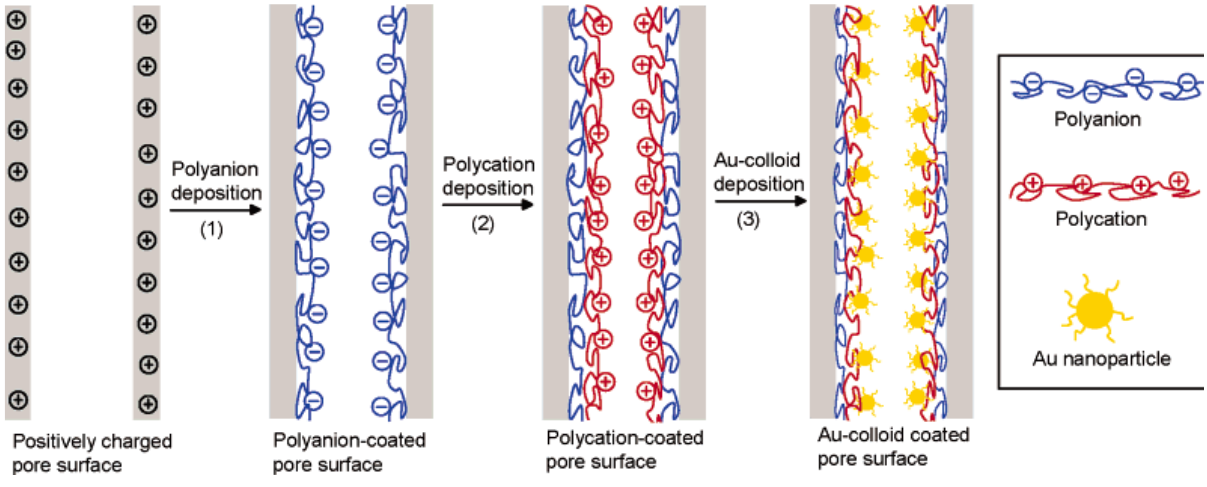

Figure 2.3. Formation of ISAM PAA-PAH/GNP layers in the pore structure of an alumina membrane.[60] Steps (2) and (3) can be repeated to achieve thicker PAH/GNP coating. (fair use)

Because of their proper refractive index, SNP have often been chosen to be deposited on glass substrates for anti-reflection applications.[61-65] However, another key parameter for anti-reflection is the relationship between the wavelength of the incident light and the coating thickness, thus the LbL self-assembly technique is an ideal approach for fabricating ISAM SNP coating with anti-reflection properties due to the convenience in the fine tuning of the coating and choosing SNP with different sizes. Taking advantage of this technique, Yancey *et al*.[61] deposited ISAM PAH/SNP thin films on a glass surface to act as anti-reflection coatings. The facile control over the coating thickness by depositing different number of BLs helped to satisfy the first condition for anti-reflection coating—optical thickness equal to 1/4 of the wavelength of incident light, while the porous structure of the ISAM SNP provided the correct refractive. This took care of the other restriction over the refractive index. They prepared ISAM coatings made of SNP with 15, 45, and 85 nm diameter on both sides of the glass slides, and maximum transmittances above 97% were achieved for the incident light with a wavelength range 350~700 nm through all of the ISAM SNP coatings. On the other hand, Rosidian *et al*.[66] reported the LbL deposition of ISAM zicronia (ZrO_2) nanoparticles with poly(sodium-4-styrenesulfonate) (PSS) as polyelectrolyte in between the nanoparticle layers to make an ultrahard coating on silicon or glass substrates. After 1 hour calcination at 900 °C, ISAM coatings containing PSS/ZrO_2 NP showed much superior microhardness over the ZrO_2 coating fabricated via sputtering. The high value of microhardness was attributed to the high packing density of the nanosized ZrO_2 particles and clusters, as well as the minimum void gaps between adjacent nanoparticles as a result of the burnout of the polyelectrolyte material that had been between them. The two works mentioned above are good examples, from two sides, to show the unique properties ISAM nanostructures can have by incorporating the properties from the "building block" nanomaterials and unique

physical structures either directly established during the ISAM fabrication or manipulated afterwards.

Besides nanoparticles, along with the recent development of novel carbon based nanostructures, the LbL self-assembly of CNT and graphene have also been investigated due to their unique electrical and mechanical properties. For instance, it was reported by Shen *et al*. [67] that multi-walled carbon nanotubes (MWCNT) can be modified by covalent bonding with poly(acrylamide) (PAM) and poly(acrylic acid) (PAA) to become positively and negatively charged (or cationic and anionic), respectively. With the assistance of two cationic and anionic polyelectrolyte solutions, LbL films of ISAM MWCNT were self-assembled on several substrates. Similarly, ISAM thin film graphene nanopallets were also developed and reported by the same group.[68] In addition, hybrid ISAM nanostructures including CNT/GNP[69] and graphene/Pt NP composites[70] were also successfully fabricated for a variety of applications.

Our group has performed extensive studies on the application of ISAM nano/micro structures with unique electrochromic properties to fabricate solid-state devices. Using active electrochromic polyaniline (PANI) and poly(2-acrylamido-2-methylpropanesulfonic acid) (PAMPs) as polycation and polyanion, respectively, Janik *et al*.[71] deposited ISAM films of PANI/PAMPs on ITO glass to build a quasi-solid state electrochromic device that demonstrated a response time less than 50 ms when responding to a square wave input of 1.0 V. After that, Jain *et al*. explored a variety of other micro-nano scaled polymer materials bearing electrochromic properties (including ruthenium purple,[72] polyviologen (PV),[73] poly(3,4-ethylenedioxythiophene): poly(styrenesulfonate) (PEDOT:PSS),[74] and polysilsequioxane nanoparticles[42]) and fabricated ISAM coatings containing these materials on ITO glasses to make

high contrast solid state electrochromic devices with subsecond switching speed in response to low voltage stimuli. Figure 2.4 is an example of the performance of one such device.

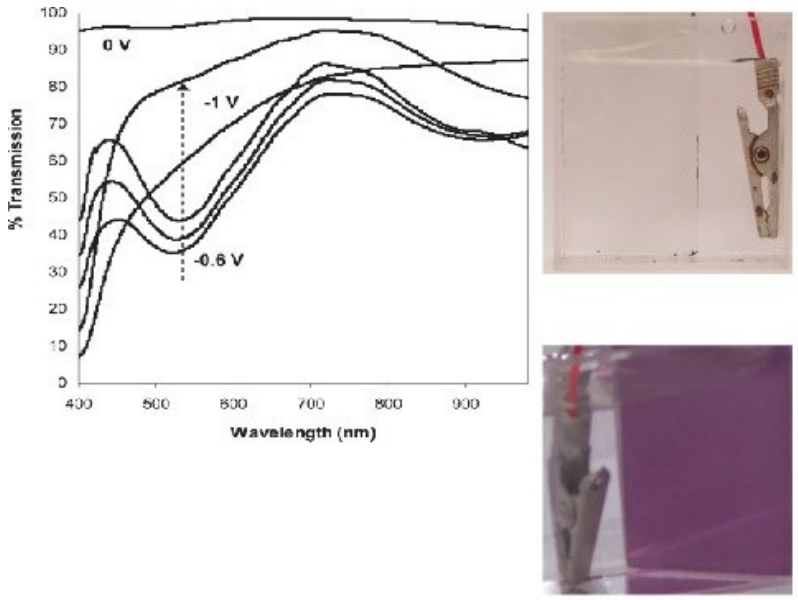

Figure 2.4. Electrochromic response of a device containing 40 BL ISAM PV/PAMPs.[73] The color and transmission switch shown have a speed of ~100 ms in response to 1 V input. (fair use)

Moreover, ISAMs of macromolecules have been extensively investigated due to the versatility in choosing a variety of ionic chromophores as the components in order to achieve desired order. One example is the field of nonlinear optics; chromophores with a rigid side group connected to the polymer main chain tend to align with each other because of the internal ionic bonds.[75] Moreover, by utilizing nonlinear optical polymer chromophores (dyes) as the components, Heflin *et al*.[76] deposited up to 100 BL of ISAM film while maintaining the growth of the desired second order harmonic generation (SHG), which implies order at large scales was obtained in the assembled thin film structure. Other polyelectrolyte materials possessing SHG ability were also investigated by our group in the forms of ISAM films deposited either on flat glass substrates or optical fibers.[77-79]

Besides, our group has also investigated and is still working on the incorporation of ISAM PAH/PCBS thin film coatings on optical fibers to achieve highly sensitive optical responses to the coating refractive index and thickness, which can be used as chemical or biological sensors.[80-82]

In the studies reported in this dissertation, ISAM thin films of GNP and SNP were fabricated on the surfaces of planar *i*EAP membranes and 3D microstructures etched in silicon for μGC devices, respectively. In addition to the large surface area and highly porous structure, which is common to both of these ISAM nanoparticle thin films, the GNP ISAM thin film is also highly conductive, while the SNP one has excellent thermal stability. These combined properties, along with the adaptivity of ISAM to different substrate configurations are ideal for prospective applications and will be discussed in this dissertation.

2.2 Components of ionic polymer-metal composite (IPMC) electromechanical bending actuators

2.2.1 Ionic electroactive polymers (iEAPs) as the backbone

An IPMC actuator usually consists of an *i*EAP membrane as the backbone, an electrolyte matrix and a noble metal or carbon coating as electrodes. The most commonly used *i*EAP membranes are commercially-available Nafion™ [83-85] and Flemion™.[86-88] But, there are several newly synthesized polymers that could also be used, and they will also be discussed in this dissertation later on. Nafion is a perfluorosulfonate membrane (DuPont, USA. Figure 2.5) and Flemion is a perfluorocarboxylate acid membrane (Asahi Glass, Japan. Figure 2.6). Both of them have a polytetrafluoroethylene (commercial name Teflon™) backbone while Nafion is

perfluorosulfonic acid type and Flemion is carboxylic acid type. They both have high ion exchange capacity, chemical and thermal stability, and decent mechanical properties in terms of good balance between strength and flexibility. The working ions within both of these membranes, upon hydration, are the counterions of the end groups, which could either be protons or cations such as Na+, K+, or Li^+.[89,90] Since the bending performance of IPMC actuators closely relates to the ion motion in the *i*EAP membranes, the understanding of and control over the factors that affect their ion conductivity are crucial for the IPMC actuator studies and applications.

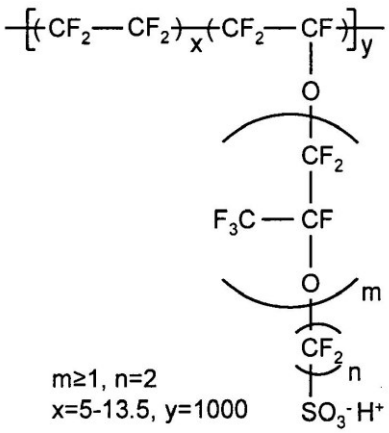

Figure 2.5. Proposed chemical structure of Nafion ion conductive polymer.

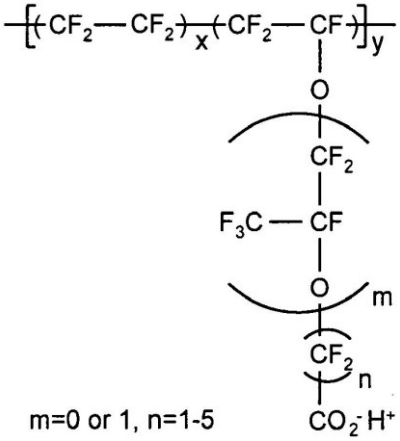

Figure 2.6. Proposed chemical structure of Flemion ion conductive polymer.

Being one of the most famous ionomers, Nafion was initially, and still is, widely used as the permselective ion exchange membrane separator in fuel cell research and applications.[91-94] Its natural cation-only permeability comes from the unique molecular structure in which the perfluorovinyl ether side-chains sprout out from the hydrophobic Teflon (tetrafluoroethylene) backbone and are terminated with negatively-charged hydrophilic sulfonate endgroups (Figure 2.4)

A Nafion membrane in its acid form has protons associated with the negatively-charged sulfonate endgroups, so it is sometimes referred as a solid electrolyte. It can be characterized by equivalent weight (EW) and ion exchange capacity (IEC). EW stands for the weight (in grams) of a dry Nafion membrane when it contains one mole of sulfonic acid groups, while IEC is then defined as IEC=1000/EW.

Although the exact mechanism is still to be determined, several models have been proposed to explain the ion conductivity of the Nafion membrane. According to one of the earliest models proposed by Yeager *et al*.,[95] upon hydration, the phase separation between the highly hydrophobic fluorocarbon portion and the highly hydrophilic sulfonate groups at the ends of the side chains results in the formation of a three-region structure, in which the fluorocarbon chain and the ionic clusters regions are separated with a interfacial zone in between (Figure 2.7). This provides “routes” for counterions to move.

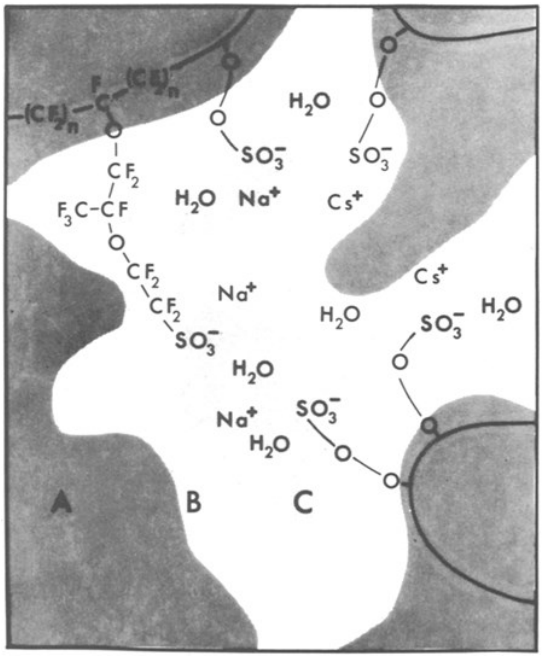

Figure 2.7. Proposed three-region structure of Nafion upon hydration: fluorocarbon backbone (A), interfacial zone (B), and ionic region that contains clusters of sulfonate endgroups and exchanged ions (C).[95] (fair use)

More recently, by applying a new algorithm to simulate the small-angle scattering data obtained from hydrated Nafion, Schmidt-Rohr *et al*.[96] came up with a parallel water channels model in which the hydrophilic sidechains of Nafion form packed cylinders containing water inside to provide "pipes" for ion migration (Figure 2.8). This is so far the most accepted model on the formation of ion conductive channels of Nafion.

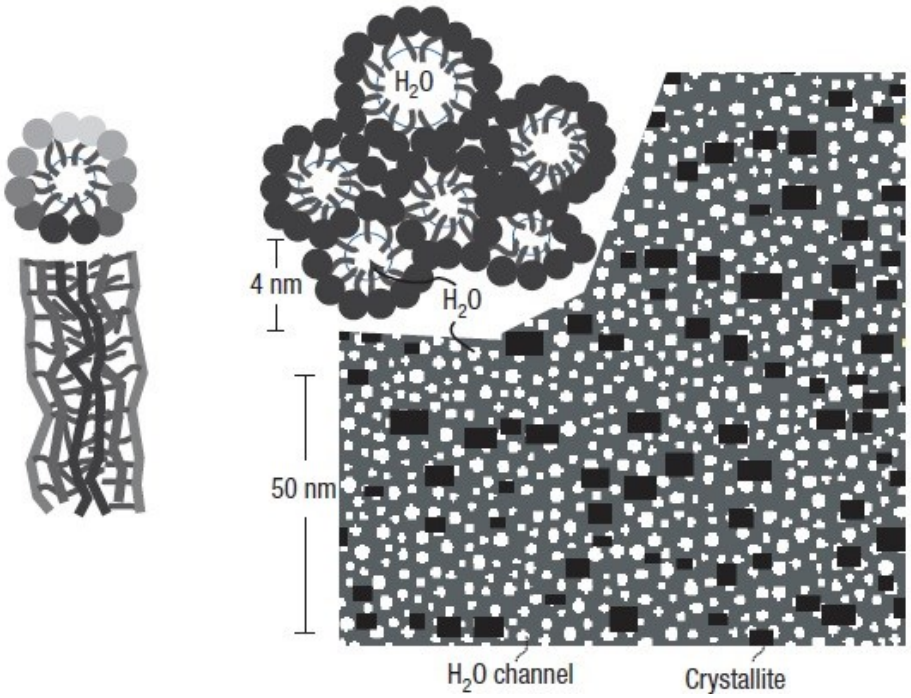

Figure 2.8. Packed cylindrical water channel for ion transport in hydrated Nafion membrane.[96] (fair use)

Regardless of the differences, the importance of water content inside the Nafion membrane was demonstrated in both models presented above. Water not only helps to solvate the counterions associated to the sulfonate group, to make them free to move and thus endue Nafion membrane with electrolytic properties, but also opens channels in the membrane for the transport and migration of even larger ions. The conductivity of a Nafion membrane thus closely relates to the hydration level in the membrane,[97-101] and the mechanical and electrical responses of IPMC actuators made from Nafion highly depend on the water content in the system as well. Detailed results and discussion on this issue are presented in the following chapter.

Having structure similar to Nafion but with carboxylate ($-COO^-$) ionic endgroups instead of sulfonate (see Figure 2.7), a Flemion membrane possesses properties similar to Nafion that make it also suitable to be the *i*EAP membrane backbone for IPMC actuator fabrication. Most of the

researches on Flemion-based actuators were performed by Oguro's group.[87,102-106] In these studies, Flemion actuators were achieved with different electrodes and couterions. The effect of water content on the conductivity and bending performance was demonstrated, and the bending mechanism of such actuators was also discussed. Good bending performance of the Flemion actuator was demonstrated. By incorporating IL as electrolyte (which will be discussed in next section) into the Flemion membrane, Wang *et al*.[107] fabricated IPMC actuators with plated gold electrodes. Flemion-based IPMC actuators with large deformation and good stability were obtained.

2.2.2 Ionic liquids (ILs) as novel electrolytes

IPMC actuators using an *i*EAP backbone can be fabricated simply by applying an outer electrode on both sides of a hydrated polymer membrane. The directional free counterion (proton or exchanged cation) transport through the opened ion conductive channels results in an imbalanced ion accumulation on the two sides of the membrane, and thus generates the mechanical bending. In these cases, *i*EAP membranes act as a solid electrolyte which needs a solvent to dissolve the counterions to make them free to move. The most commonly used solvent—water—has drawbacks in terms of fast evaporation loss and electrolysis threshold,[108,109] which puts limitations on the lifetime and operating voltage of an IPMC actuator. On the one hand, the evaporation loss of water greatly lowers the actuator's lifetime of both operation and storage, so the first generation IPMC actuators were either operated directly in water,[110] or had protective coatings to seal the water inside to prevent it from escaping.[108] Nevertheless, these measures either put strict constraints on the range of applications or introduced passive stiffness

to the actuator. On the other hand, the electrolysis threshold puts a cap on the applied voltage at approximately 1.2 V, which obviously sets limitations on the actuation performance.

Several efforts were made to overcome this limitation posed by water. For example, Nemat-Nasser *et al*.[111,85] reported the use of ethylene glycol and glycerol instead of water to eliminate the loss of electrolyte. And Shahinpoor *et al*.[112] also explored the actuation combination of poly(ethylene oxide) and poly(ethylene glycol). IPMC actuators prepared this way could bear higher applied voltage without electrolysis, at the cost of higher viscosity as compared to water; however, they suffers from slow response, which is another major drawback that needs to be addressed.

Ionic liquids (ILs) are defined as the salts that have a melting point below 100 ℃. Practically, the room temperature ILs (in liquid form at room temperature) are distinct from the rest of the category due to the difference in storage and handling, and most importantly, in the promising potential applications. Therefore, most of the researches were focused on them and they will be exclusively discussed and used in the studies reported in this dissertation. As a type of electrolyte that is in liquid form itself, IL consists of nearly 100% of ions and their combinations, without the demands of solvent for dissociating the ions of a solid electrolyte in the liquid environment. Therefore, since their discovery in the early 20th century, they have been a very interesting object of studies for their potential applications in electrochemical processes and corresponding devices.[113-115]

However, the early generation of aluminium halide-containing ILs are sensitive to moisture and therefore are not suitable for ambient environment storage and application. In 1992, a new group of ILs based on 1-ethyl-3-methylimidazolium cations ([$EMIm^+$]) associated with different anions were synthesized and reported as the first moisture-resistant ILs.[116,117] Since then,

environmentally-stable ILs have been widely used and investigated in almost all of the electrolyte related applications, including electric double layer capacitors,[118-120] fuel cells,[121-123] and solar cells.[124-126]

ILs, especially the ones with [$EMIm^+$] cation, are also an ideal option for the electrolyte used in IPMC actuators due to their good thermal stability and negligible vapor pressure (up to 300~400 ℃),[127] low viscosity (~40 cP), high conductivity (~10 mS/cm) and electrochemical window (>4 V).[128] Since the beginning of the 21st century, several ILs have been incorporated in IPMC actuators. For instance, Lu *et al*.[129] reported the incorporation of 1-butyl-3-methyl imidazolium tetrafluoroborate (BMIm-BF_4) and 1-butyl-3-methyl imidazolium hexafluorophosphate (BMIm-Pf_6) ILs into polyaniline and polypyrrole polymers to construct actuators with a long period of stable actuation performance. Similarly, Ding *et al*.[130] demonstrated improved cycle life span and strain generated by a polypyrrole actuator containing 1-ethyl-3-methyl imidazolium bis-(triflouromethanesulfonyl)amide (EMIm-TFSA) IL, as compared to the traditional organic electrolytes. Moreover, as an alternative actuator fabrication approach, a series of studies of a dry actuator fabricated by casting gelatinous ionic-liquid containing single-walled carbon nanotubes (so called "bucky gel") also showed large stress and strain.[131] Using the most popular *i*EAP membrane Nafion as the backbone, Bennett *et al*.[132] soaked 1-ethyl-3-methylimidazolium trifluoromethanesulfonate (EMIm-Tf) IL in it to make an IPMC actuator with improved stability when operated in air. And the high electrochemical window (4.1 V) of EMIm-Tf IL allow the IPMC actuators using it as electrolyte to be operated under higher voltage and thus generate larger strain with faster response speed.[85] Thus, in most of the work reported in this dissertation, EMIm-Tf IL was used as the working electrolyte for IPMC actuators made of Nafion membrane. EMIm-Tf IL can be easily soaked into the Nafion

membrane without detriment of the mechanical integrity, which shows good compatibility between them.

2.2.3 Conductive network composite (CNC) as porous electrode

The outer electrode layers of IPMC actuators are used to generate an evenly distributed external electric field through the thickness direction of the actuator. However, they do not contribute to the strain generation and instead just add passive stiffness to the actuator. For this reason, it is preferable for them to be highly conductive and in the meantime to have low modulus and be as thin as possible. The electrode can be fabricated through direct assembly (such as electro or electroless plating,[133-135] painting[136]) and impregnation-reduction processes.[137,138] These methods are usually straightforward and have flexibility in material selection. However, they suffer from complicated and high-cost fabrication procedures, as well as difficulties in controlling the morphology and thickness of the coating layers. Moreover, cracking and delamination of the electrode from the polymer surface were also observed after prolonged repeated operations.[139]

Among a couple of approaches for increasing the surface area in the electrode interface, the earliest one is the impregnation-reduction process which was initially developed for the water electrolysis application.[140] The basic idea is as follows: First, precipitate metallic salt onto the polymer membrane in an aqueous solution. The ion exchange between the protons in the ionic polymer membrane and the metal cations makes the latter diffuse into the membrane and is thus called impregnation. Then, the metal ions are reduced by a reducing agent to yield a layer of metal particles penetrated into the polymer membrane. Although this approach has been applied

in many IPMC actuator related studies,[86,141-144] it requires several wet chemistry process steps and is not able to produce uniformly distributed metal particle layers with easy thickness and size control. More importantly, the penetration depth of the metal particles is typically ~10 μm, which is too deep for the *i*EAP thin films used in current studies (25~75 μm). If the accumulation of ions is too close to the center of the membrane, it is inefficient for generating the bending actuation. As a result, this approach is most suitable for thicker *i*EAP membranes. However, a thicker membrane yields larger stiffness, which is detrimental to the speed of mechanical bending actuation. For example, Naji *et al*.[144] used this approach to develop Platinum (Pt) electrode layers with different thickness on Nafion membrane (~200 μm thick) to fabricate IPMC actuators (8 mm × 38 mm) with exchanged Li^+ as working ions. Their actuators generated a maximum ~4.5 mN force (~14.8 Pa stress) and a response time ~3 s under a 4 V input.

In recent years, a couple of new approaches have been developed to fabricate the CNC for IPMC actuators in order to provide better control over the thickness and quality of the CNC while making the fabrication process simpler and with lower cost. Basically, nanostructured conductive materials (metal nanoparticles or nanopowders) were mixed with the ionomer solution, followed by applying it onto the surface of the ionomer membrane by either casting,[145] or direct painting.[136] Better coating quality was obtained by using these techniques, though the drying processes involved are time consuming, and it is challenging to achieve a homogenous CNC coating. Besides, the ionomer membranes often need to be sanded to get a rough surface in order to ensure good contact with the polymer-metal mixture, which adds more complexity to the process.[132]

In comparison to the techniques aforementioned, the LbL self-assembly technique is ideal for fabricating a nanostructured ISAM CNC for IPMC actuators due to its simple concept,

straightforward operation, versatile selection of the material and substrate, superior coating quality and fine thickness control. It has been applied by our group in several recent IPMC actuator studies and promising results have been obtained.[85,146,147] For instance, Liu *et al*.[85] obtained a very fast response (~0.18 s) of an IPMC actuator with Nafion backbone (~25 μm thick) and 100 BL ISAM GNP CNC. Montazami *et al*.[147] reported a maximum curvature of ~0.43 mm^{-1} generated by an IPMC actuator with the same Nafion membrane and 80 BL GNP CNC. Similarly, a CNC consisting of GNP deposited via the LbL technique was used for the actuator studies in the work reported here and the detailed fabrication process will be described in section 3.1.2.

2.3 Microelectromechanical systems (MEMS) gas chromatography (GC) devices

2.3.1 MEMS GC

The invention of GC can be traced back to 1951, when the first prototype of GC system was built and reported (Figure 2.9).[148] While quite antique, it contained the "ancestors" of almost every part that is still used in modern GC systems, including sample inlet ports, a glass vial that was filled with adsorbent to purify the hydrogen carrier gas (similar to the gas pretreatment by preconcentrator though it handled carrier gas instead of analytes here), and a glass separation column with 1 cm O.D. and 2 cm long that was packed with silica gel or activated charcoal as stationary phase, and a thermal conductivity detector (TCD). The separation column and TCD were placed in Dewar flasks, which acted like the GC oven of today. All the components were connected with glass tubing and the gas flow was manually controlled by stopcocks.

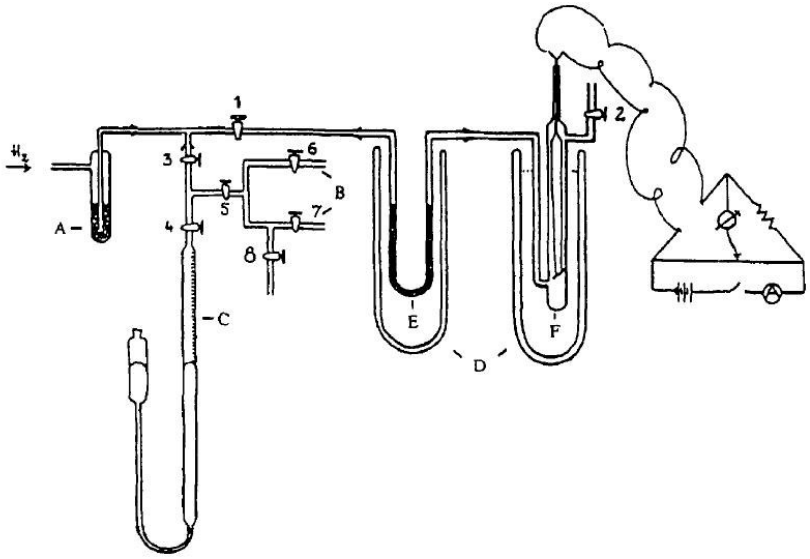

Figure 2.9. First GC system with major parts still being used in modern GC. A) "preconcentrator", B) "sample injector", D) "GC oven" E) separation column, F) thermal conductivity detector.[148] (fair use)

After that, GC studies were primarily driven by the need of oil companies for a reliable new analytical technique, and commercial GC products thus started to emerge. The separation columns that were used in early GC systems were packed with materials as stationary phase and experienced high flow resistance. The emergence of the wall-coated open-tubular (WCOT) capillary columns along with the development of fused-silica capillary tubing significantly reduced the demanding amount of sample injection and thus increased the detection sensitivity. With such improved separation columns, along with more advanced detectors, the conventional GC system has been one of the most commonly used instruments in analytical chemistry applications.

However, the bulky bench-top GC system does not meet the increasing needs for portable and real time onsite analysis. One approach to achieve these goals could rely on MEMS GC devices fabricated by etching 3D microstructures in silicon chips, developing functionalizing

materials in the microfeatures, and finally sealing the functionalized features to make microfluidic cavities or channels. A large amount of research has been done to explore this approach, including the work performed by one of the major collaborators of our group—the VT MEMS lab at the Bradley Department of Electrical and Computer Engineering at Virginia Tech led by Prof. Masoud Agah. Two key components for the MEMS GC system— μTPC and μSC are discussed in the next two sections. While the geometric design of the microfeatures does contribute to the efficient interaction between the gas flow and the inner surface, the functional material coated on the inner surfaces is the key factor that determines the quality and performance of the μGC devices.

2.3.2 Microthermal preconcentrator (μTPC)

Conceptually, two major preconcentration mechanisms can be used to collect and trap gas molecules: cryogenic and regular temperature sorptions. For the cryogenic approach, gas samples are conducted through tubing chilled with cryogenic fluids, to condense and thus be trapped in it. Then, the analytes are desorbed back into their gas phase by elevating the temperature.[149] However, the demanding cryogenic setup makes this method not suitable for a μGC system. On the contrary, ambient temperature sorption relies on adsorbent materials with unique surface properties. At the early stage of their development, preconcentrators were made of a tube filled with adsorbent materials, which should be porous, inert, and mechanically and thermally stable.[150] The analytes were trapped on the surface of the adsorbent when the gas traveled through the tube, and then thermally desorbed into the carrier gas during a controlled heating process. Simple as this seems, the cost of this type of preconcentrator is around $100 per piece, and it also requires a much more expensive desorption apparatus. Moreover, the

desorption is usually slow and incomplete due to the inefficient heat transfer in the bulky adsorbent materials, and it results in low peak resolution in the separation column. Thus, a micro-fabricated GC preconcentrator with a thin film adsorbent coating is desirable in both efficiency and cost considerations.

Three different categories of μTPC have been reported in the literature. They are distinguished from each other based on the cavity layout (empty, or encompassing either channels or micro-posts) and by the adsorbent profile (granular or thin film). In the devices using granular adsorbent material, channels and cavities formed in silicon are filled with adsorbent beads and then sealed (bonded) to another substrate.[151-158] The second type of μTPC utilizes adsorbent materials in thin film form deposited on a membrane or inside microfabricated channels or cavities.[159-165] There are trade-offs with both types of devices. The first type can provide high sample capacity but suffers from high pressure drops and power consumption during the thermal desorption process. In addition, the difficulty in restricting the beads inside the cavity makes the bonding process extremely cumbersome and can lower the fabrication yield. The devices in the second category significantly reduce the pressure drop, though they have limited sample capacity due to less surface area interacting with the analytes. A third type of μTPC addresses the limitations of the previous types by embedding closely-spaced HAR micro-posts inside an etched cavity and by coating them with a thin film adsorbent layer. This type of μTPC has been extensively explored and established in several works for both enhancing the adsorption capacity and improving the flow distribution in the microchip devices,[166-169] and is also the focus of this dissertation.

There are a variety of commercially-available adsorbents for μTPC depending on the chemical properties of the volatile organic compounds (VOCs) to be concentrated. They can be

generally divided into three categories: carbon based (charcoal, carbon black and carbon sieve), inorganic (glass beads, silica gel), and organic polymers (Chromosorb, Porapak and Tenax TA). Within all the organic polymer adsorbents, there is a significant amount of literature available on the adsorption properties of Tenax TA [poly(2,6-diphenylene oxide)] in the granular form,[170-178] with a few describing the VOCs adsorption mechanisms.[179-181] VT MEMS LAB has published a systematic fundamental study of this polymer in thin film form with regard to surface topography, crystal structure, thermal stability, modes of adsorption, and adsorption/desorption characteristics.[182-184] For instance, Alfeeli *et al*.[185] designed and fabricated a HAR μTPC by silicon etching with embedded criss-cross pillars, which were subsequently coated with thin film Tenax TA adsorbent using an inkjet method. Good coating quality was obtained and the concentration ability of μTPC functionalized this way was enhanced nearly 50 times. Figure 2.10 shows SEM images of Tenax TA thin film coated micropillars in the μTPC, while the good and consistent adsorbing behavior is shown in Figure 2.11.

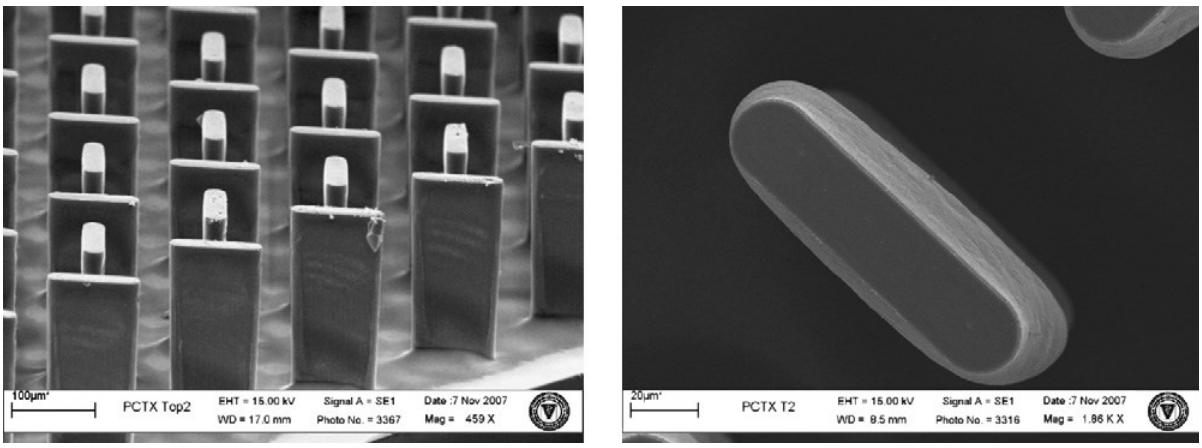

Figure 2.10. Left: Criss-cross design of the micropillars with thin film Tenax TA coating as adsorbent in the cavity of microfabricated HAR μTPC; Right: closer look at a single pillar.[185] (fair use)

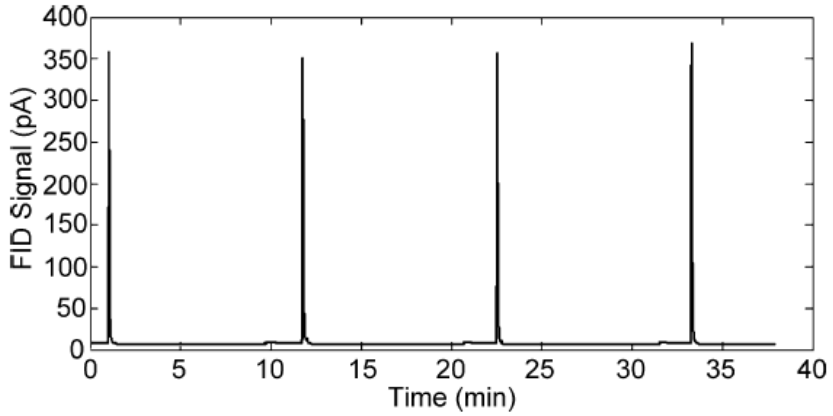

Figure 2.11. Good adsorption with decent consistency in four consecutive runs, as demonstrated by almost identical desorption peaks from multiple injections.[185] (fair use)

The thin film form of the polymeric adsorbent is pretty smooth, which is not beneficial to the μTPC application where larger surface area for gas—material interaction is always favored. Therefore, by adjusting the coating conditions, such as temperature, pressure, etc., they also investigated a variety of Tenax TA films formed in μTPC devices. It was found that the morphology of this polymer adsorbent film is very sensitive to those environmental factors. Very distinctive thin film profiles were formed under different coating conditions, showing the lack of easy control over the coating morphology (Figure 2.12).[183]

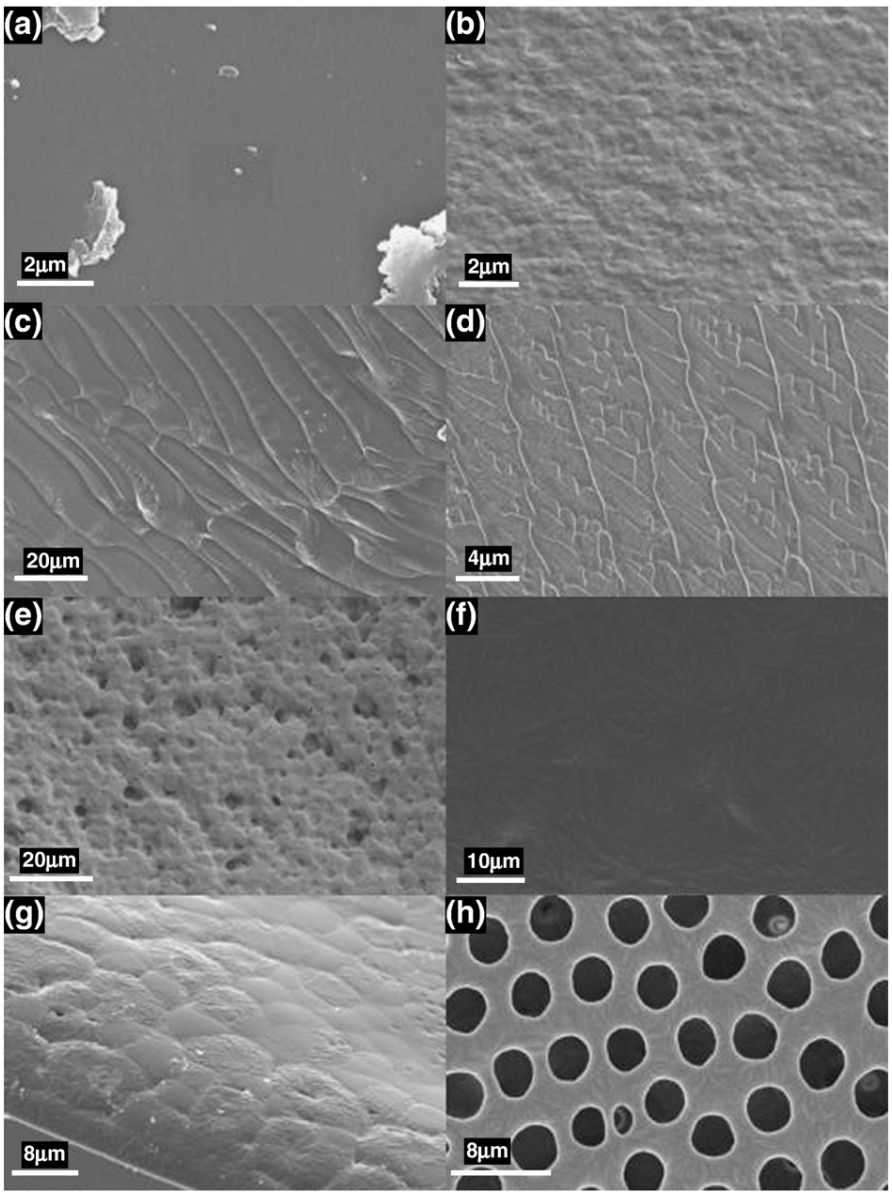

Figure 2.12. Very distinctive morphologies of Tenax TA thin films in μTPCs when the fabrication conditions were different.[183] (fair use)

Due to their well-defined structure and high surface area, nanostructured materials are a promising type of adsorbent for μTPC. CNT,[186,187] carbon nanopowder,[188] and ISAM GNP[182] have been applied as adsorbent materials, just to name a few. The biggest challenge lies in the incorporation of a uniformly distributed conformal coating in the microscale 3D structure. This is one of the main topics to be discussed in detail in this dissertation.

2.3.3 MEMS GC separation column (μSC)

The miniaturization of GC separation columns, in most of cases, was achieved by fabricating very narrow (microscale) HAR channels spiraling in silicon chips. By doing so, meters-long columns can be packed into a device with on the scale of centimeter (see Figure 1.4). The performance of these μSC can be quantitatively evaluated by the commonly used figure of merit: height equivalent to a theoretical plate (HETP), $HETP=L/N$, where L is the length of the column and N is the number of plates in the column, as determined experimentally from peak retention times (t_r) and widths at half the peak height ($w_{1/2}$): $N = \left(\frac{t_r}{w_{1/2}}\right)^2$. HETP also depends on the flow rate of the carrier gas, and the one corresponding to the minimum HETP is called the optimum flow rate. Thus, it is preferable to have an enhanced interaction between the mobile and stationary phase to increase the retention times of individual constituents traveling through the column and thus separate them based on the differences of their retention times. Moreover, the existence of narrow and symmetric signal peaks representing each component identified by the detector also contributes to a lower HETP.

Longer retention time requires enhanced interaction between the mobile and stationary phase, and for the two major categories of the GC column (packed and open tubular) different approaches are applied to increase the surface area of the stationary phase. The packed columns are filled with material, usually in the form of thin film-coated small supporting particulates, as a stationary phase to enhance the interaction with the mobile phase.[189] This has a relatively large surface area and thus greater sample capacity, so overloading the column is not likely to happen. The choice of the adsorbing materials to be packed in the column is also abundant. However, such configuration suffers from a large pressure drop and sinuous flow along the column, which

is detrimental to the column efficiency.[190] Nevertheless, they had dominated GC applications until fused-silica open tubular columns were introduced. Along with the development of the fused-silica drawing process, the open tubular design began to take over as the predominant separation column in GC applications since the early 1980s. It uses a homogeneous thin layer coating on the inner surface as the stationary phase, so it is also often referred to the wall-coated open tubular (WCOT) capillary column. The WCOT capillary column significantly reduces the pressure drop and increases the separation speed and column efficiency. More importantly, this configuration makes it easier to standardize commercial production and thus prompted the spread of the application of capillary GC to the analytical research community.[191,192]

To achieve reasonable resolving power, the WCOT capillary column needs to have enough length for the analytes in the mobile phase to sufficiently interact with the stationary phase. The typical length of the capillary column can range from 10 to more than 100 meters, depending on the specific requirements of the analysis. It is too cumbersome, by all means, for the integrated MEMS μGC systems endeavor. As a pioneering attempt in miniaturizing the GC column, Terry *et al*.[193] reported the application of semiconductor integrated circuit fabrication techniques, including etching and photolithographic procedures, to create a long spiral groove in the surface of a silicon wafer followed by sealing the top with a Pyrex glass cover. The channel fabricated using this method was a 200 μm in width by 30 μm in height rectangular cross section and was 1.5 m in length. Substantially more compact compared to the conventional capillary columns though, this configuration still was the size of a whole silicon wafer, and its separation performance was relatively poor too due to the inhomogeneity of the liquid stationary phase introduced on the internal column wall. Since then, much work has been done in pursuing miniaturized GC columns by etching channels in silicon, metal and polymer substrates.

According to a theoretical study of the HETP of rectangular channels, a narrower column results in lower HETP and thus better separation efficiency.[194] As a result, a series of HAR μSC designs including simple rectangular single capillary (μSCC, Figure 4.10),[195] multi-capillary (μMCC, Figure 4.11),[195] semi-packed (μSPC, Figure 4.25), and width-modulated (μWMC, Figure 3.20)[196] configurations have been proposed and investigated.

A multi-capillary column has a set of very narrow (≤ 30 μm) HAR columns as a group serpentining in parallel in the etched silicon chip. The gas is split at the inlet into the individual columns and merge together before the outlet. Such a configuration achieves high separation efficiency as a result of a much narrower individual column; and in the meantime reduces the adverse effect in terms of the sample capacity when using a single very narrow column. A semi-packed column contains an array of embedded micro-pillars along the trench direction. It not only has better sample capacity and separation efficiency than an open capillary column, but its pressure drop and eddy diffusion is also largely improved, as compared to a conventional packed column. Thanks to the versatile designing ability of semiconductor microfabrication, these novel μGC separation columns open a door to more optimized designs of the 3D microstructure of the column. However, column functionalization also becomes more challenging due to the difficulties in effectively and reliably fabricating conformal coatings on the internal wall of the μGC columns with such delicate and complicated microstructures.

The stationary phase coating inside the μSC is another key factor that determines the separation performance. Desired stationary phase materials should have high porosity and large surface area for effective interaction with the mobile phase, chemical inertness to prevent chemical reactions, as well as mechanical and thermal stability that is crucial for GC operation where high pressure gas flow and rapid temperature programming are usually involved. It should

also be selected based on the surface properties and the polarity of the analyte molecules. And most importantly, the stationary phase should be easy to be incorporate into the 3D microstructures to form a uniform coating.

Because of the need to meet almost the same requirements, the most widely used stationary phase materials for GC μSC are somewhat similar to the ones used for adsorbents in μTPC, including carbon, inorganic porous materials (silica, alumina, etc.), molecular sieves, and polymers (DVB, OV1, Carbowax, etc.) For example, by incorporating OV1 and Carbowax polymeric stationary phases, a microclumn with spiral configuration showed adequate separation of six gas phase chemical compounds.[197] Besides, in pioneering work silica coatings fabricated by sputtering,[198] and alumina thin films deposited by atomic layer deposition (ALD)[199] as stationary phases for GC separation were also reported, the HETP values thus obtained were 0.04 cm and 0.025 cm, respectively.

The effect of the different column lengths was also demonstrated; significantly longer retention times were obtained for longer columns. In VT MEMS LAB, many recent efforts have been put on investigating the incorporation of SAM thiol covered thin gold films as stationary phase. For example, Shakeel *et al*. reported several studies of such stationary phases, and achieved the highest multi-compound separation efficiency (HETP=0.003 cm) so far reported for μMCCs.[200-202] Moreover, SAM thiol on GNP can be easily removed and another thiol can be applied afterwards, which provides a reconfiguration ability over the stationary phase to modify its separation properties.[203]

Similar to the adsorbent material for μTPC, nanostructures are ideal candidates for porous and versatile stationary phase coating in the channels or any microstructures in them and thus have been extensively investigated.[204] Vertically aligned SWCNTs were grown in the silicon

based μSC channels and were reported to have the ability to separate 15 components.[205] ISAM GNP coatings were fabricated in μSCs as well due to their versatility in incorporating different SAM thiol layers as stationary phase to achieve selective separation.[206] Among all the nanomaterials, SNP are one of the most attractive components used in nanostructured stationary phases due to their good chemical and thermal stability,[195,196,207,208] and are the primary stationary phase material used in the μGC studies reported in this dissertation.

References

1 J. A. Shapiro, *Annual Review of Microbiology* **52,** 81 (1998).

2 N. Shimoyama, K. Sugawara, T. Mizuguchi, Y. Hayakawa, and M. Sano, *Physical Review Letters* **76,** 3870 (1996).

3 E. Bonabeau, M. Dorigo, and G. Theraulaz, *Nature* **406,** 39 (2000).

4 D. Philp and J. F. Stoddart, *Angewandte Chemie (International ed.)* **35,** 1155 (1996).

5 H. Liu and G. D. Bachand, *Soft Matter* **7,** 3087 (2011).

6 K. V. Tretiakov, K. J. M. Bishop, and B. A. Grzybowski, *Soft Matter* **5,** 1279 (2009).

7 G. M. Whitesides and B. Grzybowski, *Science* **295,** 2418 (2002).

8 W. Knoll, *Current Opinion in Colloid & Interface Science* **1,** 137 (1996).

9 J. Tien, A. Terfort, and G. M. Whitesides, *Langmuir* **13,** 5349 (1997).

10 X. Zhang and J. C. Shen, *Advanced Materials* **11,** 1139 (1999).

11 A. M. Kalsin, M. Fialkowski, M. Paszewski, S. K. Smoukov, K. J. M. Bishop, and B. A. Grzybowski, *Science* **312,** 420 (2006).

12 Y. Fang, S. Guo, C. Zhu, Y. Zhai, and E. Wang, *Langmuir* **26,** 11277 (2010).

13 M. Wang, K. M. Liechti, Q. Wang, and J. M. White, *Langmuir* **21,** 1848 (2005).

14 Y. L. Wang and M. Lieberman, *Langmuir* **19,** 1159 (2003).

15 J. Wang, L. M. Frostman, and M. D. Ward, *Journal of Physical Chemistry* **96,** 5224 (1992).

16 M. Zharnikov and M. Grunze, *Journal of Physics-Condensed Matter* **13,** 11333 (2001).

17 J. C. Love, L. A. Estroff, J. K. Kriebel, R. G. Nuzzo, and G. M. Whitesides, *Chemical Reviews* **105,** 1103 (2005).

18 G. K. Toworfe, R. J. Composto, I. M. Shapiro, and P. Ducheyne, *Biomaterials* **27,** 631 (2006).

19 M. D. Hanwell, S. Y. Heriot, T. H. Richardson, N. Cowlam, and I. M. Ross, *Colloids and Surfaces a-Physicochemical and Engineering Aspects* **284,** 379 (2006).

20 G. Decher and J. D. Hong, *Makromolekulare Chemie-Macromolecular Symposia* **46,** 321 (1991).

21 G. Decher, J. D. Hong, and J. Schmitt, *Thin Solid Films* **210,** 831 (1992).

22 T. Zeng, R. Claus, F. Zhang, W. Du, and K. L. Cooper, *Smart Materials & Structures* **10,** 780 (2001).

23 R. Montazami, S. Liu, Y. Liu, D. Wang, Q. Zhang, and J. R. Heflin, *Journal of Applied Physics* **109,** 104301 (2011).

24 T. Fukushima, K. Asaka, A. Kosaka, and T. Aida, *Angewandte Chemie-International Edition* **44,** 2410 (2005).

25 S. Liu, R. Montazami, Y. Liu, V. Jain, M. Lin, X. Zhou, J. R. Heflin, and Q. M. Zhang, *Sensors and Actuators A: Physical* **157,** 267 (2010).

26 N. Raoufi, F. Surre, T. Sun, M. Rajarajan, and K. T. V. Grattan, *Sensors and Actuators B: Chemical* **169,** 374 (2012).

27 J. H. Kim, S. H. Kim, and S. Shiratori, *Sensors and Actuators B: Chemical* **102,** 241 (2004).

28 B. Z. Wang, X. Y. Du, M. Q. Wang, W. L. Gong, and J. Anzai, *Electroanalysis* **20,** 1028 (2008).

29 G. A. Evtugyn and T. Hianik, *Current Analytical Chemistry* **7,** 8 (2011).

30 P. Sun, Y. D. Jiang, G. Z. Xie, X. S. Du, X. Li, and J. Hu, *Science China-Information Sciences* **54,** 2680 (2011).

31 L. L. Cui, T. Pu, Y. Liu, and X. Q. He, *Electrochimica Acta* **88,** 559 (2013).

32 I. Del Villar, I. R. Matias, F. J. Arregui, and P. Lalanne, *Optics Express* **13,** 56 (2005).

33 Z. Wang, J. R. Heflin, K. Van Cott, R. H. Stolen, S. Ramachandran, and S. Ghalmi, *Sensors and Actuators B: Chemical* **139,** 618 (2009).

34 A. Marletta, F. A. Castro, C. A. M. Borges, O. N. Oliveira, R. M. Faria, and F. E. G. Guimaraes, *Macromolecules* **35,** 9105 (2002).

35 H. H. Yu, D. S. Jiang, X. F. Li, D. S. Yu, and L. D. Zhou, in *Advanced Materials and Devices for Sensing and Imaging II*; *Vol. 5633*, edited by A. Wang, Y. Zhang, and Y. Ishii (2005), p. 470.

36 S. Wang, L. Zhao, X. Zhang, Z. Shi, Z. Cui, and Y. Yang, *Journal of Colloid and Interface Science* **336,** 470 (2009).

37 Z. A. Khan, R. Kumar, W. S. Mohammed, G. L. Hornyak, and J. Dutta, *Journal of Materials Science* **46,** 6877 (2011).

38 J. R. Heflin, M. T. Guzy, P. J. Neyman, K. J. Gaskins, C. Brands, Z. Wang, H. W. Gibson, R. M. Davis, and K. E. Van Cott, *Langmuir* **22,** 5723 (2006).

39 R. Montazami, V. Jain, and J. R. Heflin, *Electrochimica Acta* **56,** 990 (2010).

40 V. Jain, R. Sahoo, S. P. Mishra, J. Sinha, R. Montazami, H. M. Yochum, J. R. Heflin, and A. Kumar, *Macromolecules* **42,** 135 (2008).

41 K. Shinbo, K. Kato, F. Kaneko, K. Onishi, R. C. Advincula, and X. W. Fan, *Molecular Crystals and Liquid Crystals* **407,** 493 (2003).

42 V. Jain, M. Khiterer, R. Montazami, H. M. Yochum, K. J. Shea, and J. R. Heflin, *Acs Applied Materials & Interfaces* **1,** 83 (2009).

43 D. J. Schmidt, E. M. Pridgen, P. T. Hammond, and J. C. Love, *Journal of Chemical Education* **87,** 208 (2010).

44 C. H. B. Silva, N. A. Galiote, F. Huguenin, E. Teixeira-Neto, V. R. L. Constantino, and M. L. A. Temperini, *Journal of Materials Chemistry* **22,** 14052 (2012).

45 D. M. DeLongchamp and P. T. Hammond, *Chemistry of Materials* **16,** 4799 (2004).

46 D. Yoo, S. S. Shiratori, and M. F. Rubner, *Macromolecules* **31,** 4309 (1998).

47 S. S. Shiratori and M. F. Rubner, *Macromolecules* **33,** 4213 (2000).

48 A. Garg, J. R. Heflin, H. W. Gibson, and R. M. Davis, *Langmuir* **24,** 10887 (2008).

49 Y. Wang, A. S. Angelatos, and F. Caruso, *Chemistry of Materials* **20,** 848 (2008).

50 D. G. Shchukin, A. A. Patel, G. B. Sukhorukov, and Y. M. Lvov, *Journal of the American Chemical Society* **126,** 3374 (2004).

51 Q. Ji, M. Miyahara, J. P. Hill, S. Acharya, A. Vinu, S. B. Yoon, J.-S. Yu, K. Sakamoto, and K. Ariga, *Journal of the American Chemical Society* **130,** 2376 (2008).

52 A. D. Taylor, M. Michel, R. C. Sekol, J. M. Kizuka, N. A. Kotov, and L. T. Thompson, *Advanced Functional Materials* **18,** 3003 (2008).

53 X. Li, F. Gittleson, M. Carmo, R. C. Sekol, and A. D. Taylor, *ACS Nano* **6,** 1347 (2012).

54 B.-S. Kong, J. Geng, and H.-T. Jung, *Chemical Communications* **0,** 2174 (2009).

55 F. Wang, S. Peters, J. Guzda, R. H. Blunk, and A. P. Angelopoulos, *Langmuir* **25,** 4384 (2009).

56 Y. Lvov, K. Ariga, M. Onda, I. Ichinose, and T. Kunitake, *Langmuir* **13,** 6195 (1997).

57 J. Y. Kim, J. P. DeRocher, P. Mao, J. Han, R. E. Cohen, and M. F. Rubner, *Chemistry of Materials* **22,** 6409 (2010).

58 J. P. DeRocher, P. Mao, J. Han, M. F. Rubner, and R. E. Cohen, *Macromolecules* **43,** 2430 (2010).

59 N. A. Kotov, I. Dekany, and J. H. Fendler, *Journal of Physical Chemistry* **99,** 13065 (1995).

60 D. M. Dotzauer, J. Dai, L. Sun, and M. L. Bruening, *Nano Letters* **6,** 2268 (2006).

61 S. E. Yancey, W. Zhong, J. R. Heflin, and A. L. Ritter, *Journal of Applied Physics* **99,** 034313 (2006).

62 J. Moghal, S. Reid, L. Hagerty, M. Gardener, and G. Wakefield, *Thin Solid Films* **534,** 541 (2013).

63 Z. Z. Wu, J. Walish, A. Nolte, L. Zhai, R. E. Cohen, and M. F. Rubner, *Advanced Materials* **18,** 2699 (2006).

64 L. G. Xu and J. H. He, *Acs Applied Materials & Interfaces* **4,** 3293 (2012).

65 L. B. Zhang, Y. Li, J. Q. Sun, and J. C. Shen, *Journal of Colloid and Interface Science* **319,** 302 (2008).

66 A. Rosidian, Y. J. Liu, and R. O. Claus, *Advanced Materials* **10,** 1087 (1998).

67 J. Shen, Y. Hu, C. Qin, and M. Ye, *Langmuir* **24,** 3993 (2008).

68 J. Shen, Y. Hu, C. Li, C. Qin, M. Shi, and M. Ye, *Langmuir* **25,** 6122 (2009).

69 F. Zhang, L. Zhang, J. Xing, Y. Tang, Y. Chen, Y. Zhou, T. Lu, and X. Xia, *Chempluschem* **77,** 914 (2012).

70 C. Zhu, S. Guo, Y. Zhai, and S. Dong, *Langmuir* **26,** 7614 (2010).

71 J. A. Janik, J. R. Heflin, D. Marciu, M. B. Miller, H. Wang, H. W. Gibson, and R. M. Davis, in *Solar and Switching Materials*; *Vol. 4458*, edited by C. M. Lampert, C. G. Granqvist, and K. L. Lewis (2001), p. 146.

72 V. Jain, R. Sahoo, J. R. Jinschek, R. Montazami, H. M. Yochum, F. L. Beyer, A. Kumar, and J. R. Heflin, *Chemical Communications***,** 3663 (2008).

73 V. Jain, H. Yochum, H. Wang, R. Montazami, M. A. Vidales Hurtado, A. Mendoza-Galvan, H. W. Gibson, and J. R. Heflin, *Macromolecular Chemistry and Physics* **209,** 150 (2008).

74 V. Jain, H. M. Yochum, R. Montazami, and J. R. Heflin, *Applied Physics Letters* **92** (2008).

75 S. Balasubramanian, X. G. Wang, H. C. Wang, K. Yang, J. Kumar, S. K. Tripathy, and L. Li, *Chemistry of Materials* **10,** 1554 (1998).

76 J. R. Heflin, C. Figura, D. Marciu, Y. Liu, and R. O. Claus, *Applied Physics Letters* **74,** 495 (1999).

77 K. E. Van Cott, M. Guzy, P. Neyman, C. Brands, I. R. Heflin, H. W. Gibson, and R. A. Davis, *Angewandte Chemie-International Edition* **41,** 3236 (2002).

78 J. R. Heflin, M. T. Guzy, P. J. Neyman, K. J. Gaskins, C. Brands, Z. Y. Wang, H. W. Gibson, R. M. Davis, and K. E. Van Cott, *Langmuir* **22,** 5723 (2006).

79 C. Daengngam, M. Hofmann, Z. Liu, A. Wang, J. R. Heflin, and Y. Xu, *Optics Express* **19,** 10326 (2011).

80 Z. Y. Wang, J. R. Heflin, R. H. Stolen, and S. Ramachandran, *Applied Physics Letters* **86** (2005).

81 Z. Y. Wang, J. R. Heflin, R. H. Stolen, and S. Ramachandran, *Optics Express* **13,** 2808 (2005).

82 Z. Wang, J. R. Heflin, K. Van Cott, R. H. Stolen, S. Ramachandran, and S. Ghalmi, *Sensors and Actuators B-Chemical* **139,** 618 (2009).

83 M. Shahinpoor, Y. Bar-Cohen, J. O. Simpson, and J. Smith, *Smart Materials & Structures* **7,** R15 (1998).

84 B. Kim, B. M. Kim, J. Ryu, I. H. Oh, S. K. Lee, S. E. Cha, and J. Pak, in *Smart Structures and Materials 2003: Electroactive Polymer Actuators and Devices*; *Vol. 5051*, edited by Y. BarCohen (2003), p. 486.

85 S. Liu, R. Montazami, Y. Liu, V. Jain, M. Lin, J. R. Heflin, and Q. M. Zhang, *Applied Physics Letters* **95** (2009).

86 N. Fujiwara, K. Asaka, Y. Nishimura, K. Oguro, and E. Torikai, *Chemistry of Materials* **12,** 1750 (2000).

87 K. Onishi, S. Sewa, K. Asaka, N. Fujiwara, and K. Oguro, *Electrochimica Acta* **46,** 737 (2000).

88 K. Onishi, S. Sewa, K. Asaka, N. Fujiwara, and K. Oguro, *Electrochimica Acta* **46,** 1233 (2001).

89 T. Xue, R. B. Longwell, and K. Osseoasare, *Journal of Membrane Science* **58,** 175 (1991).

90 S. Nemat-Nasser and Y. X. Wu, *Journal of Applied Physics* **93,** 5255 (2003).

91 T. E. Springer, T. A. Zawodzinski, and S. Gottesfeld, *Journal of the Electrochemical Society* **138,** 2334 (1991).

92 K. D. Kreuer, *Journal of Membrane Science* **185,** 29 (2001).

93 C. Y. Wang, *Chemical Reviews* **104,** 4727 (2004).

94 B. Smitha, S. Sridhar, and A. A. Khan, *Journal of Membrane Science* **259,** 10 (2005).

95 H. L. Yeager and A. Steck, *Journal of The Electrochemical Society* **128,** 1880 (1981).

96 K. Schmidt-Rohr and Q. Chen, *Nature Materials* **7,** 75 (2008).

97 A. V. Anantaraman and C. L. Gardner, *Journal of Electroanalytical Chemistry* **414,** 115 (1996).

98 M. Eikerling, A. A. Kornyshev, and U. Stimming, *The Journal of Physical Chemistry B* **101,** 10807 (1997).

99 D. R. Morris and X. D. Sun, *Journal of Applied Polymer Science* **50,** 1445 (1993).

100 T. Okada, G. Xie, O. Gorseth, S. Kjelstrup, N. Nakamura, and T. Arimura, *Electrochimica Acta* **43,** 3741 (1998).

101 F. Opekar and D. Svozil, *Journal of Electroanalytical Chemistry* **385,** 269 (1995).

102 K. Oguro, N. Fujiwara, K. Asaka, K. Onishi, and S. Sewa, in *Smart Structures and Materials 1999: Electroactive Polymer Actuators and Devices*; *Vol. 3669*, edited by Y. BarCohen (1999), p. 64.

103 K. Asaka, K. Oguro, Y. Nishimura, M. Mizuhata, and H. Takenaka, *Polymer Journal* **27,** 436 (1995).

104 K. Asaka and K. Oguro, *Journal of Electroanalytical Chemistry* **480,** 186 (2000).

105 K. Asaka and K. Oguro, *Electrochimica Acta* **45,** 4517 (2000).

106 K. Asaka, N. Fujiwara, K. Oguro, K. Onishi, and S. Sewa, *Journal of Electroanalytical Chemistry* **505,** 24 (2001).

107 J. Wang, C. Xu, M. Taya, and Y. Kuga, *Smart Materials & Structures* **16,** S214 (2007).

108 Y. Bar-Cohen, S. Leary, M. Shahinpoor, J. O. Harrison, and J. Smith, in *Smart Structures and Materials 1999: Electroactive Polymer Actuators and Devices*; *Vol. 3669*, edited by Y. BarCohen (1999), p. 51.

109 Y. Bar-Cohen, S. Leary, A. Yavrouian, K. Oguro, S. Tadokoro, J. Harrison, J. Smith, and J. Su, in *Smart Structures and Materials 2000: Electroactive Polymer Actuators and Devices*; *Vol. 3987*, edited by Y. BarCohen (2000), p. 140.

110 M. Y. F. Kwok, W. L. Zhou, W. J. Li, and Y. S. Xu, in *Experimental Robotics Vii*; *Vol. 271*, edited by D. Rus and S. Singh (2001), p. 471.

111 S. Nemat-Nasser and S. Zamani, in *Smart Structures and Materials 2003: Electroactive Polymer Actuators and Devices*; *Vol. 5051*, edited by Y. BarCohen (2003), p. 233.

112 M. Shahinpoor and K. J. Kim, *Applied Physics Letters* **80,** 3445 (2002).

113 J. S. Wilkes, J. A. Levisky, R. A. Wilson, and C. L. Hussey, *Inorganic Chemistry* **21,** 1263 (1982).

114 A. J. Dent, K. R. Seddon, and T. Welton, *Journal of the Chemical Society-Chemical Communications***,** 315 (1990).

115 T. Tsuda and C. L. Hussey, *Modern Aspects of Electrochemistry, No 45***,** 63 (2009).

116 M. J. Zaworotko and J. S. Wilkes, *Abstracts of Papers of the American Chemical Society* **203,** 201 (1992).

117 J. S. Wilkes and M. J. Zaworotko, *Journal of the Chemical Society-Chemical Communications***,** 965 (1992).

118 C. Nanjundiah, S. F. McDevitt, and V. R. Koch, *Journal of the Electrochemical Society* **144,** 3392 (1997).

119 M. Ue, M. Takeda, A. Toriumi, A. Kominato, R. Hagiwara, and Y. Ito, *Journal of the Electrochemical Society* **150,** A499 (2003).

120 A. Lewandowski and M. Galinski, *Journal of Physics and Chemistry of Solids* **65,** 281 (2004).

121 G. Lakshminarayana and M. Nogami, *Electrochimica Acta* **55,** 1160 (2010).

122 R. Hagiwara, T. Nohira, K. Matsumoto, and Y. Tamba, *Electrochemical and Solid State Letters* **8,** A231 (2005).

123 J. F. Huang, H. M. Luo, C. D. Liang, I. W. Sun, G. A. Baker, and S. Dai, *Journal of the American Chemical Society* **127,** 12784 (2005).

124 H. Matsumoto, T. Matsuda, T. Tsuda, R. Hagiwara, Y. Ito, and Y. Miyazaki, *Chemistry Letters***,** 26 (2001).

125 M. Zistler, C. Schreiner, P. Wachter, P. Wasserscheid, D. Gerhard, and H. J. Gores, *International Journal of Electrochemical Science* **3,** 236 (2008).

126 D. Kuang, S. Ito, B. Wenger, C. Klein, J.-E. Moser, R. Humphry-Baker, S. M. Zakeeruddin, and M. Grätzel, *Journal of the American Chemical Society* **128,** 4146 (2006).

127 M. J. Earle, J. Esperanca, M. A. Gilea, J. N. C. Lopes, L. P. N. Rebelo, J. W. Magee, K. R. Seddon, and J. A. Widegren, *Nature* **439,** 831 (2006).

128 P. Bonhote, A. P. Dias, N. Papageorgiou, K. Kalyanasundaram, and M. Gratzel, *Inorganic Chemistry* **35,** 1168 (1996).

129 W. Lu, A. G. Fadeev, B. Qi, E. Smela, B. R. Mattes, J. Ding, G. M. Spinks, J. Mazurkiewicz, D. Zhou, G. W. Gordon, D. R. MacFarlane, S. A. Forsyth, and M. Forsyth, *Science* **297,** 983 (2002).

130 J. Ding, D. Z. Zhou, G. Spinks, G. Wallace, S. Forsyth, M. Forsyth, and D. R. MacFarlane, *Chemistry of Materials* **15,** 2392 (2003).

131 K. Mukai, K. Asaka, K. Kiyohara, T. Sugino, I. Takeuchi, T. Fukushima, and T. Aida, *Electrochimica Acta* **53,** 5555 (2008).

132 M. D. Bennett and D. J. Leo, *Sensors and Actuators a-Physical* **115,** 79 (2004).

133 P. Millet, F. Andolfatto, and R. Durand, *Journal of Applied Electrochemistry* **25,** 227 (1995).

134 H. Tamagawa, F. Nogata, T. Watanabe, A. Abe, K. Yagasaki, and J. Y. Jin, *Journal of Materials Science* **38,** 1039 (2003).

135 J.-H. Jeon, S.-W. Yeom, and I.-K. Oh, *Composites Part A: Applied Science and Manufacturing* **39,** 588 (2008).

136 B. J. Akle, M. D. Bennett, D. J. Leo, K. B. Wiles, and J. E. McGrath, *Journal of Materials Science* **42,** 7031 (2007).

137 P. Millet, R. Durand, E. Dartyge, G. Tourillon, and A. Fontaine, *Journal of the Electrochemical Society* **140,** 1373 (1993).

138 K. J. Kim and M. Shahinpoor, in *Smart Structures and Materials 2001: Electroactive Polymer Actuators and Devices*; *Vol. 4329*, edited by Y. BarCohen (2001), p. 189.

139 A. Punning, A. Kruusmaa, and A. Aabloo, *Sensors and Actuators a-Physical* **133,** 200 (2007).

140 P. S. Fedkiw and W. H. Her, *Journal of the Electrochemical Society* **136,** 899 (1989).

141 T. Rashid and M. Shahinpoor, in *Smart Structures and Materials 1999: Electroactive Polymer Actuators and Devices*; *Vol. 3669*, edited by Y. BarCohen (1999), p. 289.

142 B. J. Akle, D. J. Leo, M. A. Hickner, and J. E. McGrath, *Journal of Materials Science* **40,** 3715 (2005).

143 M. Shahinpoor and K. J. Kim, *Sensors and Actuators a-Physical* **96,** 125 (2002).

144 L. Naji, J. A. Chudek, E. W. Abel, and R. T. Baker, *Journal of Materials Chemistry B* **1,** 2502 (2013).

145 C. K. Chung, P. K. Fung, Y. Z. Hong, M. S. Ju, C. C. K. Lin, and T. C. Wu, *Sensors and Actuators B-Chemical* **117,** 367 (2006).

146 Y. Liu, S. Liu, J. Lin, D. Wang, V. Jain, R. Montazami, J. R. Heflin, J. Li, L. Madsen, and Q. M. Zhang, *Applied Physics Letters* **96** (2010).

147 R. Montazami, S. Liu, Y. Liu, D. Wang, Q. Zhang, and J. R. Heflin, *Journal of Applied Physics* **109** (2011).

148 O. Bobleter, *Chromatographia* **43,** 444 (1996).

149 B. Kolb, *Journal of Chromatography A* **842,** 163 (1999).

150 K. Dettmer and W. Engewald, *Analytical and Bioanalytical Chemistry* **373,** 490 (2002).

151 H. K. L. Chan, S. W. Pang, R. A. Veeneman, E. T. Zellers, and M. Takei, *The 13th International Conference on Solid-State Sensors, Actuators and Microsystems* **2,** 2091 (2005).

152 I. Gràcia, P. Ivanov, F. Blanco, N. Sabaté, X. Vilanova, X. Correig, L. Fonseca, E. Figueras, J. Santander, and C. Cané, *Sensors and Actuators B: Chemical* **132,** 149 (2008).

153 T. Wei-Cheng, H. K. L. Chan, L. Chia-Jung, S. W. Pang, and E. T. Zellers, *Journal of Microelectromechanical Systems* **14,** 498 (2005).

154 T. Wei-Cheng, S. W. Pang, L. Chia-Jung, and E. T. Zellers, *Journal of Microelectromechanical Systems* **12,** 264 (2003).

155 A. B. Alamin Dow and W. Lang, *Sensors and Actuators B: Chemical* **151,** 304 (2010).

156 E. H. M. Camara, P. Breuil, D. Briand, N. F. de Rooij, and C. Pijolat, *Analytica Chimica Acta* **688,** 175 (2011).

157 A. Rydosz, W. Maziarz, T. Pisarkiewicz, K. Domański, and P. Grabiec, *Microelectronics Reliability* **52,** 2640 (2012).

158 H. Vereb, B. Alfeeli, A. Dietrich, and M. Agah, *IEEE Sensors***,** 1237 (2011).

159 M. Kim and S. Mitra, *Journal of Chromatography A* **996,** 1 (2003).

160 E. W. Simões, S. G. de Souza, M. L. P. da Silva, R. Furlan, and H. E. Maldonado Peres, *Sensors and Actuators B: Chemical* **115,** 232 (2006).

161 I. Voiculescu, R. A. McGill, M. E. Zaghloul, D. Mott, J. Stepnowski, S. Stepnowski, H. Summers, V. Nguyen, S. Ross, K. Walsh, and M. Martin, *IEEE Sensors Journal* **6,** 1094 (2006).

162 C. E. Davis, C. K. Ho, R. C. Hughes, and M. L. Thomas, *Sensors and Actuators B: Chemical* **104,** 207 (2005).

163 G. C. Frye-Mason, R. P. Manginell, E. J. Heller, C. M. Matzke, S. A. Casalnuovo, V. M. Hietala, R. J. Kottenstette, P. R. Lewis, and C. C. Wong, *International Conference on Microprocesses and Nanotechnology. Microprocesses and Nanotechnology '99***,** 60 (1999).

164 M. Martin, M. Crain, K. Walsh, R. A. McGill, E. Houser, J. Stepnowski, S. Stepnowski, H.-D. Wu, and S. Ross, *Sensors and Actuators B: Chemical* **126,** 447 (2007).

165 P. R. Lewis, P. Manginell, D. R. Adkins, R. J. Kottenstette, D. R. Wheeler, S. S. Sokolowski, D. E. Trudell, J. E. Byrnes, M. Okandan, J. M. Bauer, R. G. Manley, and C. Frye-Mason, *IEEE Sensors Journal* **6,** 784 (2006).

166 B. Alfeeli and M. Agah, *IEEE Sensors Journal* **11,** 2756 (2011).

167 B. Alfeeli, D. Cho, M. Ashraf-Khorassani, L. T. Taylor, and M. Agah, *Sensors and Actuators B: Chemical* **133,** 24 (2008).

168 M. Akbar and M. Agah, *2012 IEEE 25th International Conference on Micro Electro Mechanical Systems (MEMS)***,** 906 (2012).

169 M. Akbar, D. Wang, H. Shakeel, J. R. Heflin, and M. Agah, *The 17th International Conference on Solid-State Sensors, Actuators and Microsystems***,** 2759 (2013).

170 E. D. Pellizzari, J. E. Bunch, R. E. Berkley, and J. McRae, *Analytical Letters* **9,** 45 (1976).

171 R. H. Brown and C. J. Purnell, *Journal of Chromatography A* **178,** 79 (1979).

172 S. Seshadri and J. W. Bozzelli, *Chemosphere* **12,** 809 (1983).

173 I. Maier and M. Fieber, *Journal of High Resolution Chromatography* **11,** 566 (1988).

174 K. Ventura, M. Dostál, and J. Churácek, *Journal of Chromatography A* **642,** 379 (1993).

175 V. Simon, M.-L. Riba, A. Waldhart, and L. Torres, *Journal of Chromatography A* **704,** 465 (1995).

176 A. Kroupa, J. Dewulf, H. Van Langenhove, and I. Viden, *Journal of Chromatography A* **1038,** 215 (2004).

177 R. Borusiewicz and J. Zieba-Palus, *Journal of Forensic Sciences* **52,** 70 (2007).

178 M. Schneider and K.-U. Goss, *Analytical Chemistry* **81,** 3017 (2009).

179 K. Sakodynskii, L. Panina, and N. Klinskaya, *Chromatographia* **7,** 339 (1974).

180 D. Zhao and J. J. Pignatello, *Environmental Toxicology and Chemistry* **23,** 1592 (2004).

181 A. Alentiev, E. Drioli, M. Gokzhaev, G. Golemme, O. Ilinich, A. Lapkin, V. Volkov, and Y. Yampolskii, *Journal of Membrane Science* **138,** 99 (1998).

182 B. Alfeeli, V. Jain, R. K. Johnson, F. L. Beyer, J. R. Heflin, and M. Agah, *Microchemical Journal* **98,** 240 (2011).

183 B. Alfeeli, L. T. Taylor, and M. Agah, *Microchemical Journal* **95,** 259 (2010).

184 M. Akbar and M. Agah, *Microelectromechanical Systems, Journal of* **22,** 443 (2013).

185 B. Alfeeli, D. Cho, M. Ashraf-Khorassani, L. T. Taylor, and M. Agah, *Sensors and Actuators B-Chemical* **133,** 24 (2008).

186 C. Saridara, R. Brukh, Z. Iqbal, and S. Mitra, *Analytical Chemistry* **77,** 1183 (2005).

187 F. Zheng, D. L. Baldwin, L. S. Fifield, N. C. Anheier, C. L. Aardahl, and J. W. Grate, *Analytical Chemistry* **78,** 2442 (2006).

188 C. Pijolat, M. Camara, J. Courbat, J. P. Viricelle, D. Briand, and N. F. de Rooij, *Sensors and Actuators B-Chemical* **127,** 179 (2007).

189 M. M. Robson, K. D. Bartle, and P. Myers, *Journal of Microcolumn Separations* **10,** 115 (1998).

190 R. L. B. E. F. Grob, *Modern practice of gas chromatography* (Wiley-Interscience, Hoboken, N.J., 2004).

191 P. F. Bente, E. H. Zerenner, and R. D. Dandeneau, (Hewlett-Packard Co; Yokogawa Hewlett Packard Ltd).

192 S. R. Lipsky, W. J. McMurray, M. Hernandez, J. E. Purcell, and K. A. Billeb, *Journal of Chromatographic Science* **18,** 1 (1980).

193 S. C. Terry, J. H. Jerman, and J. B. Angell, *Ieee Transactions on Electron Devices* **26,** 1880 (1979).

194 M. A. Zarejan-Jahromi, M. Ashraf-Khorassani, L. T. Taylor, and M. Agah, *Journal of Microelectromechanical Systems* **18,** 28 (2009).

195 D. Wang, H. Shakeel, J. Lovette, G. W. Rice, J. R. Heflin, and M. Agah, *Analytical Chemistry* **85,** 8135 (2013).

196 H. Shakeel, W. Dong, J. R. Heflin, and M. Agah, *Sensors Journal, IEEE* **14,** 3352 (2014).

197 P. R. Lewis, R. P. Manginell, D. R. Adkins, R. J. Kottenstette, D. R. Wheeler, S. S. Sokolowski, D. E. Trudell, J. E. Byrnes, M. Okandan, J. M. Bauer, R. G. Manley, and C. Frye-Mason, *Sensors Journal, IEEE* **6,** 784 (2006).

198 J. Vial, D. Thiébaut, F. Marty, P. Guibal, R. Haudebourg, K. Nachef, K. Danaie, and B. Bourlon, *Journal of Chromatography A* **1218,** 3262 (2011).

199 H. Shakeel, G. W. Rice, and M. Agah, *Sensors and Actuators B: Chemical* **203,** 641 (2014).

200 H. Shakeel and M. Agah, in *High-performance multicapillary gas separation columns with MPG stationary phases*, 2011, p. 1909.

201 H. Shakeel and M. Agah, *Microelectromechanical Systems, Journal of* **22,** 62 (2013).

202 H. Shakeel, G. Rice, M. Agah, and Ieee, in *2012 Ieee 25th International Conference on Micro Electro Mechanical Systems* (Ieee, New York, 2012).

203 H. Shakeel, G. Rice, and M. Agah, in *First reconfigurable MEMS separation columns for micro gas chromatography*, 2012, p. 823.

204 E. Guihen and J. D. Glennon, *Analytical Letters* **36,** 3309 (2003).

205 M. Stadermann, A. D. McBrady, B. Dick, V. R. Reid, A. Noy, R. E. Synovec, and O. Bakajin, *Analytical Chemistry* **78,** 5639 (2006).

206 B. Alfeeli, S. Ali, V. Jain, R. Montazami, J. Heflin, and M. Agah, in *MEMS-based gas chromatography columns with nano-structured stationary phases*, 2008, p. 728.

207 H. Shakeel, W. Dong, R. Heflin, and M. Agah, in *Width-modulated microgas chromatography separation columns with silica nanoparticles stationary phase*, 2013, p. 1.

208 N. Na, X. Cui, T. De Beer, T. Liu, T. Tang, M. Sajid, and J. Ouyang, *Journal of Chromatography A* **1218,** 4552 (2011).

CHAPTER 3 SELF-ASSEMBLED NANOSTURCTURES IN IONIC POLYMER-METAL COMPOSITE ACTUATORS

3.1 The fabrication of the Nafion membrane based IPMC actuators

3.1.1 Nafion membrane

The Nafion membrane used as the *i*EAP backbone in the studies reported in this dissertation was extruded Nafion N111-IP membrane (Ion Power Inc.) with 25 μm thickness and EW=1100. It was used as received.

3.1.2 ISAM conductive network composite (CNC) fabricated via LbL self-assembly

To provide greatly enhanced ion storage capacity, a highly conductive and porous CNC layer containing GNP was fabricated on both sides of the Nafion membrane via the layer-by-layer (LbL) self-assembly technique, to enhance the overall bending performance of the IPMC actuator. The cationic and anionic materials used for the ISAM CNC fabrication were the inactive long chain poly(allylamine hydrochloride) (PAH, Sigma-Aldrich) polycation and GNP colloid (Purest Colloids, Inc.) with negative surface charge. The pH of a 10 mM PAH aqueous solution was adjusted to 4.0 (±0.1), by adding HCl or NaOH solutions, and the GNP colloid was used as received (pH=8.0). The LbL coating started by alternately dipping the framed Nafion membrane in a PAH solution and then GNP colloid to form one bilayer. The electrostatic attraction of each solute to the oppositely-charged surface provided strong, rapid adsorption of a nanoscale layer of the solute onto the surface. The thickness of every single layer was automatically regulated through surface charge reversal. Each PAH and GNP coating step was followed by three 1 minute deionized (DI) water rinsing steps. This removed any excess coating

material deposited during the prior step that was not strongly bound by electrostatic attraction. The CNC fabrication process was terminated once the desired thickness (number of bilayers) was achieved. The automatic dipping system (Figure 2.2) was used for all the CNC LbL fabrication. The coated membrane was then left in the air overnight for drying and ready for IL absorption.

In order to get an even coating on the highly soft and flexible thin Nafion membrane, polycarbonate frames with 1 inch by 2 inch opening were used to hold the membrane during the LbL dipping. Originally, the membrane was clamped between two such frames by stapling. With this configuration, however, the GNP degraded rapidly during the LbL fabrication, as shown by the significantly changed colloid color and the clearly obvious precipitate on the bottom of the beaker, see Figure 3.1. The obvious suspects contaminating the GNP colloid were the metal staples and thus a newly designed plastic "zip-loc" frame was proposed and fabricated, as shown in Figure 3.2. By eliminating the usage of metal staples, the GNP colloids maintained good quality for a longer time (up to 6 hours or 30 BL of ISAM deposition) during LbL fabrication (Figure 3.3). A thicker and more homogeneous CNC coating was also obtained on Nafion membrane using this procedure, as shown in Figure 3.4 and 3.5. Figure 3.5 also demonstrates the correlation between the thickness of the CNC and the number of bilayers. A Veeco Dektak 150 profilometer was used to determine the thickness of the PAH/GNP CNC, which was deposited on glass microscope slides in this case for more accurate measurement, with the assumption that the CNC on Nafion had a similar thickness.

Figure 3.1. Degradation of GNP colloid caused by staples on the original frame configuration. Left: fresh GNP colloid; Right: GNP colloid left overnight with two staples in it.

Figure 3.2. Frame with plastic zip-loc design for LbL CNC fabrication.

Figure 3.3. GNP colloid after 10 BL CNC fabrication using new zip-loc frame (left container) and old stapled frame (right container). The middle container is the fresh GNP colloid for reference.

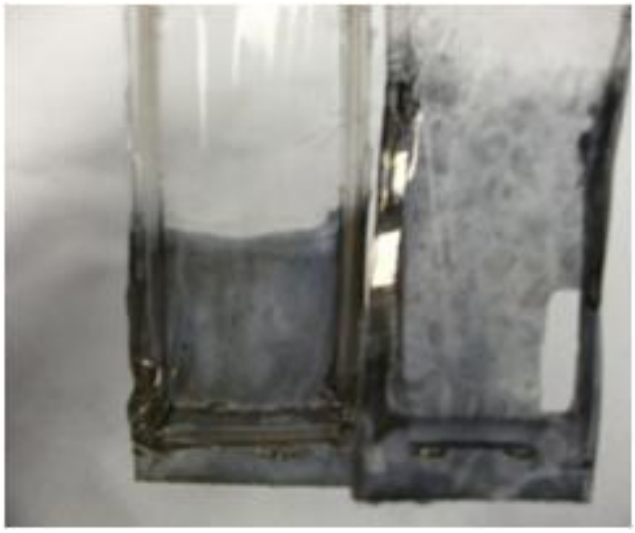

Figure 3.4. 30 BL of PAH/GNP CNC coating fabricated by using new zip-loc frame (left) and old stapled frame (right).

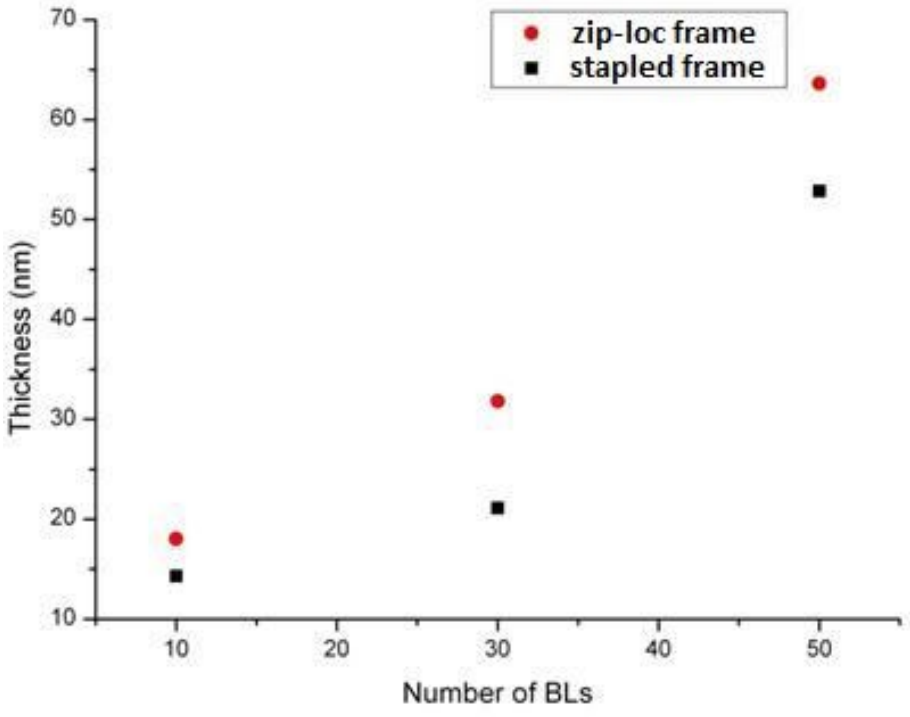

Figure 3.5. Correlations between the thickness and number of bilayers (BLs) of the PAH/GNP CNC fabricated via LbL self-assembly.

3.1.3 Ionic liquid (IL) as electrolyte

The incorporation of IL into the *i*EAP membrane with ISAM CNC coatings was performed by submerging the membrane into the IL at elevated temperature. More electrolyte generally enables larger bending due to increase in mobile ions, but the amount of the IL (quantified as the weight percent uptake wt. %, see Eq. 3-1) that can be soaked into the membrane is limited by a couple of factors.

$$wt.\% = \frac{W_{IL}}{W_{Nafion+CNC}} \tag{3-1}$$

$$W_{IL} = W_{IL+Nafion+CNC} - W_{Nafion+CNC}$$

Generally speaking, for a certain *i*EAP membrane and type of IL, the amount of IL soaked into the membrane increases as time goes by, and the maximum amount of IL that can be swollen into the membrane is determined solely by the temperature. However, the temperature was usually controlled to be below the threshold at which the physical properties of the membrane or CNC start changing. Typically, the soaking temperature was kept below 110 °C, because we have found that the CNC starts to dissolve above that temperature. Some *i*EAPs may need even lower soaking temperature to prevent degradation of their mechanical properties. Table I shows the dependence of the IL uptake and the soaking temperature for a Nafion membrane with different CNC thickness as an example; all the samples were soaked in EMIm-Tf IL for 20 minutes, which was found to be long enough to reach the maximum uptake at a given temperature.

Table I. IL uptake (in weight percent) in a Nafion membrane with different CNC thickness when soaking at 50 °C and 110 °C for 20 minutes.

	0 BLs	**20 BLs**	**30 BLs**	**40 BLs**	**50 BLs**
50 °C	24.8%	25.8%	26.3%	27.0%	27.2%
110 °C	34.3%	37.5%	39.7%	40.8%	41.3%

It can be clearly seen that, more IL can be incorporated into the membrane at higher temperature. In addition, a thicker CNC also contributes to a larger amount of IL incorporation. This is because the porous structure of CNC can accommodate the absorption of IL.

3.1.4 Fabrication of outer electrodes

The outer electrodes connected to the power supply in the current studies were fabricated by hot-pressing gold foil on both sides of the CNC-coated ionomer membrane. To do this, the *i*EAP membrane with CNC was sandwiched between two pieces of 50 nm thick gold foil. For the Nafion case, a press force of 700 lb (Digital Load Cell E-Z Press^{TM} with Heated Platens, International Crystal Laboratories) was then applied onto the membrane at 90 °C and the gold foil firmly adhered to the membrane. Finally, the membrane was cut into 1 mm × 10 mm strips for actuation tests. The final five layer structure of the IPMC actuator is schematically shown in Figure 1.1.

3.2 The characterization of Nafion membrane-based IPMC actuators

3.2.1 Bidirectional bending and two-ion model

For the actuation test, one end of the actuator was clamped between two external electrodes while the other end is left free to move. For all the actuator samples, a DC step voltage (μAutoLab III/FRA 2 Impedance Analyzer, Metrohm Autolab) was applied and the bending behavior was recorded by an HD CCD camera (SONY HXR-MC1) with 30 fps. When the actuator bends, it forms an arc. By measuring the distance between the clamp point and the free end of the actuator before and after the bending, the curvature of the bending can be calculated by $K=R^{-1}$, where R is the radius of the bending arc. A larger curvature corresponds to more bending, as illustrated in Figure 3.6.

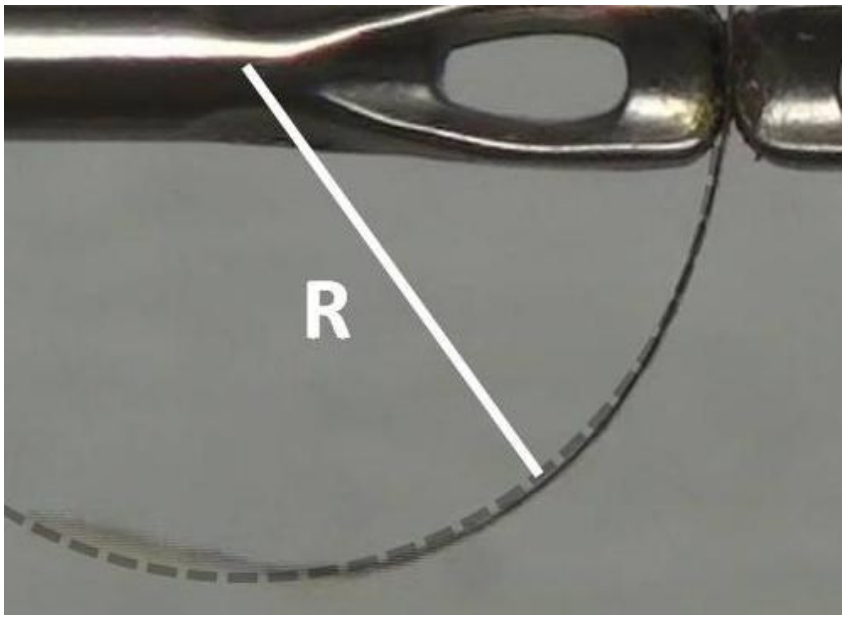

Figure 3.6. The bending amplitude of IPMC actuator is characterized by the bending curvature, which is defined as $K=R^{-1}$.

In early work, it was reported that IPMC actuators bended only toward the anode under a DC applied voltage since the bending was caused by the migration and accumulation of cations

only, which was consistent with the general understanding of Nafion as a cation permeable polymer.[1] However, a bidirectional bending behavior was observed by our research group in ionic liquid-containing IPMC actuators,[2] which implied a more complicated bending mechanism relating to the ion transport and accumulation in the actuator. To be more specific, under the external electric field, the cations and anions of the IL travel through the Nafion membrane in opposite directions and accumulate at the interface between the electrodes and the Nafion membrane on the cathode and anode sides, respectively. The ion distribution within the actuator experiences a transition from a random, neutral mixture to a forced separation. Any imbalance (size, number, and/or speed) between the cations and anions during this process will result in a differential swelling and contraction between the two sides of the actuator, and thus cause a bending motion. With an applied DC voltage (steady external electric field), the actuator shows a fast but smaller bending toward the anode, which is followed by a slow but larger bending toward the cathode. This bidirectional bending behavior strongly suggests that, in the IPMC actuators with EMIm-Tf as electrolyte, the cations are smaller and move faster, while the anions are larger but move more slowly, as depicted in Figure 3.7, and the actual bending behavior can be viewed in the **Video 3.1** multimedia file.

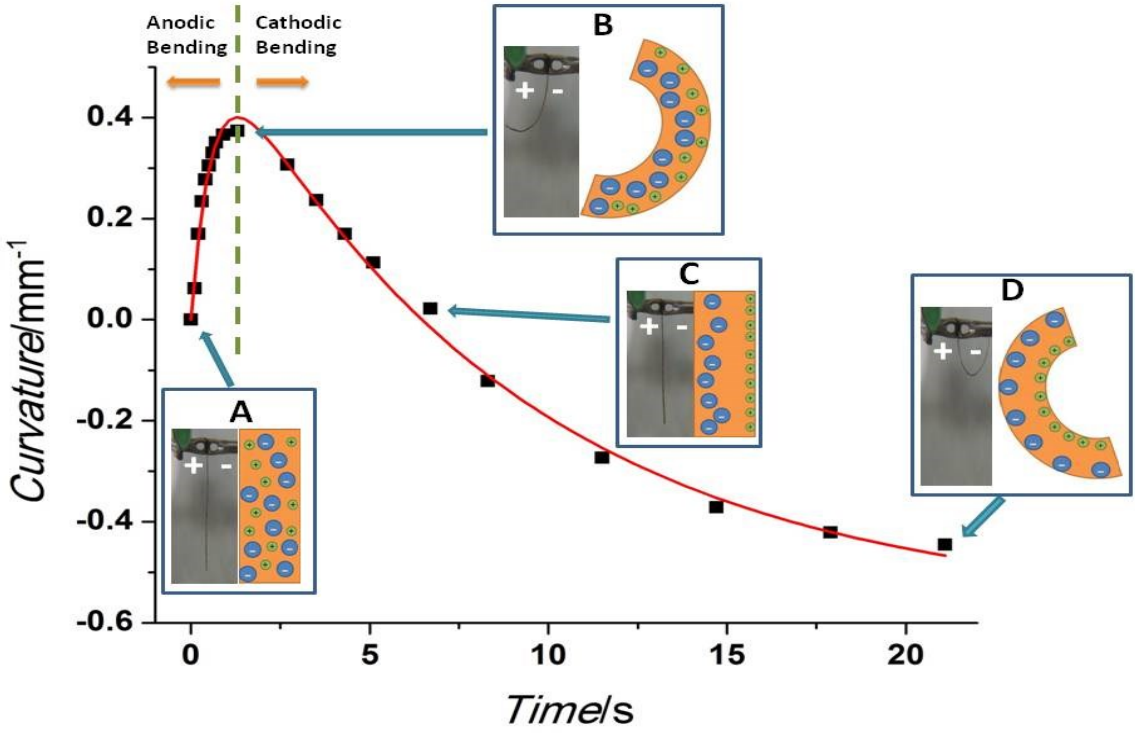

Figure 3.7. The bending curvature versus time of an IMPC actuator with 30 BL CNC and 35 wt.% uptake of EMIm-Tf IL under 4 V DC voltage. The red line is the fitting curve by using the parallel RC circuit charging equation (Eq. 3-2). The actual images and corresponding ion distribution models of the actuator in different bending stages are also depicted. The anodic bending curvature is arbitrarily set to be positive while the cathodic one is set to be negative.

When no voltage is applied, the actuator is in its equilibrium and neutral state (Figure 3.7, state A). The cations and anions are randomly distributed and the actuator is extended straight. Shortly after the voltage is applied, the faster cations accumulate on the cathode side quickly while the slower anions have hardly responded. There will be more ions on the cathode side and fewer ions on the anode side of the actuator, which causes the cathode side to expand and anode side contract, resulting in a bending toward the anode (Figure 3.7, state B), which is referred to "anodic bending". Later, as the anions migrate and many of them have moved to the anode side of the actuator, the expansion on both sides of the actuator becomes almost the same, so the

bending of the actuator will reverse and, at some point, returns to the original position (Figure 3.7, state C). Finally, after all the ions complete the redistribution and reach equilibrium, the anode side of the actuator will take more volume compared to the cathode side, due to the size difference between the anions and cations, which results in a bending finally toward the cathode (Figure 3.7, state D). This part is referred to "cathodic bending".[3]

It is worthwhile to note that, unlike the widely reported back relaxation behavior which is believed to be related to the spontaneous diffusion effect of ions,[4,5] the cathodic bending after the initial anodic bending is the physical result of the motion and accumulation of the anion from the IL. Thus, the actuator will reach its maximum bending toward cathode and keep that curvature as long as there is a constant voltage supply, and the bending curvature is directly related to the applied voltage.

Under applied voltage, the migration of the ions in the actuator (and thus the bending of the actuator) can be simulated by charging of a parallel RC circuit, as shown in Figure 3.8.[2]

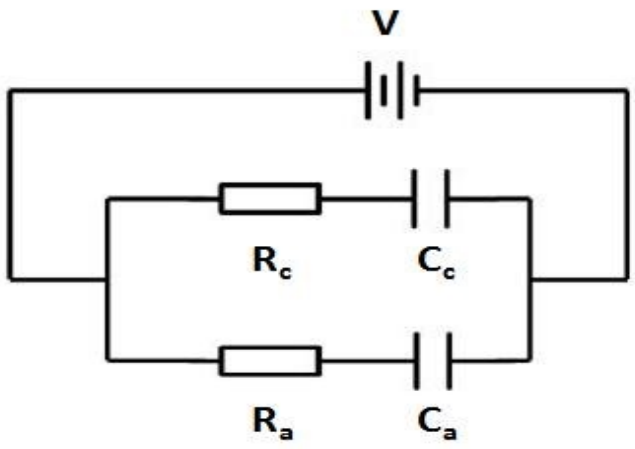

Figure 3.8. Equivalent parallel RC circuit used to fit the bending curvature versus time of the IMPC actuator. The two parallel branches stand for the cation and anion related bending, where $R_{a/c}$: resistance exerted on the anions/cations during migration; $C_{a/c}$: capacitance relating to the accumulation of anions/cations.

The cationic and anionic branches of the parallel RC circuit represent the migration and accumulation of cations and anions, respectively. The capacitance of the capacitor corresponds to the number of ions that can be accommodated near the surfaces of the electrodes on both sides of the actuator, while the resistance represents the drag and friction exerted on the ions as they make their way through the ion conductive channels in the Nafion membrane toward the electrodes. Because the bending of an IPMC actuator is caused by the accumulation of ions, i.e., the charging of the actuator, the time domain bending curvature can be fitted by the charging equation of the parallel RC circuit model, as expressed by

$$K = K_a(1-e^{-t/\tau_a}) - K_c(1-e^{-t/\tau_c}) \tag{3-2}$$

wherein K_a, K_c are the fitted maximum curvature of the anodic and cathodic bending, respectively, and K is the total curvature. The second term is negative to represent the opposite bending direction as compared to the initial anodic bending. The characteristic time $\tau_{a/c}$ is the time constant that characterizes the charging (bending) speed of either branch (accumulation of either type of ions) of the system and is defined as the product of the capacitance and resistance (τ=RC). From the consideration of effectiveness, lower resistance is preferred, and it is also beneficial to fast response (smaller τ). However, in order to achieve a larger bending amplitude, the effective capacitance should be large, which can be achieved by having a larger amount of ions (higher uptake of IL) and more volume for ion accumulation (adding CNC layers). This trade-off needs to be taken into consideration when developing IPMC actuators for different applications. An example of fitting the bending curvature using the RC circuit charging equation (Eq. 3-2) is shown in Figure 3.7.

3.2.2 The dependence of bending curvature on the thickness of ISAM CNC

Our group reported previously a study of the dependence of the slower cathodic bending on the thickness of the CNC.[6] Figure 3.9 shows the maximum cathodic bending curvature (generated by anions) of an IPMC actuator with 40 wt.% uptake of IL as a function of CNC thickness for actuators with different numbers of bilayers comprising the CNC, including the case of bare Nafion (no CNC). Under a 4 V DC step input, the cathodic bending curvature increases approximately linearly with the thickness of the CNC. The increase of bending curvature as a function of thickness was attributed to the motion of a larger number of ions into the thicker CNCs, as thicker CNCs are capable of containing more IL and hence more ions accumulate at each electrode in the presence of an electric field due to this higher capacitance. Accumulation of a larger number of anions results in a larger volume imbalance between the electrodes; this in turn causes a larger mechanical deformation and thus curvature.

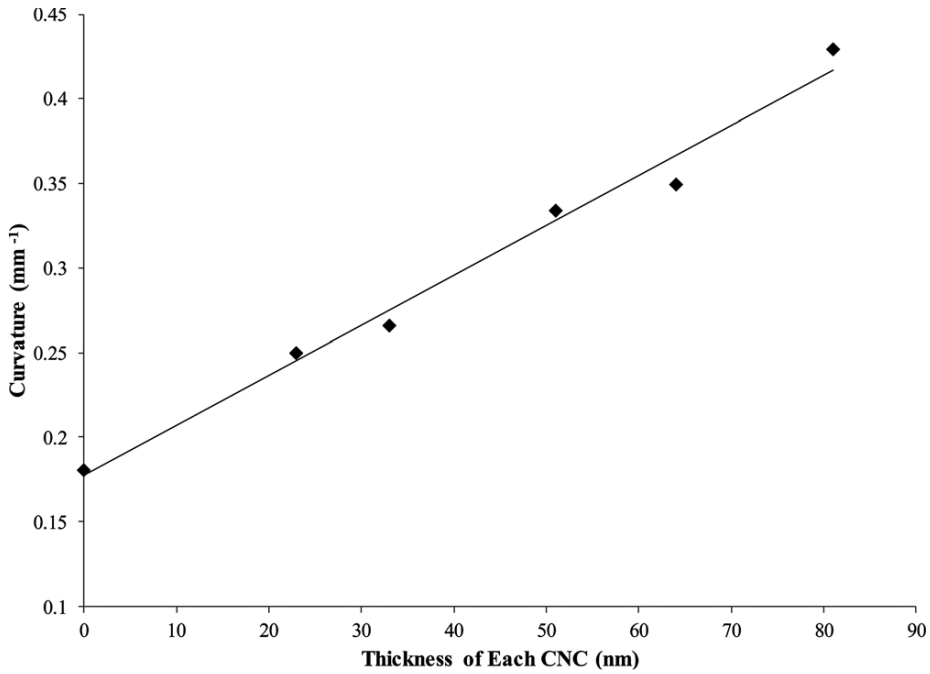

Figure 3.9. Curvature of cathodic bending increases linearly with the increase in the thickness of CNC. Data are taken under application of 4 V step input.[6]

As a following work, we have also found that the curvature of fast anodic bending of IPMC actuators with similar IL uptake (~35 wt.%) under a 4 V DC voltage input was larger for thicker GNP CNC. Figure 3.10 shows an approximately linear relation between the maximum anodic bending curvature and the number of BLs of the GNP CNC on the actuator, as a result of the increased number of cations that can accumulate on the cathode side CNC during the faster anodic bending.

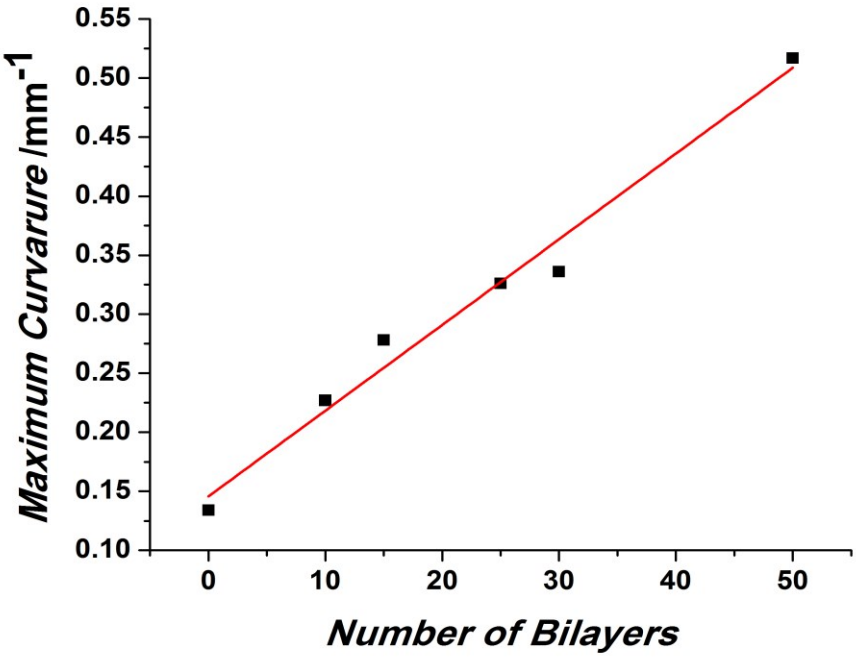

Figure 3.10. Curvature of anodic bending increases linearly with the increase in the thickness of CNC (shown as number of bilayers). Data are taken under application of 4 V step input.

3.2.3 The dependence of blocked force on the thickness of the ISAM CNC

Besides the bending curvature, another factor important to the application of IPMC actuators is the blocked force that can be generated. It is defined as the maximum force

generated by the actuator when its tip is blocked from bending at its original position. In order to characterize the influence of the CNC on the blocked force, IMPC actuators with no CNC (0 BL), and with 20, 30, 40, 50 BL GNP CNC were prepared with similar IL uptake (~35 wt.%) and the blocked force of both anodic and cathodic bending was measured with a load cell (GSO-10, with TMO-1 amplifier/conditioner module, Transducer Techniques), as shown in Figure 3.11. It can be seen in Figure 3.12 that, with the same amount of IL uptake, or in other words, with the same amount of ions available, actuators with thicker CNC (larger number of BL) generated larger blocked force, for both the anodic and cathodic bending cases, as a result of more space for ions to accumulate in the thicker CNC. Since the area of the actuators were 10 mm^2, the maximum force per unit area (stress) obtained in the actuator with 50 BL CNC were 1.2 Pa and 1.7 Pa for anodic and cathodic bending, respectively.

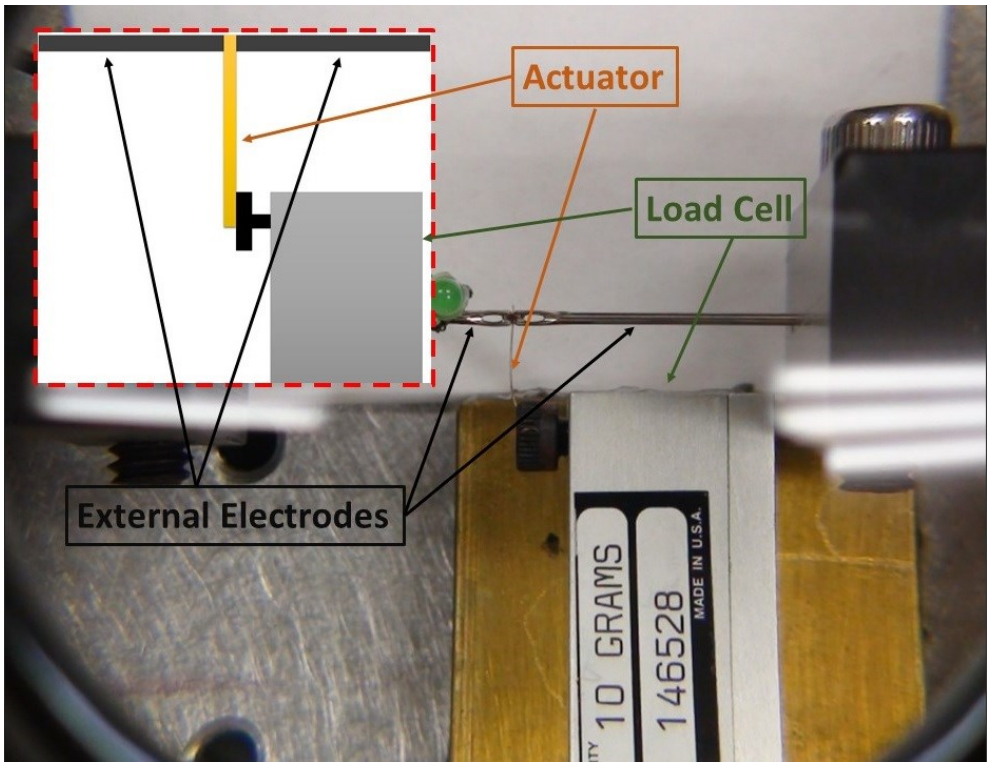

Figure 3.11. The setup for blocked force measurement. The inset is the schematic illustration of the actual setup in the image.

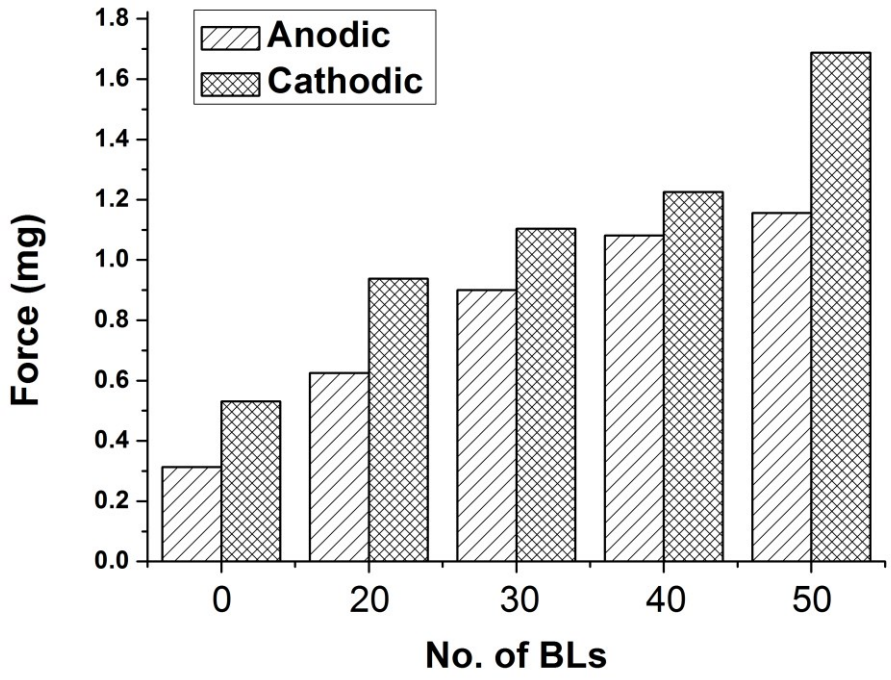

Figure 3.12. Blocked force of anodic and cathodic bending of the IPMC actuators with different number of BLs in the CNC.

3.2.4 The dependence of bending curvature on IL uptake

In order to investigate the effect of the amount of ionic liquid and the CNC layer on bending performance, two series of IPMC actuators were fabricated and tested: A. actuators made from Nafion membranes without a CNC layer, were soaked with EMIm-Tf IL to weight uptakes of 0%, 9%, 21% and 29.5%; B. actuators made from Nafion membranes coated with a 20 BL CNC layer were soaked with same IL to weight uptakes of 0%, 17.3%, 30.1% and 35%.

By fitting the bending performances with Eq. 3-2, the values of the maximum curvature of the anodic and cathodic bending can be obtained and summarized in Table II and Table III, and demonstrated in Figure 3.13.

Table II. Fitted maximum anodic and cathodic curvatures of Nafion actuators with 20 BL GNP CNC layers.

ILs weight uptake	0%	17.3%	30.1%	35%
K_a (mm^{-1})	0.04	0.68	3.26	4.72
K_c (mm^{-1})	0.40	1.17	4.66	5.62

Table III. Fitted maximum anodic and cathodic curvatures of actuators made of Nafion only.

ILs weight uptake	0%	9%	21%	29.5%
K_a (mm^{-1})	0.22	1.45	1.64	1.44
K_c (mm^{-1})	0.3	1.92	2.22	2.02

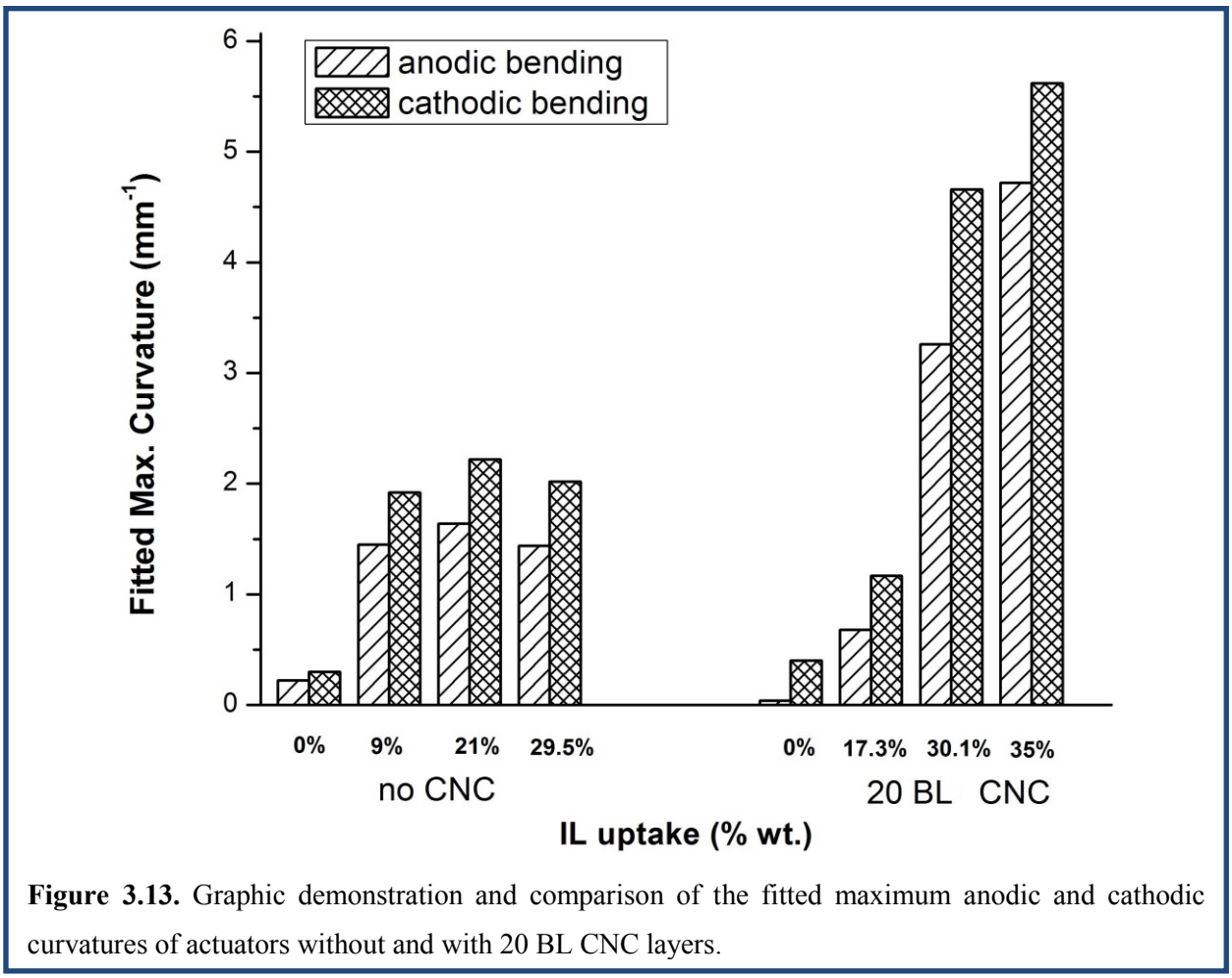

Figure 3.13. Graphic demonstration and comparison of the fitted maximum anodic and cathodic curvatures of actuators without and with 20 BL CNC layers.

From Table II, it can be seen that the maximum fitted curvatures (both for the anodic and cathodic bending) are larger for the actuators with CNC layers containing more IL (up to 35

wt.%). This is expected since more IL provides more ions for accumulation at the electrodes to enhance the bending. However, under the same conditions, as shown in Table III, the performance improvement of actuators without CNC layers saturates when the IL uptake reaches around 10 wt.%. This suggests that, in this case, even as more mobile ions are incorporated into the actuator, the ion accumulation is saturated at the electrodes at a weight uptake of ~10%. This demonstrates the role of the CNC layers to provide a porous reservoir for ions. The CNC increases the capacitance and can thus accommodate the accumulation of more ions near the electrodes, which in turn boosts the overall bending curvature of the actuator. The clear difference of these two cases is graphically demonstrated in Figure 3.13. It is noteworthy that with low IL uptake (< 20 wt.%), the bending curvatures generated by actuators with CNC layers are smaller than the one from actuators without CNC; this is probably due to the stiffness of CNC layers that add to the actuator. Only with high IL uptake, can benefit from the accumulation of a larger amount of mobile ions outweigh the passive stiffness of the CNC layers.

3.3 Modified equivalent circuit modeling of the IPMC actuators

3.3.1 Influence of water content

It is well known that the water content plays an important role in the ionic conductivity of Nafion membrane.[7-9] As discussed in section 2.2.1, the incorporation of water into the Nafion membrane not only promotes phase separation between the hydrophilic SO_3^- end group and the hydrophobic Teflon backbone of the polymer to provide channels for ion migration, but also helps to dissolve the H^+ ions associated to the end group to provide an effective electrolyte for Nafion IPMC actuator even without IL. Clearly, more water generates wider channels for the

ions to migrate through the polymer network more easily and results in a faster and larger bending of the actuator. This is especially true for the actuators without IL, where dissolved proton (H^+, or hydronium) and electrolyzed hydroxyl (OH^-) group are the working ions.

To investigate the correlation between the performance (both mechanical and electrical) of IPMC actuators and the ambient humidity, which directly affects the water content in the actuator, the entire actuation probe station was enclosed by a homemade humidity chamber (Figure 3.14). The humidity in the chamber was increased by a commercial ultrasonic humidifier (no heating) and decreased by inducting pure nitrogen gas. The humidity was monitored by a Fluke 971 hygrometer. All the tests corresponding to a given humidity were performed after the fluctuation of humidity was kept within ±1%.

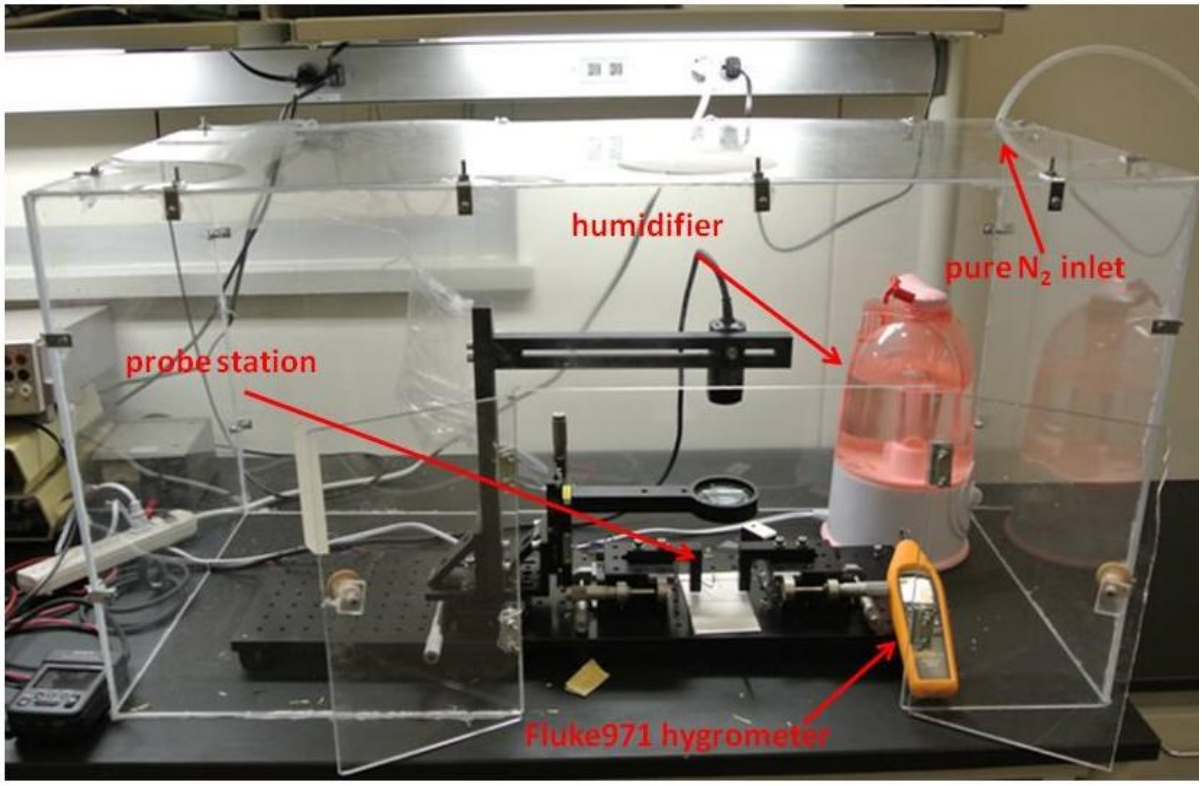

Figure 3.14. Homemade humidity chamber for humidity control and maintaining.

Figure 3.15 shows the bending performance of a Nafion IPMC actuator with 30 BL CNC and no IL under 4 V DC step input at different relative humidity, where faster and larger bending was generally achieved at higher humidity. The decreased curvature at 90% humidity was due to the observable water condensation on the surface of the actuator. In this case, the bending of the actuator without IL was too small to be observed when the humidity is lower than 60%. Figure 3.16 shows the bending performance of a Nafion IPMC actuator with same CNC thickness but with 37 wt.% uptake IL. It can be seen that the actuator in a higher humidity environment (60%~80% range) clearly showed faster and larger bending as a result of higher ionic conductivity of the Nafion membrane with higher water content. Note that at very high humidity levels (85% and 90%), the clear water condensation on the actuator surface during tests resulted in the performance degradation of the actuators.

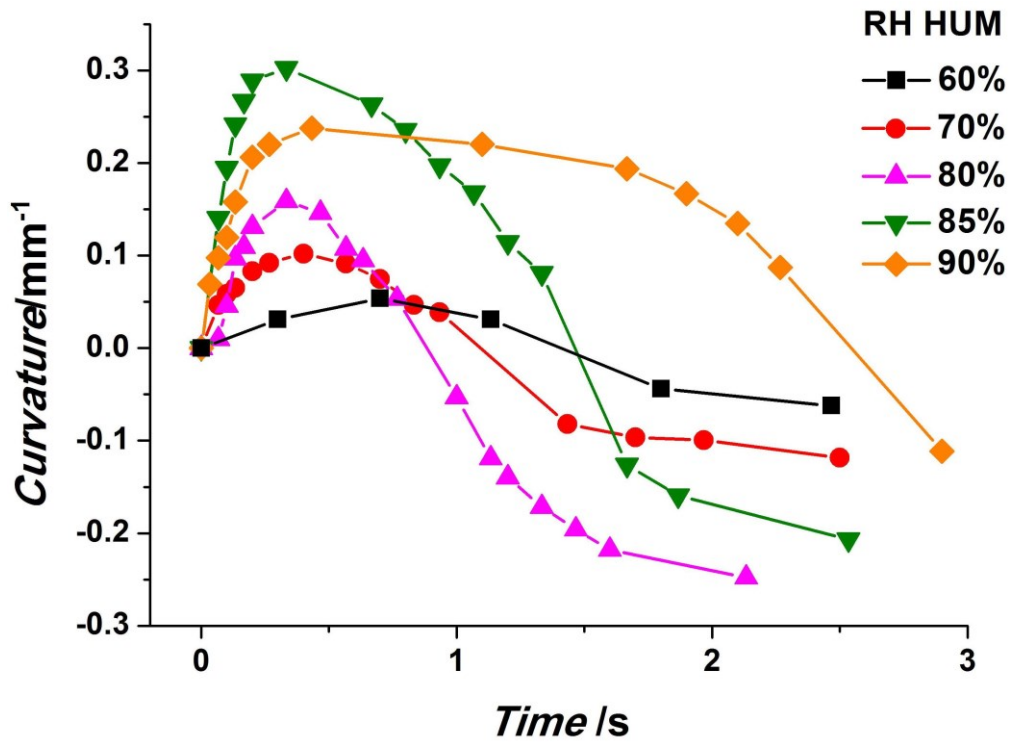

Figure 3.15. Bending curvature vs. time of an actuator with 30 BL GNP CNC layer and no IL under 4 V DC input in different relative humidity.

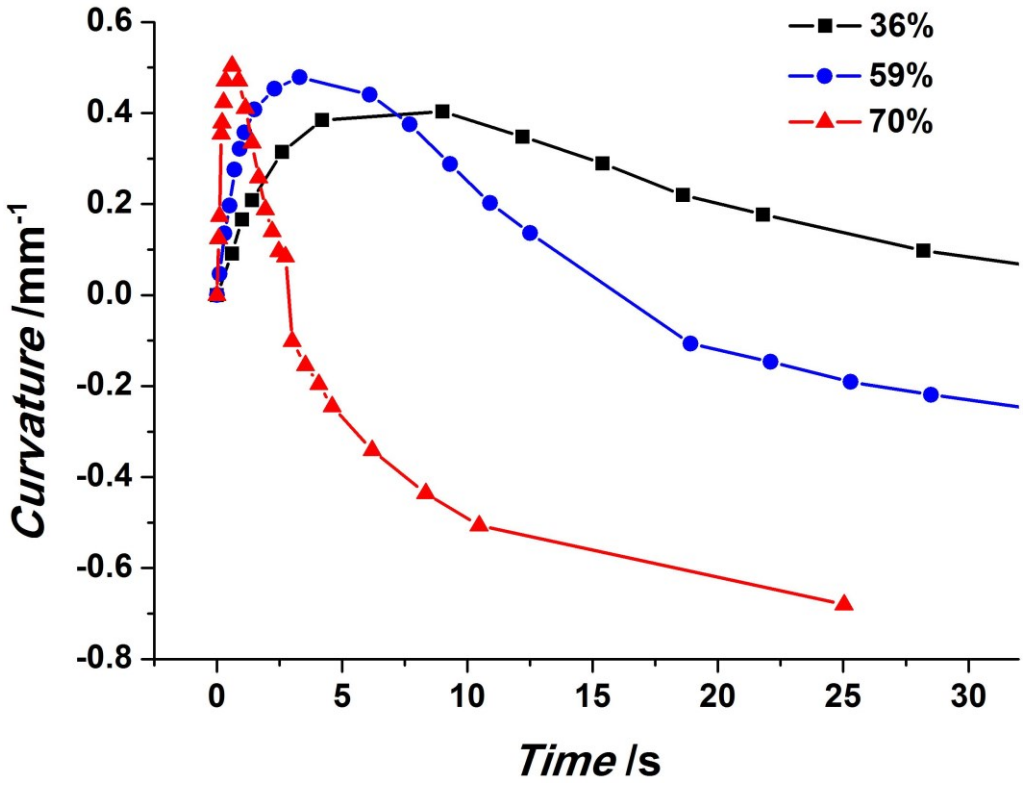

Figure 3.16. Bending curvature vs. time of an actuator with 30 BL GNP CNC and 35 wt.% IL under 4 V DC input in different humidity.

Water also affects the electrical properties of the IPMC actuators. After the DC input was applied, a very fast rise followed by a fast current drop through the actuator was observed at first, which correlates to the ion migration resulting from the external electric field. Then, after the ions finished the redistribution and the bending reached its final position, the current slowly decreased to and maintained a steady magnitude for an extended time instead of approaching zero, even though there was no more bending motion of the actuator. As an example, Figure 3.17 shows the charging current through a typical Nafion IPMC actuator with GNP CNC; the current after the initial drop remained constant for over 5 minutes. The voltage was kept on for tens of minutes and no clear change in the current was observed. This clearly excludes ion accumulation as the source of this current. Moreover, it was found that the steady-state current closely relates

to the humidity of the environment in which the testing was performed. For these reasons, we conclude that this steady-state current is caused by the electrolysis of the water adsorbed by the actuator from the ambient environment. Right after a DC voltage was applied, the charging current was mainly determined by the ion transport of the IL. Then, because the operation voltage of the actuator (4 V) was higher than the water electrolysis threshold (~1.3 V), the charging current was only determined by the electrolysis of water in the actuator once the transport and accumulation of the ions were complete, i.e., the bending reached its steady state point. After the initial fast current drop, the dynamic balance between the adsorption of water vapor and the consumption of water during the electrolysis resulted in a steady current, which depends on the humidity of ambient environment.

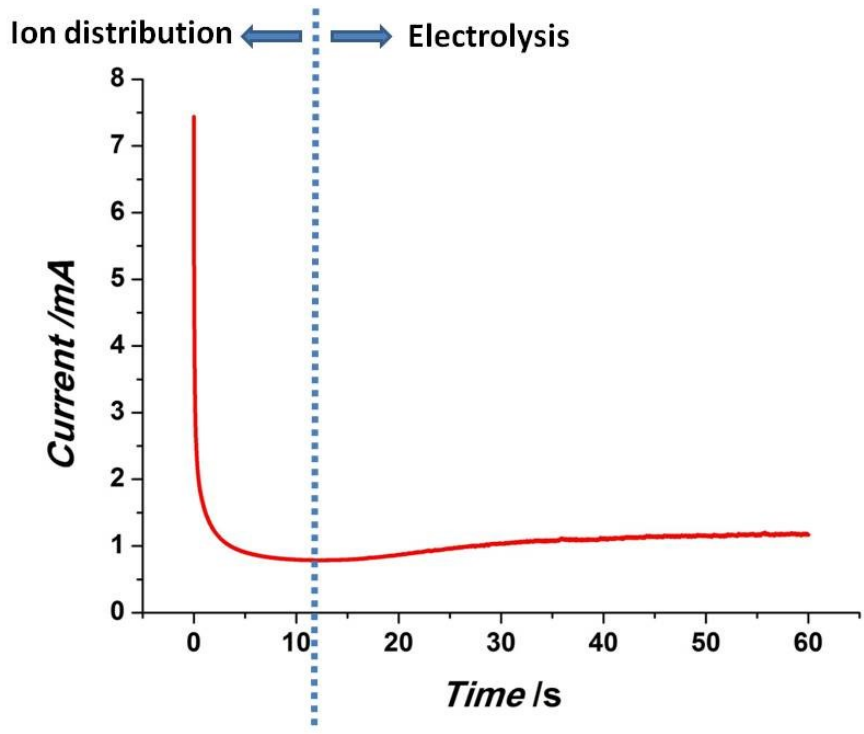

Figure 3.17. Typical charging current curve of a device under applied DC voltage at fixed humidity.

The electrolysis current through the IPMC actuator clearly depends on the applied voltage, as shown in Figure 3.18; and is roughly proportional to the surface area of the device, shown in Fig. 3.19. For a certain applied voltage (less than 4 V), the relationship between the electrolysis current and the environmental humidity can be easily calibrated according to the size and surface area of the Nafion IPMC actuator.

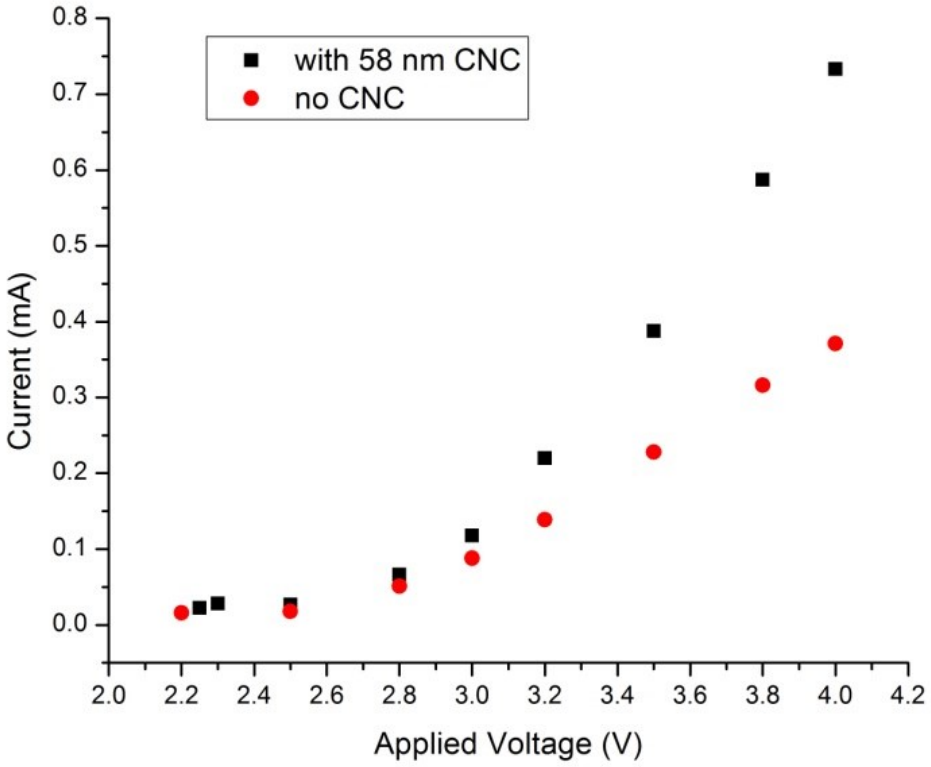

Figure 3.18. The dependence of the electrolysis current on the applied voltage, measured on Nafion IPMC actuators with/without the CNC coating.

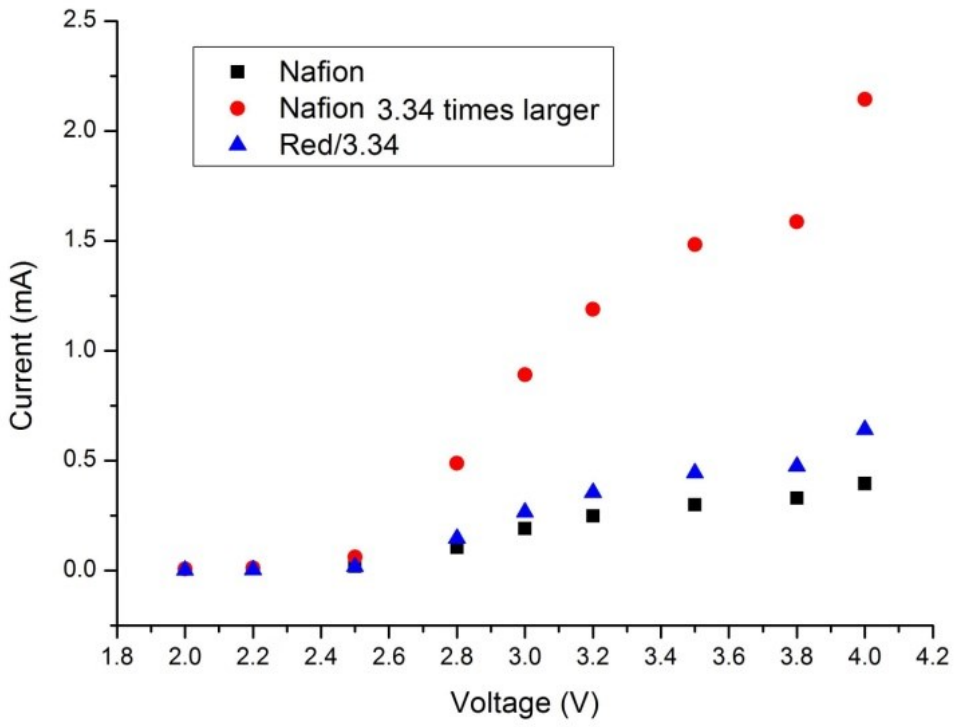

Figure 3.19. Nafion IPMC actuator with larger area (1 mm × 33.4 mm) has larger electrolysis current and the current is roughly proportional to the area.

From Figure 3.18, it can also be seen that the electrolysis current was larger when the CNC was present. There are two possible reasons for this. First, the porous structure of CNC may increase the effectiveness of absorbing moisture from the ambient environment; second, the highly porous and conductive CNC coating also serves as an electrode such that the electrolysis process may also take place at the surface of gold nanoparticles so that the overall effect is amplified. The humidity-dependent electrolysis current can be found with or without the CNC layer, but the sensitivity is higher with the CNC presence.

The dependence of the electrolysis current under 2.5 V DC input through an Nafion IPMC actuator with 30 BL CNC and 35 wt.% IL uptake on the ambient environment humidity can be

clearly seen in Figure 3.20. The amplitude of the steady electrolysis current distinguishes between humidity changes of just a few percent, and the current increases in a manner closely correlated with increased humidity.

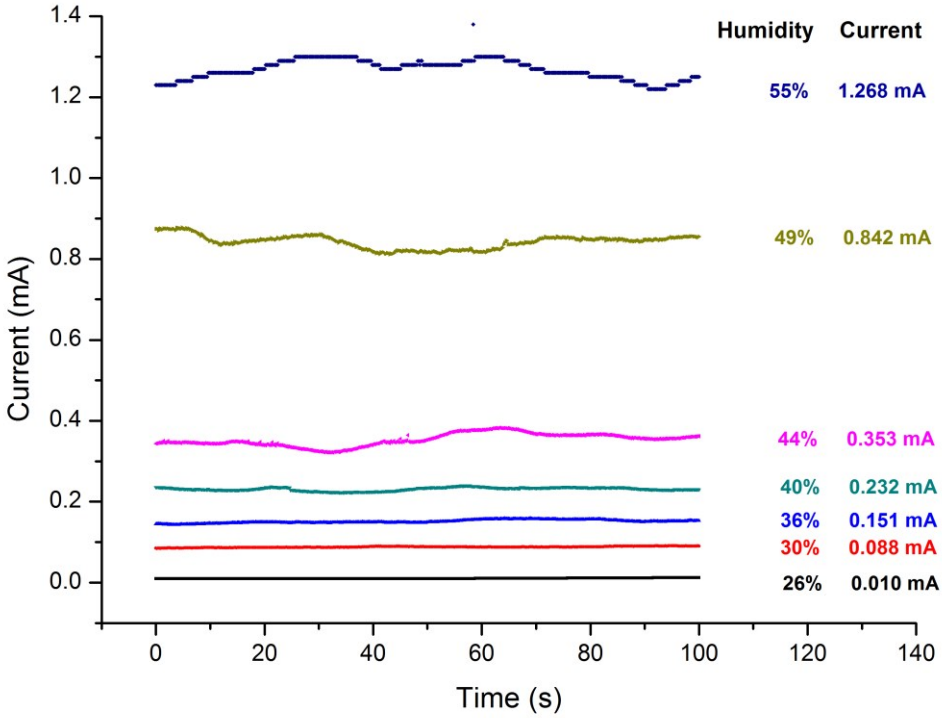

Figure 3.20. Electrolysis current through the Nafion IPMC actuator (30 BL, 35% wt. IL uptake) at different humidity levels. The listed current is the average value over 100 seconds.

A comparison of the responses to a sudden change in humidity between the Nafion IPMC actuator and a commercially available regular digital hygrometer (Sper Scientific 800016) is shown in Fig. 3.21. During the test, the Nafion IPMC actuator and this commercially available hygrometer were placed side-by-side in the humidity chamber. The humidity in the lab room outside the chamber was kept at 26% and the humidifier was used to increase the humidity in the chamber. At first, the humidity was elevated to 55% and held until both the current through the

Nafion IPMC actuator and the reading on the hygrometer became steady. Then the humidifier was turned off and the door of the chamber was opened to the lab room environment in order to let the humidity drop to 26%. As soon as the door was opened, a steep change of the electrolysis current through the Nafion IPMC actuator can be observed, as shown in Fig. 3.21A. In the meantime, a timer was started and the reading on the commercial hygrometer was recorded. It can be seen that the electrolysis current through the Nafion IPMC actuator rapidly decreases from the value corresponding to 55% humidity to the one corresponding to 26% humidity in approximately 80 seconds. Considering that the actual humidity in the chamber after the door was opened requires a certain time to reach the steady value of humidity in the room, the current through the Nafion IPMC actuator most likely accurately reflects the local humidity on a time scale of seconds or less. In comparison, the reading of the commercial digital hygrometer took nearly 30 minutes to reach 26%. In other words, the response of the Nafion IPMC actuator to a sudden humidity change is more than 20 times faster than this commercially available regular digital hygrometer.

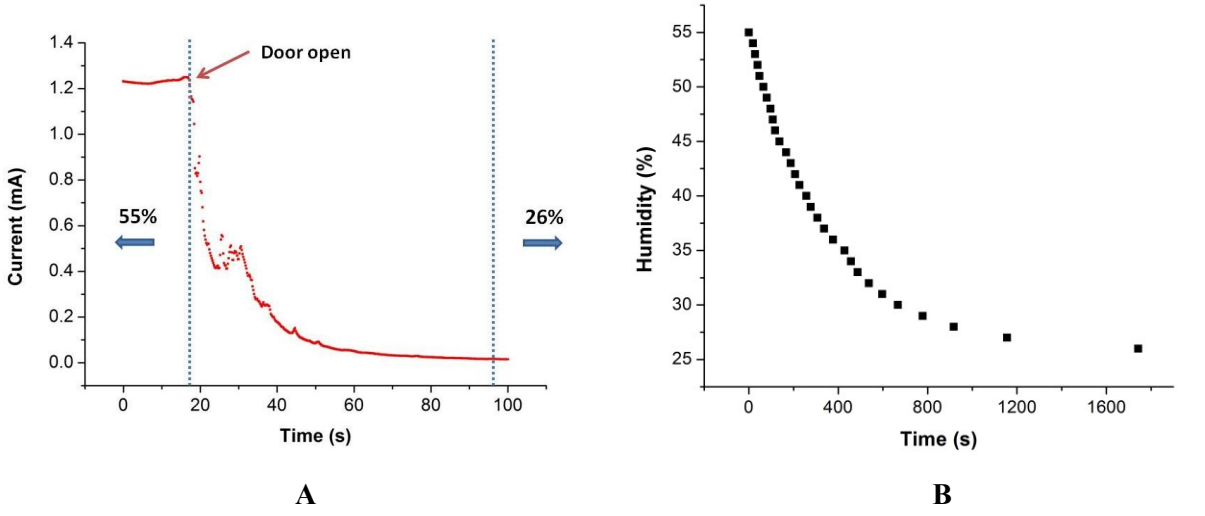

Figure 3.21. The response from the IPMC actuator (A) and commercially available digital hygrometer (B) to a humidity change from 55% to 26%. Note the different time scales in (A) and (B).

Due to the discovery of such a highly sensitive relationship between the electrolysis current through the Nafion IPMC actuator and the ambient humidity, and the advantage of the much faster response to the humidity change over the commercial available hygrometer, a new humidity measuring device was proposed with easy concept, low cost, small size and low voltage operation (~3 V), which suggested a new type of portable fast hygrometer suitable for the real time monitoring of rapid humidity change or fluctuation. This idea has been filed in a Virginia Tech Intellectual Property (VTIP) Disclosure.

I would like to point out that, although the professional Fluke971 hygrometer used for humidity monitoring in our experiments can have a comparable fast response, this type of hygrometer utilizes the change of capacitance as opposed to the current used in our proposed device. The more complicated measurement of capacitance makes such hygrometers expensive (~$300).

3.3.2 Modified equivalent circuit model

As discussed in section 3.2.1, in our previous study, an equivalent circuit model was proposed to simulate the electrical and mechanical properties of the Nafion IPMC actuator, where two RC branches in parallel represent the cationic and anionic contribution.[2] The capacitor relates to the charge storage and the resistor corresponds to the drag felt by the ions during migration through the polymer network. The bending curvature of the actuator is proportional to the ions accumulated in the CNC, so the bending curve can be fitted very well with the capacitor charging equation of the equivalent circuit. However, this model does not include the influence from the water content. As discussed in the last section, there was a steady electrolysis current

through the Nafion IPMC actuator after the initial charging was complete and this current could not be represented with the old model. Thus, a modified equivalent circuit model to better simulate the electrical property of the IPMC actuator is proposed here, as shown in Figure 2.19. This model adds a "leakage" resistor "r" to represent the equivalent resistance of the water electrolysis process. Based on this model, the charging current through the IPMC actuator under a DC voltage can be expressed as:

$$I = V_0[\frac{C_a}{\tau_a}e^{-t/\tau_a} + \frac{C_c}{\tau_c}e^{-t/\tau_c} + \frac{1}{r}] \qquad (3\text{-}3)$$

where the RC time constants $\tau_a = R_a C_a$ and $\tau_c = R_c C_c$. The meanings of the parameters are explained in the caption of Figure 3.22.

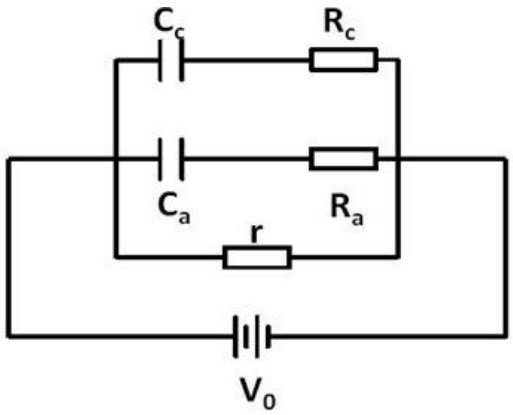

Figure 3.22. Modified equivalent circuit model for the IPMC actuator. R_a, C_a, R_c and C_c are the resistance and capacitance relating to the ion transportation and accumulation during anodic/cathodic bending, respectively. V_0: applied voltage, r: leakage resistance of the system relating to the electrolysis current of water.

When an actuator has been fully charged under a DC input (bending is completed and the current through it becomes steady) and then is disconnected from the power source, the voltage

across it does not drop to zero instantly but experiences a slow decay, which correlates to the ion redistribution in the actuator. This process can be simulated by the slow voltage drop during the discharging of the capacitors in Figure 3.22 when the RC circuit is disconnected from V_0. The measurement of this "leftover voltage" provides a new angle to probe the ion motion in the actuator and another approach to verify the proposed circuit model. By programming the impedance analyzer we use, the voltage across the actuator can be continuously monitored when the power supplied to the actuator is switched off. According to this modified circuit model, the expression of the "leftover voltage" can be then deduced as:

$$V = rV_0\left[\frac{C_a}{t_a}e^{-t/t_a} + \frac{C_c}{t_c}e^{-t/t_c}\right] \tag{3-4}$$

where $t_a = \frac{\tau_a + \tau_c + r(C_a + C_c) + \sqrt{[\tau_a - \tau_c + r(C_a - C_c)]^2 + 4r^2 C_a C_c}}{2}$, and

$$t_c = \frac{\tau_a + \tau_c + r(C_a + C_c) - \sqrt{[\tau_a - \tau_c + r(C_a - C_c)]^2 + 4r^2 C_a C_c}}{2}$$

To test this model, three identical Nafion actuators with GNP CNC coating were soaked with different amounts of EMIm-Tf IL (19.4, 28.2 and 32.6 wt.% uptake), and their charging currents and discharging "leftover" voltages were measured as shown in Figure 3.2.3 and 3.2.4, in which the external DC voltage was applied at t=0.

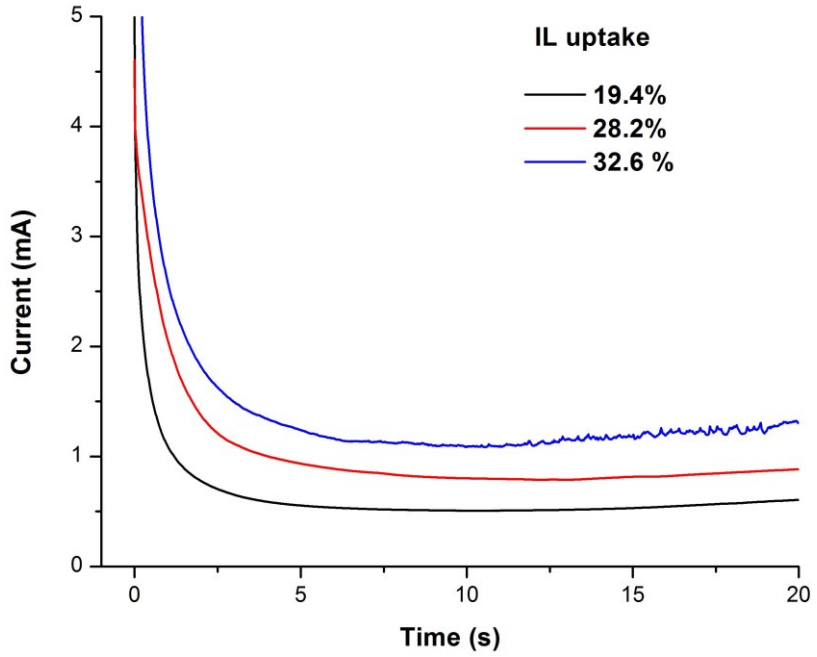

Figure 3.23. Charging current through Nafion IPMC actuators with 30 BL CNC and different IL uptake.

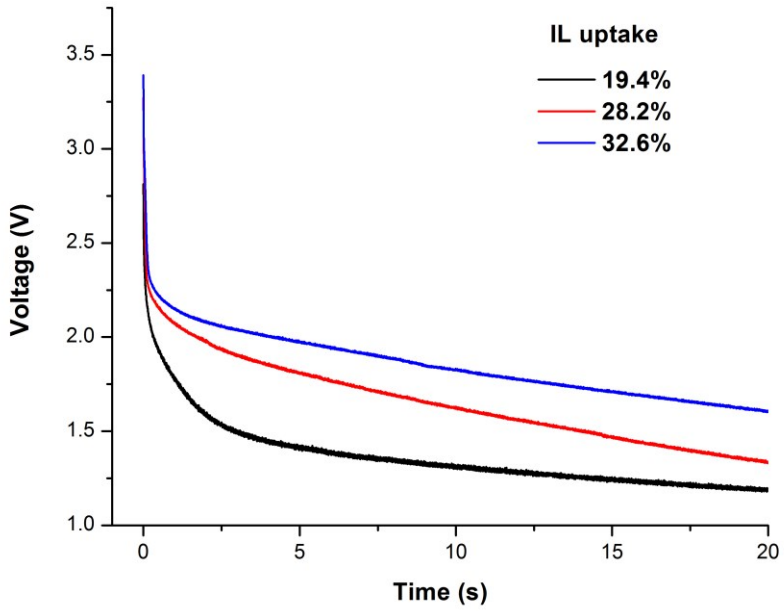

Figure 3.24. Discharging current through Nafion IPMC actuators with 30 BL CNC and different IL uptake.

Figure 3.2.3 and 3.2.4 show clear dependence of the electrical properties of the IPMC actuators on IL uptake; more IL leads to a larger charging current and slower dropped leftover voltage. The larger amount of free ions from more IL resulted in a larger charging current through the actuator. For the same reason, it would take longer time for the ions to redistribute to the evenly mixed neutral state; thus a slower leftover voltage decay was observed.

By fitting these electrical responses according to Eq. 3-3 and 3-4, the key parameters C_c and C_a were obtained. We can see a general agreement of the fitting data (with two significant digits) for charging and discharging, as shown in Table IV.

Table IV. Comparison of capacitances and leakage resistance in the circuit model (Figure 3.22) obtained by fitting the charging and discharging behavior of the IPMC actuators. $C_{a\text{-}c}$ and $C_{a\text{-}d}$: capacitance of anodic bending during charging and discharging, respectively; $C_{c\text{-}c}$ and $C_{c\text{-}d}$: capacitance of cathodic bending during charging and discharging, respectively, r: leakage resistance.

IL weight uptake [%]	19.4	28.2	32.6
$C_{a\text{-}c}$ (μF)	14	21	4.5
$C_{a\text{-}d}$ (μF)	6.1	21	8.6
$C_{c\text{-}c}$ (μF)	550	700	580
$C_{c\text{-}d}$ (μF)	1400	130	950
r (kΩ)	4.2	4.6	4.4

The general agreement (C_a~10 μF, C_c~1000 μF) was found between the fitted capacitances in charging and discharging cases within the factor of 2.6, for all the three different IL uptakes. The difference between the parameters obtained from fitting the charging and discharging behavior could result from the different ionic conducting channels in the Nafion

membrane with/without external electric field. Moreover, the leakage resistances, which relate to the electrolysis of water adsorbed in the membrane, obtained from the fitting of all three different IL uptake cases, agreed with each other very well. These show the validity of this model to a certain extent and could be a useful approach to better characterize the electrical properties of the Nafion IPMC actuator, although the IPMC is a more complex system that can be affected by multiple factors simultaneously and there is probably not a reasonably simple model that can provide excellent simulation.

3.3.3 The correlation between ion diffusion coefficients and bending performance

Since it is the ion's transport and accumulation in an IPMC actuator that causes the bending, it is intriguing to understand the correlation between the behaviors in the microscopic and macroscopic domains. This would lead to approaches for improving the performance or manipulating the reactions of the actuators. For example, Imaizumi *et al*.[10] studied the bending performance of *i*EAP actuators composed of an ion conductive polyether-segmented polyurethaneurea (PEUU) membrane incorporating either a lithium bis-(trifluoromethanesulfonyl)amide (Li[NTf_2]) salt or an EMIm-NTf_2 IL as electrolyte. They found that the bending directions of actuators containing (Li[NTf_2]) and EMIm-NTf_2 were opposite, when subjected to a voltage input with same polarity. These experimental results agreed with their NMR measurement results on the relative diffusion coefficient between the Li^+ and [$EMIm^+$] cations and [NTf_2^-] anions in PEUU, where diffusivity of [NTf_2^-] was found to be higher than Li^+ but lower than [$EMIm^+$].

By using NMR, Li *et al*.[11] of Prof. Madsen's group in the Department of Chemistry at Virginia Tech investigated the ion transport in EMIm-Tf IL swelled Nafion membranes (same configuration we used for IPMC actuator fabrication). They found that the diffusion of [$EMIm^+$] cation is faster than that of [Tf^-] anion, and the ion mobility, for both cation and anion, of the IL in the Nafion membrane highly depended on the water content in the system. The higher the water content, the larger the ion mobility. Accordingly, faster actuation response of the IPMC actuator was also obtained, as discussed in section 3.3.1.

However, the directional bending behavior is determined by the relative size and transport speed of the ion species. As discussed in section 3.2.1, the initial anodic bending followed by the cathodic bending behavior of an IPMC actuator is caused by the migration and accumulation of smaller but faster cations and larger but slower anions in the *i*EAP membrane. As a likely proof of the difference in the diffusion coefficient and size of the cations and anions, Hou *et al*.[12] of Prof. Madsen's group discovered that inside the Nafion membrane with EMIm-Tf IL, the diffusion coefficient of the cation was higher than that of the anion for a wide range of water content. In the model they proposed, the domination of large size anionic triplets reduced the anion diffusion rate because of the stronger interaction with the charged endgroups of the polymer side chain in ion conductive channels, and in the meantime generated a relative larger number of single cations to increase the cation diffusion. This scheme of smaller but faster cation and larger but slower anion is consistent with the bending behavior found on the IPMC actuator by our group before.[2]

Interestingly, for another commonly used IL electrolyte, 1-ethyl-3-methylimidazolium tetrafluoroborate (EMIm-BF_4), incorporated in Nafion, they found that the relative magnitude of the cationic and anionic diffusion coefficients was clearly reversed when the water content

crossed a certain threshold. To be more specific, while anion diffusion was slower than cation at lower water content, the same as the EMIm-Tf case, it became faster than cation at high water content due to the especially effective dissociation of anions from local electrostatic networks.[12] However, a direct proof of the correlations between such transition in microscale ion motion and the corresponding macroscale actuation was still lacking. Thus, we investigated and correlated the ion mobility of EMIm-BF_4 IL within a Nafion membrane with a range of water contents, as well as the electromechanical response of the Nafion IPMC actuators.

In order to verify this reasoning, an Nafion IPMC actuator with 30 BL CNC was fabricated and soaked with EMI-BF_4 IL (Sigma-Aldrich) to 23.9 wt.% uptake, followed by the hot-pressing of gold foil onto the outer surfaces of the membranes. After cutting the membrane into actuators, they were tested in the humidity chamber. A 3.5 V step DC input was applied and the bending performance was recorded and calculated. The bending performance of the Nafion IPMC actuator with EMIm-BF_4 IL is shown in Figure 3.25.

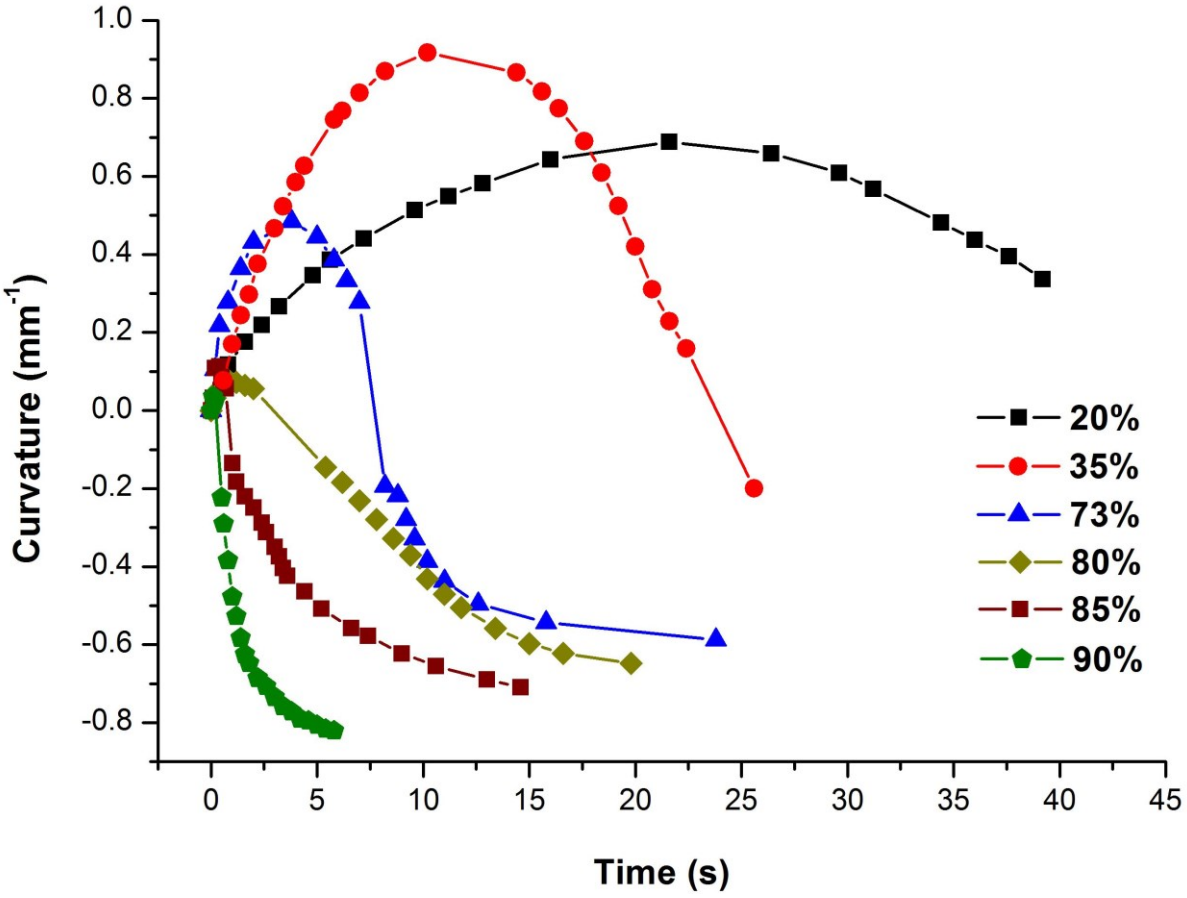

Figure 3.25. Bending curvature of Nafion IPMC actuator with 30 BL CNC and 23.9% wt. uptake EMIm-BF_4 IL under different ambient relative humidity.

It can be seen that for the lowest humidity (20%) the Nafion IPMC actuator with EMIm-BF_4 IL experienced anodic bending first after the DC voltage was applied, and then the direction reversed to become cathodic bending, similar to our observation with EMIm-Tf IL. As the humidity increased to 35%, the trend of bending remained the same except for a larger slope for both initial anodic bending and the following cathodic bending. This demonstrates that faster ion motion as the result of the higher water content does contribute to a more rapid actuation response and also causes a larger bending curvature, because more ions can migrate and accumulate in the actuator within the same time period. As the humidity was further increased to

73%, the actuation became faster still, but the amplitude of anodic bending decreased while the cathodic one was increased, which agreed with the NMR result of faster anion diffusion under higher water content. Most interestingly, when the humidity was above 80%, the bidirectional bending disappeared and only cathodic bending can be observed. This presumably corresponds to the threshold of water content in the NMR results where the ratio of diffusion coefficient of cations and anions drops from larger than 1 to smaller than 1. Above this point, higher humidity resulted in faster and larger cathodic bending only, without any observable anodic bending. This presumably occurs because the larger anions move to the anode more rapidly than the cations move to the cathode, so that the anode side is always more expanded. This proves the assumption of the combined contribution of faster individual BF_4^- anion and larger anion triplets in the literature.[12]

3.4 IPMC actuators made of other novel iEAP membranes

Although Nafion has been a favored *i*EAP membrane for IPMC actuator applications, this commercially available membrane has significant disadvantages of the lack of control over several key parameters. Recently, instead of using Nafion, we fabricated and tested IPMC actuators based on novel ion conductive imidazolium pentablock[13] and triblock copolymer membranes,[14,15] DMAEA containing ABA triblock copolymer membrane,[16] and the triblock A-BC-A polymer membrane with soft "BC" central block of DEGMEMA and imidazolium sites. All of these *i*EAP membranes were synthesized by the research group of Prof. Long in the Department of Chemistry at Virginia Tech. These *i*EAP membranes exhibit both good storage moduli and reasonable ionic conductivity, and expand the class of multiphase copolymers that are suitable for electromechanical IPMC actuator applications. Unless otherwise noted, all the

bending tests were performed in ambient environment with temperature ~20 °C and relative humidity (RH) ~45%.

3.4.1 IPMC actuator made from imidazolium-containing pentablock copolymer membrane

Because of their high ionic conductivity, acceptable affinity to ILs, and tailored structures and morphologies, imidazolium-containing polymers are promising candidates for the fabrication of electromechanical actuators. By utilizing the commercially available sulfonated pentablock copolymer Nexar™ (IEC=2.0, Kraton Polymers LLC) as a precursor, Gao[13] modified this imidazolium-containing sulfonated pentablock ABCBA copolymer through facile and quantitative neutralization of sulfonic acid sites with 1-ethylimidazolium [$EtIm^+$] cations. Thus modified Nexar pentablock copolymer contains a hydrophilic, imidazolium polystyrene sulfonate central (C) block that enables the incorporation of IL, and hydrogenated polyisoprene (B) blocks that impart membrane flexibility and elasticity, as well as the hydrophobic poly(*tert*-butyl styrene) (A) outer blocks acting as the physical crosslink to provide mechanical strength in the presence of IL (Figure 3.26).

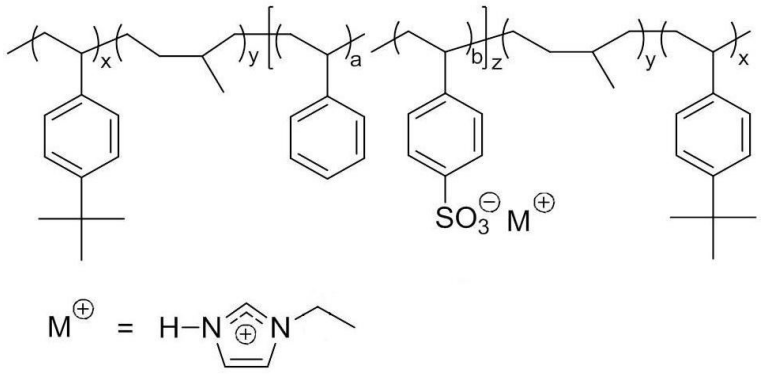

Figure 3.26. Structure of sulfonated poly(*t*-butyl styrene-*b*-styrene-*b*-hydrogenated isoprene-*b*-*t*-butyl styrene) pentablock copolymer neutralized with [$EtIm^+$] counterions (IEC=2.0).[13]

The scanning electron microscopy (FESEM, LEO Zeiss 1550) and atomic force microscopy (AFM, Veeco Multimode in tapping mode) studies performed by Gao revealed the microphase-separated morphology of this modified pentablock copolymer, as shown in Figure 3.27). This provides channels for ion transport in the actuation process. After the incorporation of EMIm-Tf IL, this copolymer membrane displayed well-defined rubbery plateaus with high storage moduli near 700 MPa as determined by dynamic mechanical analysis (DMA). This high modulus is desirable since it will generate large force during the actuation.

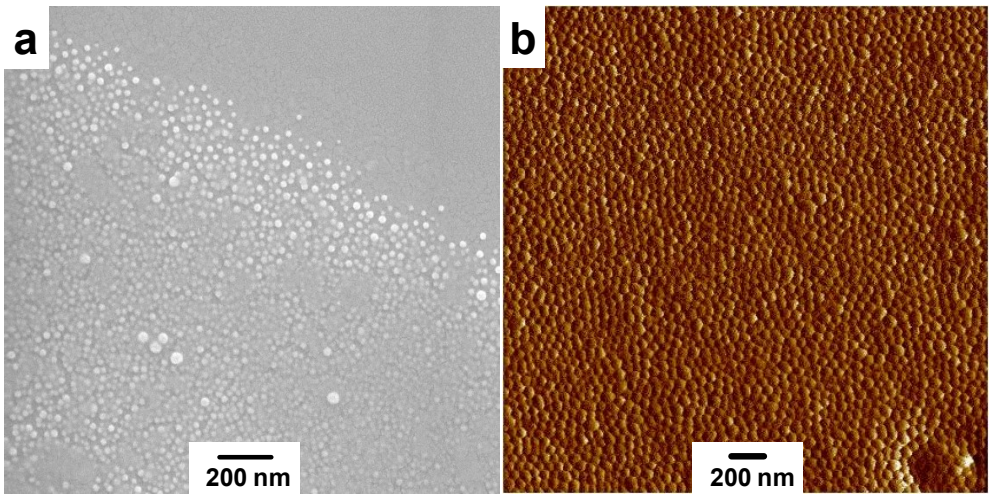

Figure 3.27. SEM (a) and AFM (b) images clearly show micellar structure formed by phase separation in the [$EtIm^+$] modified Nexar pentablock copolymer.[13]

For the IPMC actuator fabrication, this [$EtIm^+$] modified pentablock copolymer membrane with a thickness of 40 μm was first coated with 30 BL GNP CNC via LbL self-assembly, and was then soaked with EMIm-Tf IL to ~56 wt.%. (10 h at 50 °C), and finally hot pressed with gold foil as outer electrode. The bending performance of the IPMC actuators thus made is shown in Figure 3.28, in which the bending of a Nafion actuator with 30 BL CNC is also included for reference.

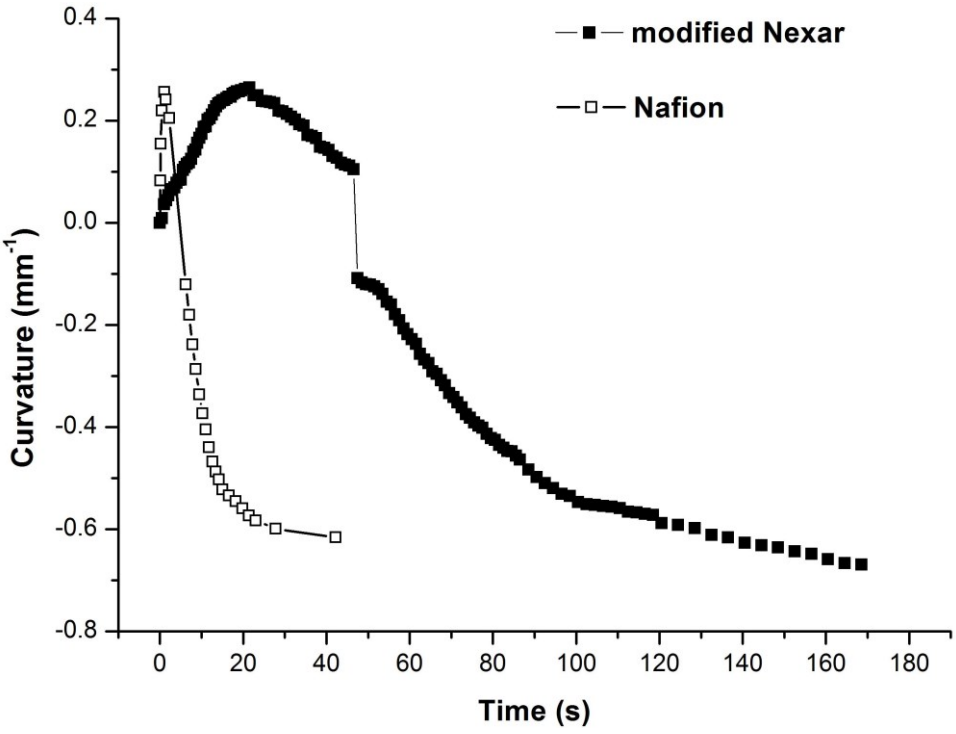

Figure 3.28. Bending curvature as a function of time of a IPMC actuator with 30 BLs CNC made from [$EtIm^+$] modified Nexar pentablock copolymer (IEC=2.0) with 56 wt.% EMIm-Tf IL under a 4 V DC input. The bending of a Nafion IMPC actuator also with 30 BL CNC but 35 wt.% EMIm-Tf IL is also shown as reference.

In spite of its higher IL uptake, IPMC actuator made from this [$EtIm^+$] modified Nexar pentablock copolymer had a slower bending response and comparable bending curvature as compared to the one made from Nafion. However, it is still a promising candidate for the IPMC actuator application further development.

3.4.2 IPMC actuator made from imidazolium-containing triblock copolymer membranes

By applying nitroxide-mediated polymerization (NMP), another novel imidazolium-containing ABA triblock copolymer poly(Styrene-*b*-[1-ethyl-3-(4-vinylbenzyl)imidazolium bis(trifuoromethane sulfonyl)imide])-*b*-Styrene), or poly(Sty-*b*-[EVBIm][Tf_2N]-*b*-Sty), was

synthesized and cast into an *i*EAP membrane and characterized by Green *et al*. for IPMC actuator fabrication (Figure 3.29).[14] The charged, low T_g imidazolium central block imparts electrochemical stability and high ion conductivity, while polystyrene outer blocks offer mechanically reinforcing phases for suitable mechanical properties. DMA analysis revealed a modulus of approximately 100 MPa for this triblock copolymer at room temperature, which is suitable for fabrication into an IPMC actuator. Microscopic phase separation was confirmed by using small angle X-ray scattering (SAXS) and transmission electron microscopy (TEM). The ionic conductivity of this triblock copolymer determined by electrochemical impedance spectroscopy was found to be ~5.0×10^{-7} S/cm.

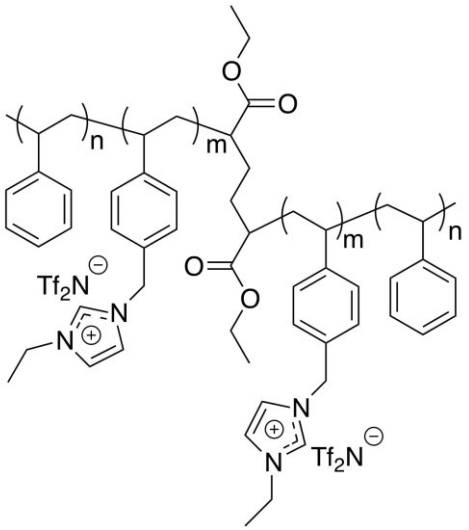

Figure 3.29. Structure of poly(Sty-*b*-[EVBIm][Tf_2N]-*b*-Sty) triblock copolymer.

Using the poly(Sty-*b*-[EVBIm][Tf_2N]-*b*-Sty) membrane with a thickness around 50 μm provided by Green, IPMC actuators with 30 BL CNC were fabricated and tested. EMIm-Tf IL was not incorporated because we found that the membrane instantly deformed and degraded into a sticky amorphous state once it contacted with IL. The reason for this degradation still needs further investigation. An actuator made from Nafion with 30 BL CNC and no IL was also

prepared for performance comparison. The bending behavior of those two devices is shown in Figure 3.30.

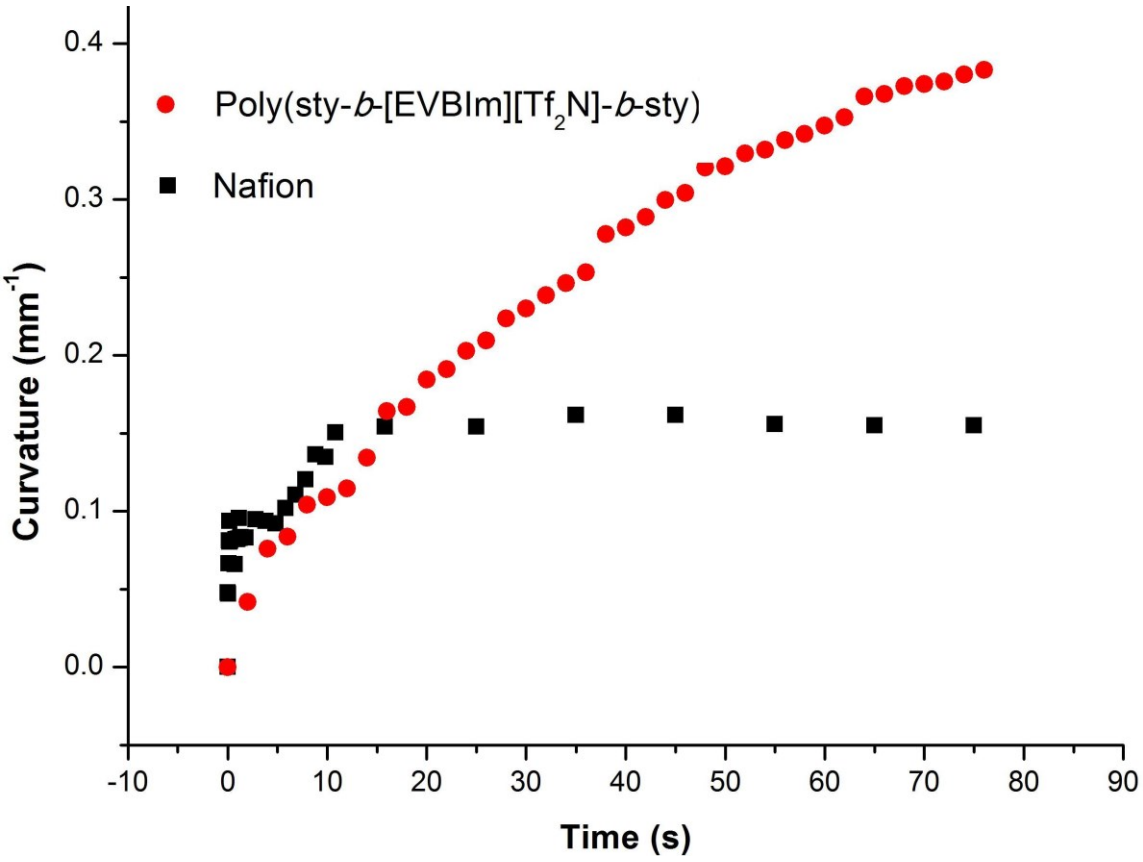

Figure 3.30. Bending curvature as a function of time of the IPMC actuator made from poly(Sty-*b*-[EVBIm][Tf_2N]-*b*-Sty) membrane with 30 BL CNC and no IL under a 4 V DC input. The bending of a Nafion actuator with 30 BL CNC and no IL is shown for comparison.

When there was no IL incorporated, the bending was generated by the transport and accumulation of [Tf_2N^-] anions associated to the poly(Sty-*b*-[EVBIm][Tf_2N]-*b*-Sty) actuator. To the contrary, free hydroniums primarily contributed to the bending of Nafion actuator. The bending performances of those two types of IPMC actuator were comparable in the first 20 s after the DC input was applied. Then, the bending of Nafion actuator deceased while the one of poly(Sty-*b*-[EVBIm][Tf_2N]-*b*-Sty) actuator kept increasing and reached about 2.5 times bigger

compared to the Nafion actuator. Although preliminary, this result clearly shows some superior properties of the poly(Sty-*b*-[EVBIm][Tf_2N]-*b*-Sty) over Nafion in actuator applications. Please note that as opposite to the anodic bending of the Nafion actuator, this poly(Sty-*b*-[EVBIm][Tf_2N]-*b*-Sty) actuator generates cathodic bending only (due to [Tf_2N^-]), which was assigned to have positive curvature for easy comparison with Nafion case in Figure 3.30. As a matter of fact, it is noteworthy that this was the first time to apply a cationic triblock copolymer with anionic counterion for actuator application.

As a following work, Jangu *et al.*[15] synthesized a series of well-defined ABA triblock copolymers with polystyrene external blocks but a charged poly(1-methyl-3-(4-vinylbenzyl)imidazolium bis(trifuoromethane sulfonyl)imide central block by using the same NMP approach (structure shown in Figure 3.31). Microphase separation and good mechanical stability were confirmed using SAXS and DMA, respectively, which are suitable for IPMC actuator applications.

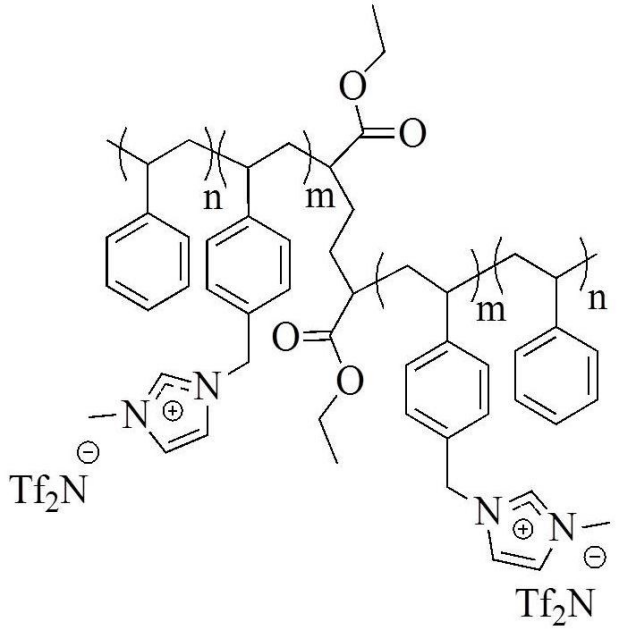

Figure 3.31. Structure of poly[Sty_n-*b*-(MVBIm-Tf_2N)$_m$-*b*-Sty_n] ABA triblock copolymer.

Several of these triblock copolymers membranes with different segment numbers were cast with EMIm-Tf IL and fabricated into IPMC actuators and tested. Of these, (poly[Sty_{35}-*b*-$(MVBIm\text{-}Tf_2N)_{80}$-*b*-$Sty_{35}$] —showed the best bending performance. This membrane was cast with 32 wt. % IL with 180 μm thickness and coated with 30 BL CNC. The bending performance at 4 V DC input is shown in Figure 3.32, along with the bending curvature of a 30 BL Nafion with 35 wt.% IL also shown as reference. Similar actuation speed but smaller actuation amplitude were obtained from this triblock copolymer, as compared with the one made from Nafion, which was probably due to its much smaller ion conductivity than that of Nafion.

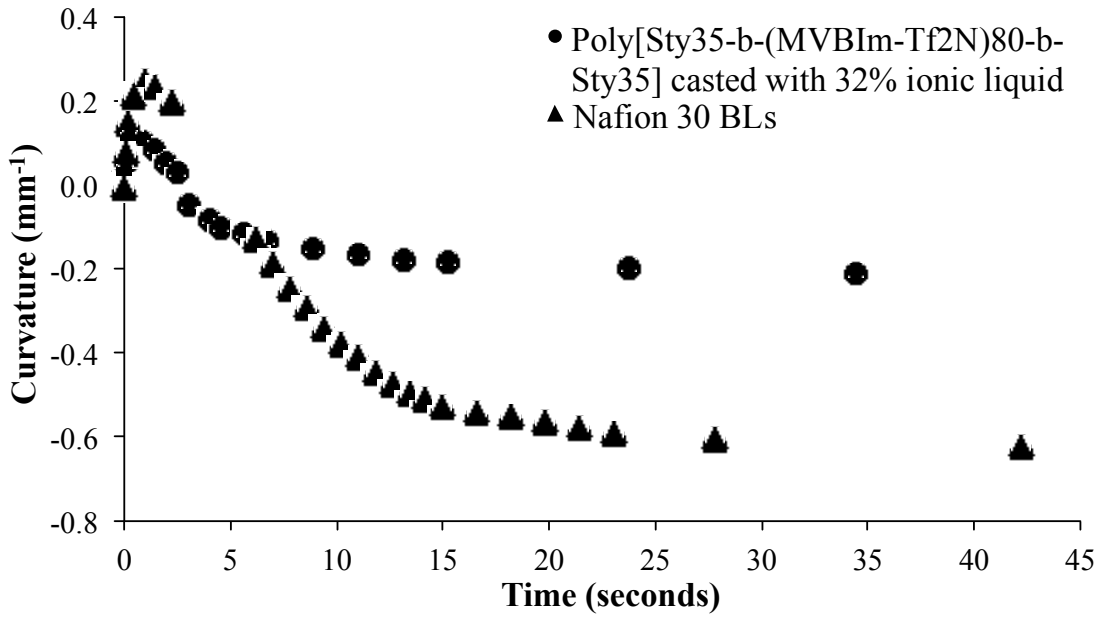

Figure 3.32. Bending curvature observed under a 4 V applied voltage for IPMC actuators made from poly(Sty_{35}-*b*-$(MVBIm\text{-}Tf_2N)_{80}$-*b*-$Sty_{35}$) triblock copolymer casted with 32 wt.% of EMIm-Tf IL, and Nafion membrane swollen with 35 wt.% EMIm-Tf IL as reference.

3.4.3 IPMC actuator made from DMAEA-containing ABA Triblock copolymer membrane

Besides the imidazolium-containing family, the high-molecular-weight poly(Sty-*b*-(*n*BA-*co*-SBDMAEA)-*b*-Sty) triblock copolymer (structure shown in Figure 3.33) was successfully synthesized and characterized by Wu *et al.*[16] as the *i*EAP by employing reversible addition-fragmentation chain transfer (RAFT) polymerization. The presence of the tertiary amine functionality in the central block of this triblock copolymer afforded tunable polarity toward polar guest molecules, such as IL. This results in a good affinity toward EMIm-Tf IL, which is desirable for better actuation performance. In addition, a ~100 MP modulus was found that is suitable for actuator fabrication.

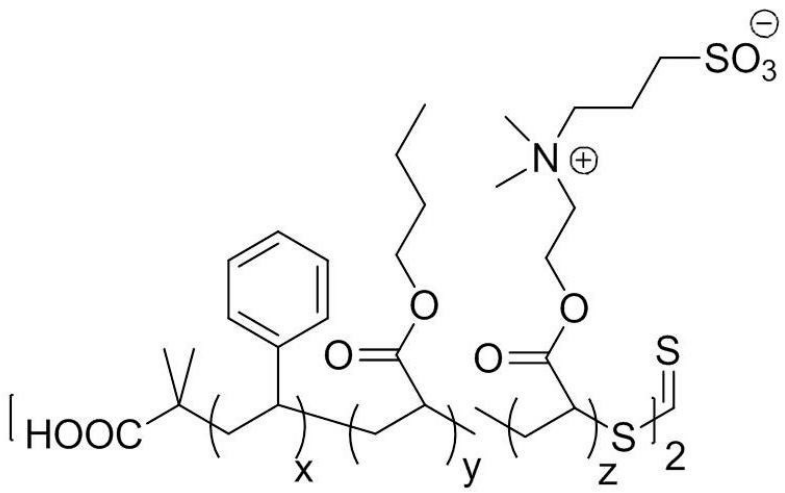

Figure 3.33. Structure of poly(Sty-*b*-(nBA-*co*-SBDMAEA)-*b*-Sty) triblock copolymer.

A cast membrane of this triblock copolymer with ~30 μm thickness was used to perform the LbL CNC coating to 30 BL. By soaking the membrane at 60 °C for 28 h, up to 58 wt.% EMIm-Tf IL is incorporated (as compared to < 30 wt.% uptake for Nafion IPMC actuator under same conditions). After being hot pressed with gold foil as outer electrode, an actuator made from this BDMAEA triblock copolymer membrane was tested in 70% humidity and clearly

experiences bidirectional bending behavior, as shown in Figure 3.34. This specific actuator did not show clear actuation in lower humidity. The bending performance of the actuator made from Nafion membrane with 30 BL CNC and 35 wt.% IL is included as reference.

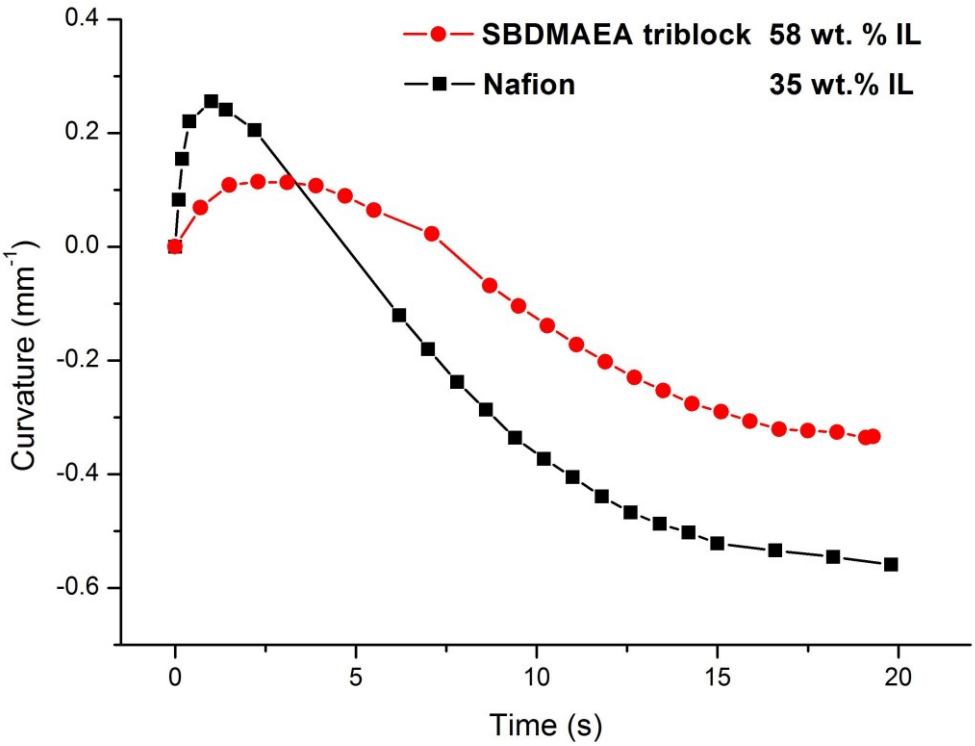

Figure 3.34. Actuation curvature for electromechanical transducer fabricated from the SBDMAEA triblock copolymer with 58 wt% EMIm-Tf IL under 4 V DC input and in 70% humidity. The bending of a Nafion actuator with 30 BL CNC and 35 wt.% IL is shown for comparison.

The bending performance of the SBDMAEA actuator with 30 BL CNC was not as good as the one of Nafion actuator with same CNC, especially when considering it contained more IL and was operated in a higher humidity.

3.4.4 IPMC actuator made from imidazolium-containing triblock copolymers containing a synergy of ether and imidazolium sites

In a recent work, Jangu *et al*. also applied the RAFT polymerization to synthesize a well-defined A-BC-A poly[Sty-*b*-(MVBIm-Tf_2N_{52}-*co*-$DEGMEMA_{48}$)-*b*-Sty] triblock copolymer. It contains a soft "BC" central block of DEGMEMA and imidazolium sites with external polystyrene blocks that provide mechanical reinforcement, as shown in Figure 3.35. This triblock copolymer was found to have suitable morphology and thermomechanical properties to be cast into films with ionic liquid and then fabricated into IPMC actuators.

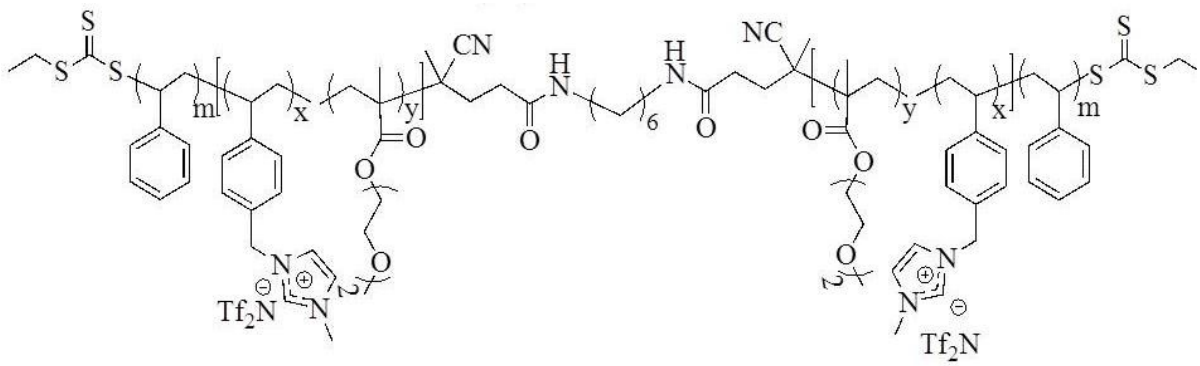

Figure 3.35. Structure of poly[Sty-*b*-(MVBIm-Tf_2N-*co*-DEGMEMA)-*b*-Sty] charged A-BC-A triblock copolymer.

This A-BC-A copolymer was cast by Jangu into a membrane with a thickness ~ 50 µm. Then, 30 BL CNC were coated on both sides of the membrane followed by soaking with EMIm-Tf IL at 90 °C for 30 min to a weight uptake of 29.9%.

At ambient conditions, the actuator prepared from this triblock copolymer membrane showed bidirectional bending under a 4 V DC input. Compared to a the bending performance of a Nafion actuator with same 30 BL CNC and 35 wt.% IL uptake, the actuator prepared from this triblock copolymer membrane showed greater curvature and faster response in the anodic

bending (Figure 3.36). This implies that this triblock copolymer membrane provided a more efficient transport channel for electrolytes than Nafion, and thus resulted in a faster and larger accumulation of the cations in the cathode side CNC. Moreover, considering that the following cathodic bending was caused by the suppression of the larger initial cation accumulation (as compared to the Nafion case) by the slower anionic counterpart accumulation on the anode side CNC, the transport of anions was also largely enhanced compared to the Nafion membrane. The fact that this triblock copolymer IPMC actuator contained less ions (29.9 wt.% uptake of IL, as compared to 35 wt.% of Nafion IPMC actuator) makes this triblock copolymer membrane a promising candidate for replacing Nafion in electroactive device applications.

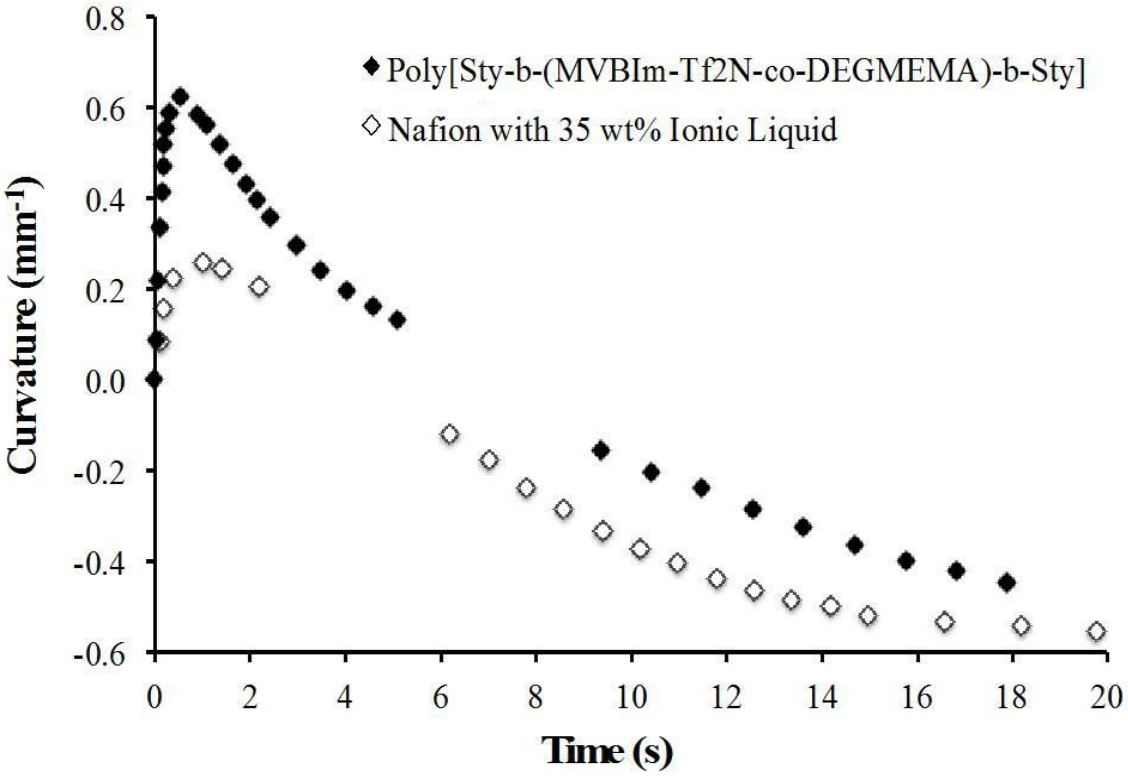

Figure 3.36. Bending curvature of IPMC actuator made from poly[Sty-*b*-(MVBIm-Tf_2N-*co*-DEGMEMA)-*b*-Sty] having 26 mol% ion content at ambient conditions (20 °C and ~ 43% humidity) under a 4 V applied voltage. The membrane was soaked with 29.9 wt.% EMIm-Tf IL, with Nafion membrane with 35 wt.% ionic liquid as reference.

3.5 Supplement note about the "conditioning" effect

It should be pointed out that a unique "conditioning" effect was discovered by us from IPMC actuator related studies. This corresponds to a distinct improvement in bending performance of an actuator after several cycles of operation under alternating power polarity. Specifically, for a freshly prepared actuator under a 4 V step DC input, when the anodic bending was complete and the actuator was bending toward the cathode, the polarity of the power source was instantly reversed to make the actuator start bending toward anode again. Another instant reverse of power polarity was applied when the actuator passed the neutral position and became closer to anode. A faster response to such polarity reversal was usually seen as compared to the first operation. This procedure was repeated several times until the response speed of the actuator to the reversal operation did not increase any further. The bending performance of the IPMC actuator conditioned this way was greatly improved, especially for the faster anodic bending. Interestingly, this effect was not observed in the actuators without CNC layers.

To demonstrate this effect, four Nafion actuators with 35 wt.% EMIm-Tf IL and 10, 20, 30 and 40 BL of GNP CNC were tested freshly first, and then after being subjected to the conditioning process. The results are summarized in Figure 3.37, where only the anodic bending was tested and recorded.

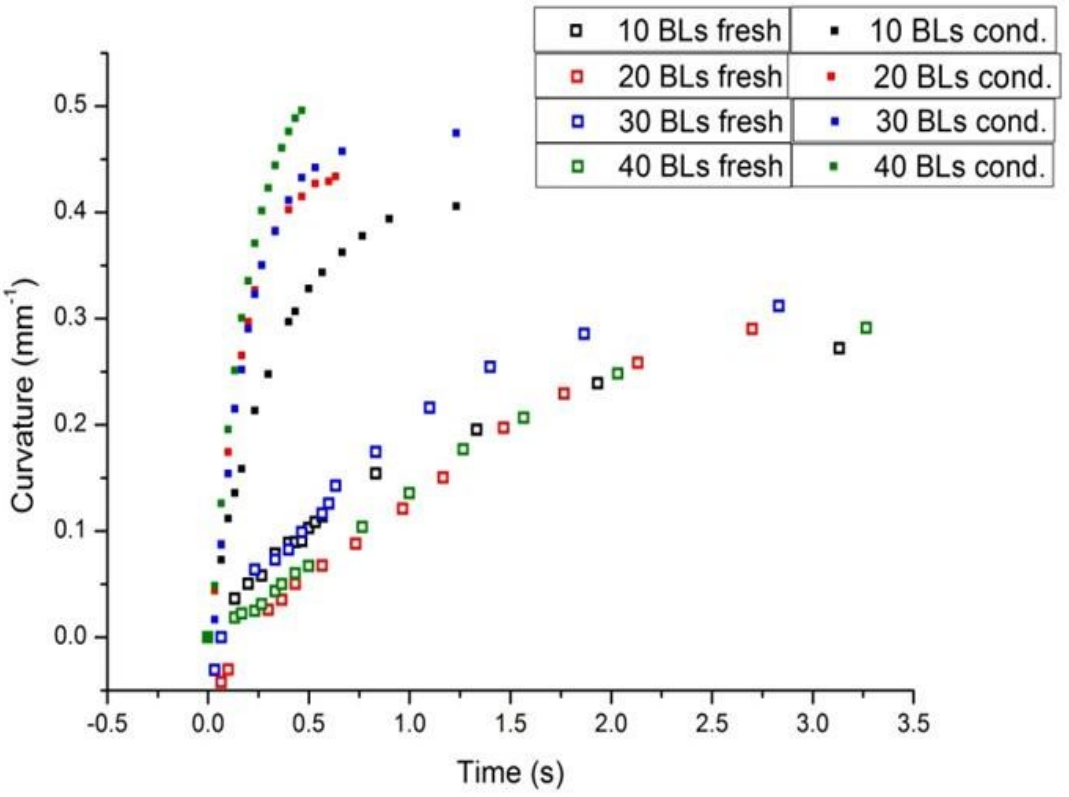

Figure 3.37. Fast anodic bending performance of Nafion actuators with different CNC thickness but same 35 wt.% IL uptake before and after "conditioning".

The improvement in the bending performance can be clearly seen from Figure 3.37. Both the speed and amplitude of anodic bending were greatly enhanced for all the actuators tested. Especially, actuators with thicker CNC experienced more improvement compared to the ones with thinner CNC. As a result, the bending curvature did not show clear dependence on the CNC thickness for the freshly prepared actuator, but larger bending amplitude was shown in the actuators with thicker CNC after they had been through the conditioning process.

Although the mechanism of this conditioning effect is still not clear, it clearly relates to the existence and properties of CNC layer. A possible reason could be that the back and forth ion accumulation and depletion help to open more porous space in the CNC to be able to

accommodate more ions. It could also be the result of some kind of electrochemical process in the GNP-polymer interface that changed the ionic environment in the CNC. In addition, this conditioning seems to be a permanent change to the actuator. After being stored for an extended time, the performance of a conditioned IPMC actuator was still better than when it was freshly made.

To help generate better bending performance of the actuator, the conditioning process is also crucial for good consistency in actuation tests. Thus, actuators (including the ones without CNC coating) used for the testing and discussion reported in this dissertation were all conditioned before being tested.

References

1 M. D. Bennett and D. J. Leo, *Sensors and Actuators a-Physical* **115,** 79 (2004).

2 Y. Liu, S. Liu, J. Lin, D. Wang, V. Jain, R. Montazami, J. R. Heflin, J. Li, L. Madsen, and Q. M. Zhang, *Applied Physics Letters* **96** (2010).

3 D. Wang, R. Montazami, and J. R. Heflin, *MRS Online Proceedings Library* **1575,** null (2013).

4 S. Nemat-Nasser, *Journal of Applied Physics* **92,** 2899 (2002).

5 Y. Bar-Cohen, *Electroactive polymer (EAP) actuators as artificial muscles : reality, potential, and challenges* (SPIE Press, Bellingham, Wash., 2004).

6 R. Montazami, S. Liu, Y. Liu, D. Wang, Q. M. Zhang, and J. R. Heflin, *Journal of Applied Physics* **109** (2011).

7 A. V. Anantaraman and C. L. Gardner, *Journal of Electroanalytical Chemistry* **414,** 115 (1996).

8 M. Eikerling, A. A. Kornyshev, and U. Stimming, *The Journal of Physical Chemistry B* **101,** 10807 (1997).

9 F. Opekar and D. Svozil, *Journal of Electroanalytical Chemistry* **385,** 269 (1995).

10 S. Imaizumi, Y. Kato, H. Kokubo, and M. Watanabe, *Journal of Physical Chemistry B* **116,** 5080 (2012).

11 J. Li, K. G. Wilmsmeyer, J. Hou, and L. A. Madsen, *Soft Matter* **5,** 2596 (2009).

12 J. Hou, Z. Zhang, and L. A. Madsen, *Journal of Physical Chemistry B* **115,** 4576 (2011).

13 R. Gao, D. Wang, J. R. Heflin, and T. E. Long, *Journal of Materials Chemistry* **22,** 13473 (2012).

14 M. D. Green, D. Wang, S. T. Hemp, J.-H. Choi, K. I. Winey, J. R. Heflin, and T. E. Long, *Polymer* **53,** 3677 (2012).

15 C. Jangu, J.-H. H. Wang, D. Wang, S. Sharick, J. R. Heflin, K. I. Winey, R. H. Colby, and T. E. Long, *Macromolecular Chemistry and Physics* **215,** 1319 (2014).

16 T. Wu, D. Wang, M. Zhang, J. R. Heflin, R. B. Moore, and T. E. Long, *Acs Applied Materials & Interfaces* **4,** 6552 (2012).

CHAPTER 4 ISAM THIN FILM NANOSTURCTURES IN MEMS GC DEVICES

The work in this chapter was performed in a NSF-funded collaboration with the VT MEMS LAB of Prof. Agah in the Department of Electrical and Computer Engineering at Virginia Tech. Unless otherwise noted, the GC performance testings of all the μTPCs and μSCs reported in this dissertation were conducted by Muhammad Akbar and Hamza Hankeel, respectively, of VT MEMS LAB. The geometric design of all the μGC devices was done by VT MEMS LAB.

4.1 Thin film ISAM SNP coating in GC micro-thermal preconcentrators (μTPCs)

4.1.1 The fabrication and characterization of μTPCs

The fabrication of the μTPCs in this work started with the photolithography of microposts and fluidic ports using AZ9260 photoresist on standard single side polished silicon wafers (4 inch, 500 μm thick, University Wafers). The wafers were first spin coated with AZ9260 photoresist at 3000 rpm to achieve around 8 μm thickness, soft-baked at 110 °C for 1 minute, and exposed for 45 seconds through custom masks described below using a mask aligner (Karl Suss MA-6). After development using AZ400K, wafers were hard-baked at 110 °C for 2 minutes. Deep reactive ion etching (DRIE, Alcatel) with photoresist as the etch mask was then used to etch the wafers in order to achieve an etching depth of 240 μm. Afterwards, the wafers were diced into individual devices which were ready for the incorporation of adsorbent materials. The thus fabricated μTPC device consisted of 12 mm × 9 mm × 0.5 mm silicon chip with 80 × 80 array of square pillars that having 50 μm side length, embedded inside an 8 mm × 8 mm × 0.24 mm cavity.

4.1.2 Adsorbents for the µTPCs—thin film Tenax TA

After stripping the photoresist with acetone, the etched device was filled with Tenax TA polymer solution (10 mg/ml in dichloromethane) and allowed to evaporate to leave a thin film of the polymer adsorbent on the cavity surfaces. The device was then sealed with a Pyrex 7740 wafer (500 µm thick, University Wafers) using anodic bonding with temperature, pressure, and voltage set to 320 °C, 22 kPa, and 1250 V, respectively. Finally, fused silica capillary tubes (220 µm O.D. and 100 µm I.D., Polymicro Technologies) were inserted and sealed inside the fluidic channels with epoxy to serve as inlet/outlets for the device, as shown in Figure 4.1 (blue "T" process).

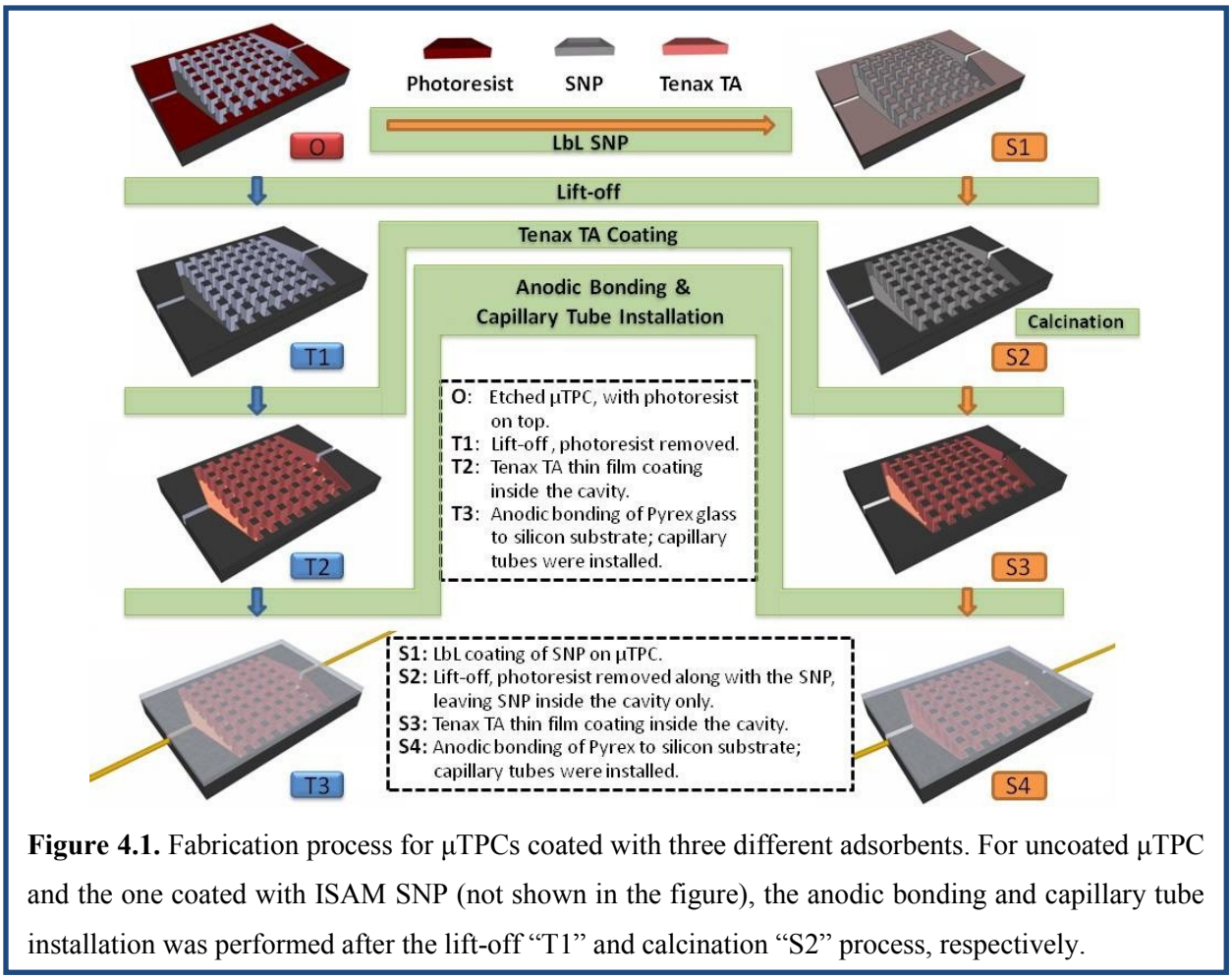

Figure 4.1. Fabrication process for µTPCs coated with three different adsorbents. For uncoated µTPC and the one coated with ISAM SNP (not shown in the figure), the anodic bonding and capillary tube installation was performed after the lift-off "T1" and calcination "S2" process, respectively.

4.1.3 Adsorbents for the μTPCs—thin film ISAM SNP

Following silicon etching while having photoresist left over the un-etched regions, the LbL technique was used to coat the interior surfaces of the μTPCs with ISAM SNP as shown in Figure 4.2. The positively-charged long-chain PAH acts like a polymeric "glue" to hold the negatively-charged SNP "bricks" together. Following the earlier work in our group using SNP for antireflection coatings,[1] the pH of the 10 mM PAH (Sigma-Aldrich) solution and SNP colloid (45 nm average diameter, 20-21 wt.% in water, NISSAN Chemical) were adjusted to 7.0 (±0.1) and 9.0 (±0.1), respectively, by adding HCl and NaOH solutions, in order to achieve maximum surface charge differences for enhancing the electrostatic bonding between the adjacent layers while maintaining colloidal stability.

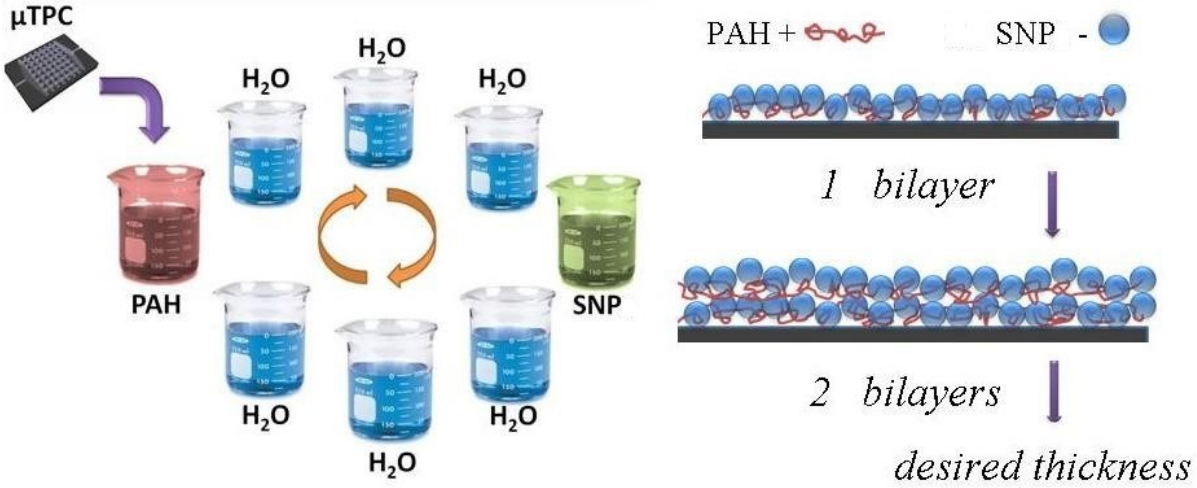

Figure 4.2. Schematic procedure of layer-by-layer assembly of ISAM SNP coating on μTPC.

An automatic dipping system (Figure 2.2) was used to perform the LbL deposition process. Eight beakers were placed in a circle, with one containing PAH solution and another containing SNP colloid. Three beakers were placed between them on each side that could automatically be emptied and refilled with deionized (DI) water for rinsing purposes. The μTPC chips, held on

glass slides, were first dipped into the PAH solution for 2.5 minutes, followed by three consecutive one-minute rinsings in DI water. They were then dipped into the SNP colloid for another 2.5 minutes followed by another three rinsing steps before the chips went back into the PAH solution. The resulting coating covered the entire surface of the μTPCs, including the internal etched 3D structures and the photoresist left on the top of the chip from the chip fabrication process.

A lift-off procedure via sonication in acetone for 5 minutes was then used to remove the photoresist along with the SNP coating on top of the unetched areas, leaving SNP only on the sidewalls and bottom of the etched features. This process guaranteed a smooth clean top surface which was crucial for anodic bonding with the Pyrex wafer while in the meantime keeping the SNP coating elsewhere intact. Prior to anodic bonding, the chips were placed in an oven at 500 ºC for 4 hours. This calcination step burns off the PAH and softens and slightly fuses the SNPs together, resulting in a thermally and mechanically robust SNP coating as the only adsorbent material for the μTPCs. The device was then sealed with a Pyrex wafer using the same anodic bonding and capillary tubes installation procedure described in section 4.1.2, as shown in Figure 4.1 (blue "T" process).

4.1.4 Adsorbents for the μTPCs—ISAM SNP modified Tenax TA

After the calcination step, some of the SNP-coated μTPCs were further coated with Tenax TA using the same method described in Section 4.1.2. The devices were then sealed by anodic bonding and inlets/outlets installed as described in section 4.1.2. The process is shown in Figure 4.1 (orange "S" process). This yielded a Tenax TA layer that possessed a nanostructure surface that resembled the SNP surface.

4.1.5 Surface characterization of the μTPCs

FESEM images of the μTPCs with the three different adsorbents (SNP, thin film Tenax TA and SNP-Tenax TA) are shown in Figure 4.3 and Figure 4.4. Figure 4.3 A-C shows the FESEM images of the μTPC with only SNP as the adsorbent. Figure 4.3 A shows the top view of the μTPC after the lift-off procedure. A clean top surface was achieved which was beneficial for the anodic bonding process. Meanwhile, the bottom (Figure 4.3 B) and the sidewall of the microposts (Figure 4.3 C) were covered with a homogeneous, porous SNP coating (insets of Figure 4.3 B, 4.3 C).

An FESEM image of the surface profile of the thin film Tenax TA coating in the μTPC is shown in Figure 4.3 D. The thin film Tenax TA coating on the sidewalls of the microposts experienced low density pores (inset a). From the cross-sectional view of the thin film Tenax TA coating on the bottom, it can be seen that the coating had a micro-fiber like structure underneath a dense, relatively smooth surface. Thus, the total available surface area was somewhat limited.

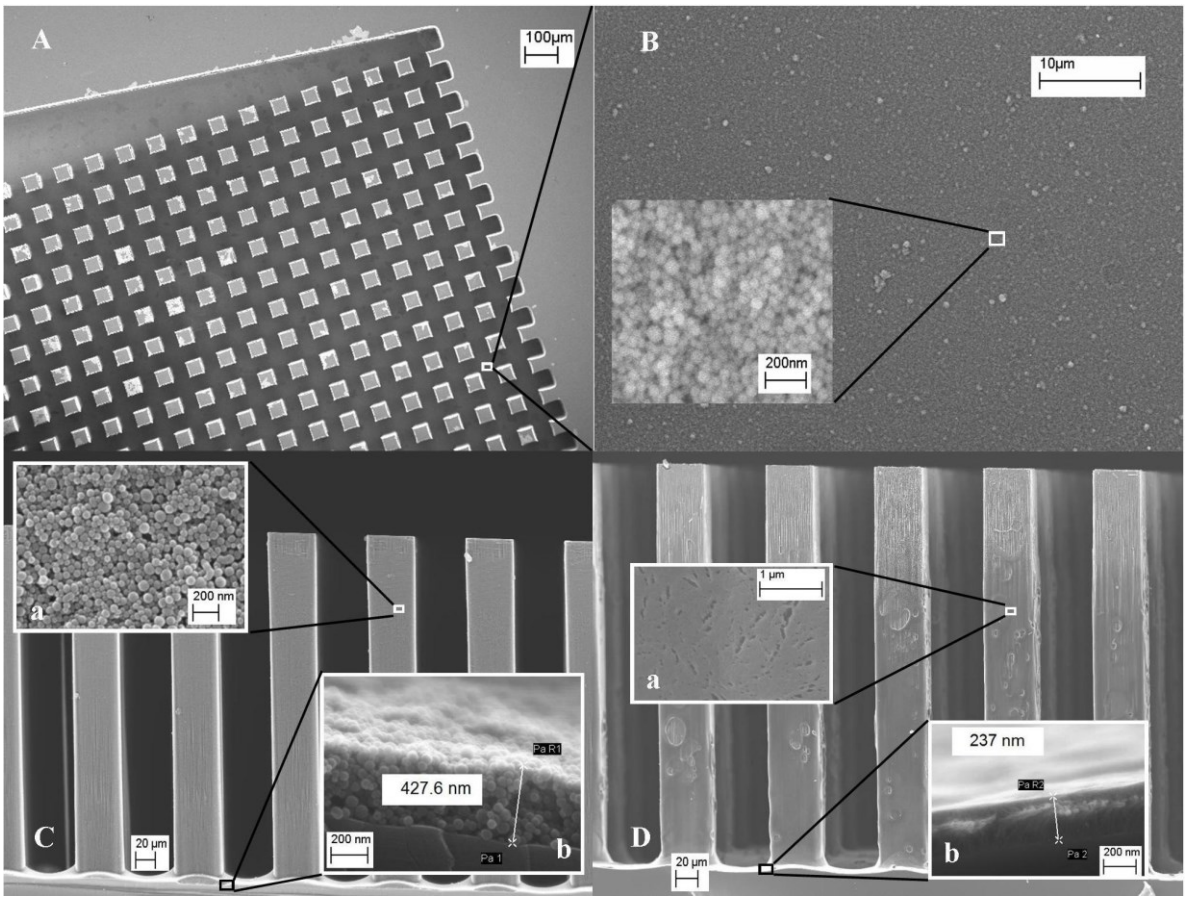

Figure 4.3. SEM images of (A) the µTPC coated with 10 BL ISAM SNP, (B) top view of the SNP coating on the bottom of the µTPC, and (C) cross-section view of SNP coating on the sidewall of the micro posts. Inset C(a) shows the high magnification view and inset C(b) shows the thickness of SNP coating on the bottom. (D) cross-section view of Tenax TA thin film on micro posts. Inset D(a) is a closer view of Tenax TA coating on the sidewall of the pillars. Inset D(b) shows the thickness of the Tenax TA coating on the bottom of the µTPC.

In comparison, the morphology of the Tenax TA coating inside the µTPC was significantly modified by the underlying SNP coating. The FESEM images illustrating this change are shown in Figure 4.4. A nanoscaled structure of Tenax TA was developed on the SNP coating present on the sidewall of the microposts. With the help of the SNP coating underneath, the nano "drips" and "strips" of Tenax TA fine structure were developed in three dimensions, which significantly increased the surface area of Tenax TA. A different surface morphology of Tenax TA on SNP

was achieved on the bottom of the μTPC, where Tenax TA was conformally coated on the rough surface of the SNP, as shown in Figure 4.4 B. This may have been caused by the different amount of Tenax TA attached to the sidewall of the microposts and the bottom, due to gravitational effects during the Tenax TA deposition and solvent evaporation. This conformal coating also increased the surface area of the Tenax TA by inheriting the large surface area and porosity from the SNP coating.

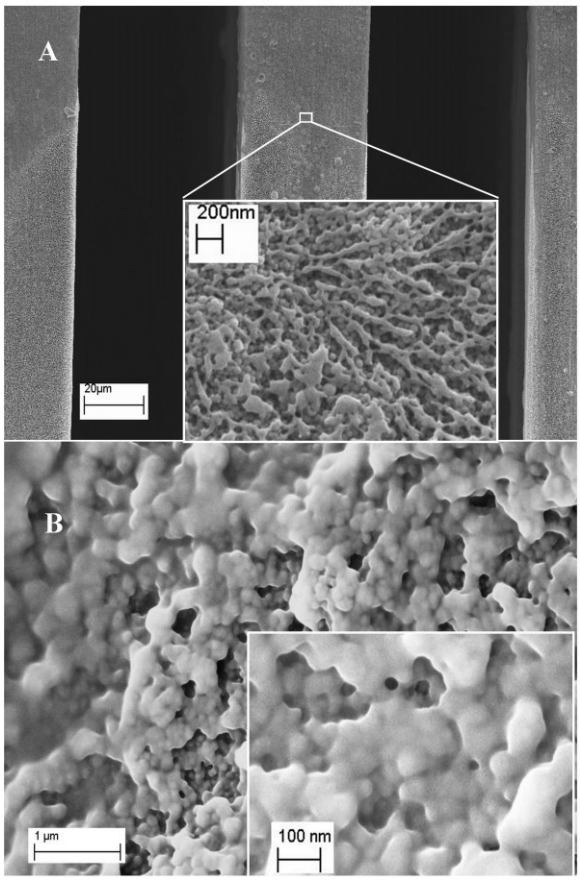

Figure 4.4. (A) cross-section view of Tenax TA-coated SNP on the sidewall of the micro posts. The inset shows the nanoscale structure of Tenax TA brought by the SNP coating underneath (B) Tenax TA conformally deposited on the SNP template on the bottom.

The three dimensional surface profiles of the bare silicon wafer and the 10 BL ISAM SNP coating on a silicon wafer were compared using an Atomic Force Microscope (AFM) in Figure

4.5. It is quite clear that the roughness, and thus the surface area, was substantially increased by the SNP coating. The measured roughnesses for a 1 µm × 1 µm area of these two surfaces were around 0.4 nm and 13 nm, respectively, which indicates that the surface roughness was increased by a factor of 30. In the case of the Tenax TA coating, the large scale structures limited the use of AFM for measuring the surface roughness. Since the AFM could not probe the real chip due to the fabricated microstructures, the surface measurements were all performed on a planar surface prepared using the same deposition procedure.

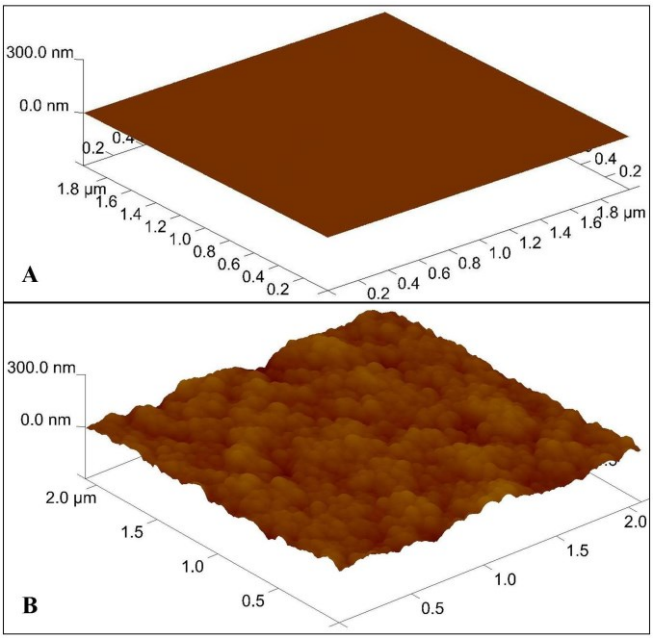

Figure 4.5. 3-D AFM image of the surface of (A) silicon wafer surface and (B) 10 BL SNP coating on the silicon surface. The analysis was performed on a 1 µm × 1 µm chip area.

4.1.6 Adsorption capacities

All the various chip configurations (SNP, Tenax TA thin film, and SNP-Tenax TA) were tested under the same flow conditions (typically 1 ml/min). The sample volumes and injection split ratios were varied to determine the adsorption capacity over a range of polarities using

hexane, toluene, 1,2-dichloroethane, and isopropanol as test compounds. Flasks were prepared with septum caps containing each compound and the headspace allowed to become saturated with vapor. Assuming ideal gas law behavior, the mass amount of analyte injected from a saturated vapor above the pure liquid was calculated from the injection volume and the split ratio used for the injection. For example, a 1 μL injection of hexane vapor at 1 atm and 25 °C with a 50:1 split injection (2% reaching the μTPC) would be 70 ng. Samples were drawn from the headspace using gas-tight syringes and injected immediately into the heated GC injection port. The GC oven was maintained under isothermal conditions at 30 °C. Helium was used as the carrier gas supplied via the GC split/splitless inlet and controlled by the electronic flow controller. The chips were connected directly between the injection port and the flame ionization detector (FID) maintained at 250 °C. The μTPC was mounted on a high performance ceramic heater which was rapidly heated to 250 °C at a ramp rate of ~100 °C/s. A K-type thermocouple coupled to a digital voltmeter was used for manual temperature monitoring and control. After the sample vapor injection, the breakthrough signal (analyte not retained by the preconcentrator) was allowed to return to a baseline level prior to heating for analyte desorption. The ratio of the retained area to total area (unretained plus retained) relative to the total mass injected provides the mass adsorption capacity.

The mass retention of the chips was determined from the fraction of the total area retained relative to the total area (breakthrough peak plus retained peak). In this study, the capacity of the devices was initially characterized with μL volumes of analyte sampled from a saturated headspace using gas-tight syringes. An example of a typical retention profile for toluene using a SNP-Tenax TA chip is shown in Figure 4.6 for three replicate runs. Tailing from the excess hexane in the breakthrough peak is expected due to the porous nature of the SNP layers coupled

with weak intermolecular adsorption of multiple analyte layers from oversaturation of the chip; however, the thermal desorption of the trapped hexane at around 250 °C is very sharp (w_b < 6-8 seconds; where w_b represents width of the peak at the base) as well as reproducible over multiple firings. This is a very desirable attribute and necessary for efficient transfer of analytes as a narrow band to a chromatographic column for separations.

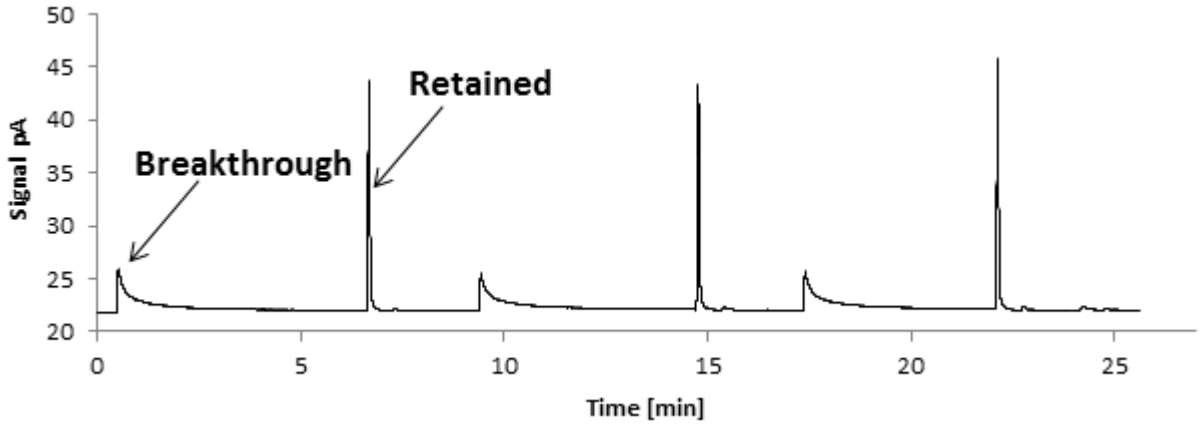

Figure 4.6. Triplicate desorption profiles for hexane from an SNP-Tenax TA μTPC.

Comparisons of the adsorption capacities for the three types of μTPC chips used were performed by the research group of Prof. Rice of the Department of Chemistry at The College of William & Mary. The results are graphically depicted in Figure 4.7. All the chips were tested under identical conditions with respect to adsorption temperature (30 °C), flow rate (1 ml/min), and desorption temperature (~250 °C). The adsorption capacity of the SNP-Tenax TA relative to the Tenax TA chip improved by factors of 2.7, 1.3, 1.4, and 3.0 for hexane, toluene, 1,2-dichloroethane, and isopropanol respectively, which represents a range of polarities. The enhanced surface area and morphology of Tenax TA most likely resulted in these enhancements for low to medium polarity compounds.

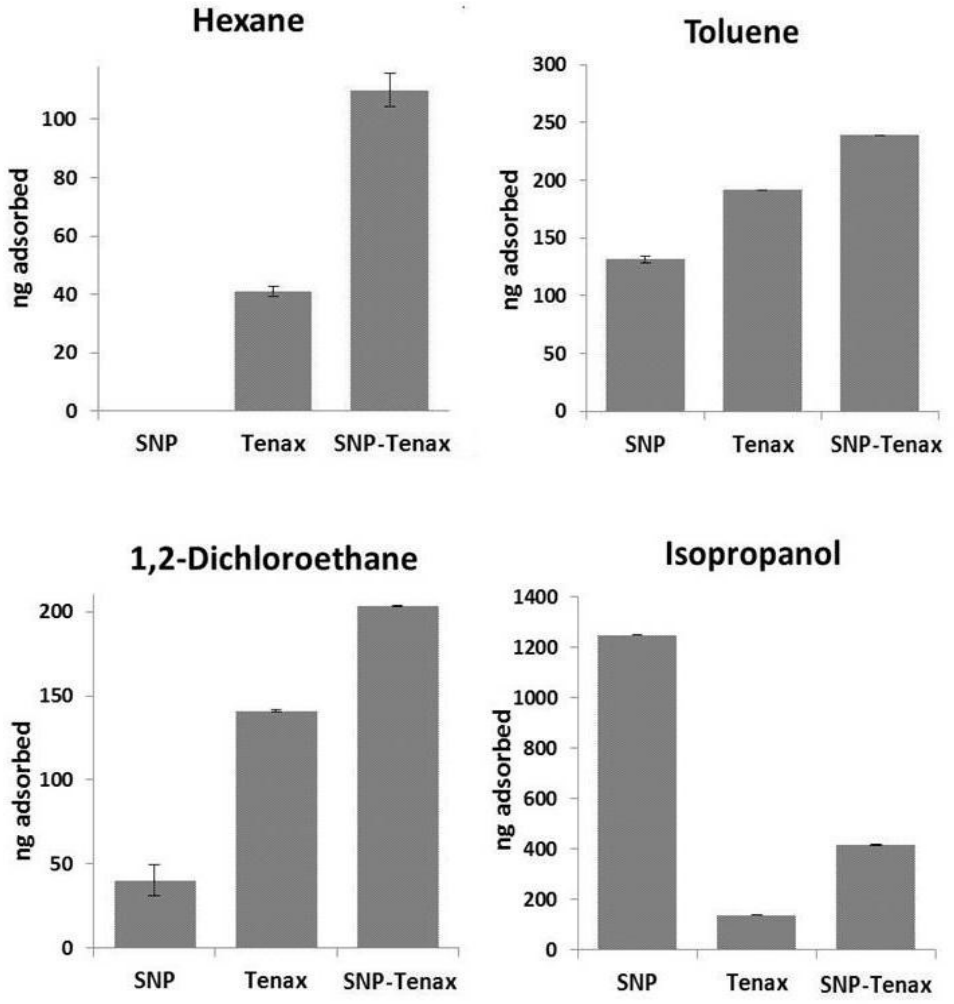

Figure 4.7. Adsorption capacities of SNP, Tenax TA, and SNP-Tenax TA μTPCs for hexane, toluene, 1,2-dichloroethane, and isopropanol.

The most striking impact from polarity was observed for the SNP chip. Virtually no hexane (a very non-polar compound) was retained by the SNP chips; however, substantially more isopropanol was retained than for either the Tenax TA and SNP-Tenax TA chips (by factors of 9.0 and 3.0 respectively). This is due to the large number of active hydroxyl sites present on the silica surface that have very strong intermolecular attractions via hydrogen bonding to very polar compounds such as alcohols. The reduced capacity for isopropanol in the presence of Tenax TA is most likely the result of a significant number of these sites being covered by the Tenax TA

film. This type of interaction could be advantageous for producing pseudo-selective chips for retention of polar compounds. However, additional studies must be performed to ascertain whether irreversible adsorption could occur with more active polar compounds such as phenols or amines.

The capturing ability of the SNP-Tenax TA chip coupled with a chromatographic separation was successfully demonstrated by testing a mixture of eight commonly found VOCs. The liquid volumes of the VOCs used to produce the mixture were based on the relative vapor pressures of each VOC such that the vapor state mix contained comparable mole amounts of each VOC, assuming ideal gas law conditions. The mixture was contained within a septum-sealed bottle. During the adsorption phase, the chip was loaded with a 10 µl headspace volume of the mixture using a gas-tight syringe. The pressure was maintained at 5 psi (0.5 ml/min flow rate) to allow sufficient interaction between the analytes and the adsorbent. Before the thermal desorption, the pressure was increased to 20 psi (1.5 ml/min flow rate) and the signal was allowed to return to original level. The increased pressure was necessary to produce an adequate flow rate in the 30-m long GC column. In addition, this assisted in producing a narrower plug during the thermal desorption process for subsequent separation by increasing the volumetric flow rate. The GC column was then coupled to the µTPC and the chip was quickly heated to 250 °C to desorb the compounds. The chromatogram in Figure 4.8 is the result of coupling the µTPC to the GC column. It is evident from the chromatogram that the last several peaks widths (compounds 4-8) are significantly narrower than the preceding ones (compounds 1-3). This is due to the condensation of less volatile compounds onto the beginning of the cold GC column after thermal desorption, resulting in a narrower sample plug. On the other hand, the more volatile compounds may tend to remain in the vapor phase and continue through the column,

resulting in a broader peak based on the desorption characteristics of the μTPC. The results shown in the top inset of Figure 4.8 indicate that the chip successfully captured/concentrated all of the injected analytes from the mixture with a desorption peak width of ~10 seconds and a negligible breakthrough peak, which is expected since the volume injected and split ratio used are comparable to the conditions used for testing the adsorption capacities of the individual compounds previously described. Chromatograms obtained from multiple injections are highly reproducible.

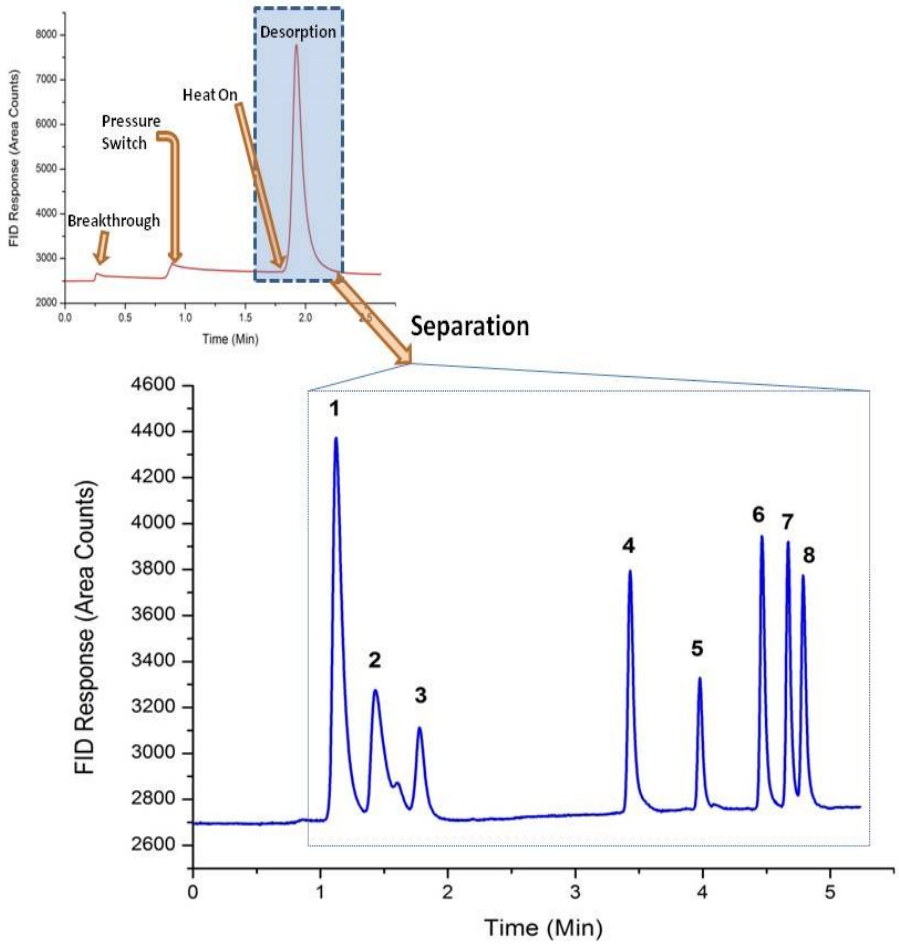

Figure 4.8. The performance of the μTPC with SNP-Tenax TA chip for eight VOCs. Adsorption conditions: 5 psi and 10:1 split injection ratio. Desorption conditions: 20 psi and temperature programming (30 °C – 15 °C/min – 90 °C). Compound identification: 1. chloroform, 2. isopropanol, 3. 1-propanol, 4. toluene, 5. tetrachloroethylene, 6. chlorobenzene, 7. ethylbenzene and 8. p-xylene.

4.2 The application of ISAM SNP coatings in GC micro separation columns (μSC)

4.2.1 The fabrication of μSC with thin film ISAM SNP as stationary phase— regular micro single capillary channel (μSCC) design and micro multi-capillary channels (μMCC) design

The regular μSC devices functionalized with thin film ISAM SNP had either a micro single capillary channel (μSCC 1 m-long, 150 μm-wide, 240 μm-deep), or 16 narrow micro multi-capillary channels (μMCC 25 cm-long, 30 μm-wide, 240 μm-deep) working in parallel. These HAR devices were fabricated by using standard MEMS processes, similar to the one described in section 4.1.1. Afterwards, the wafer was diced into individual devices after etching with the photoresist left on top. Selective deposition of ISAM SNP inside the channels was achieved by using a liftoff procedure explained below.

Keeping the photoresist on the μSC devices intact, the LbL deposition of SNP inside the HAR micro fluidic channels started with alternately dipping each device into a positively-charged long-chain polymeric aqueous solution (PAH), and then the negatively-charged SNP colloid. Because of the very narrow channels, the μMCC column deposition was performed using the SNP colloid at one third of the original concentration (7 wt.%) to prevent the formation of bulky nanoparticle structures between the channel walls that would plug the flow (Figure 4.11 C). The LbL deposition scheme presented here afforded a homogenous SNP coverage both on the interior microchannel surfaces and on the photoresist at the top of chip. After coating, the samples were rinsed thoroughly with DI water and dried with low flux nitrogen. After deposition of the desired number of bilayers, the devices were then dipped in acetone and sonicated for 12 minutes. This liftoff procedure removes the SNP deposited on the photoresist on top of the channel walls without removing the coating inside the channels, which is crucial for the sealing process with a Pyrex wafer.

After the same calcination and anodic bonding procedures described in section 4.1.3 and illustrated in Figure 4.9, deactivated capillary tubes were installed at the inlet and outlet ports using epoxy. The presence of active silanol (hydroxyl) groups on the surface of silica and SNP has been widely reported in the literature and is known to be detrimental to chromatographic performance. Deactivation of these groups using chlorosilanes has been shown to reduce peak broadening considerably. In this study, a 10 mM chlorodimethyloctadecyl silane (CDOS) solution in toluene was pumped into the chip by nitrogen (Figure 4.9) and allowed to sit overnight to deactivate the nanoparticles and glass surfaces.[2] The solvent was then removed by nitrogen prior to using the device for chromatographic analysis.

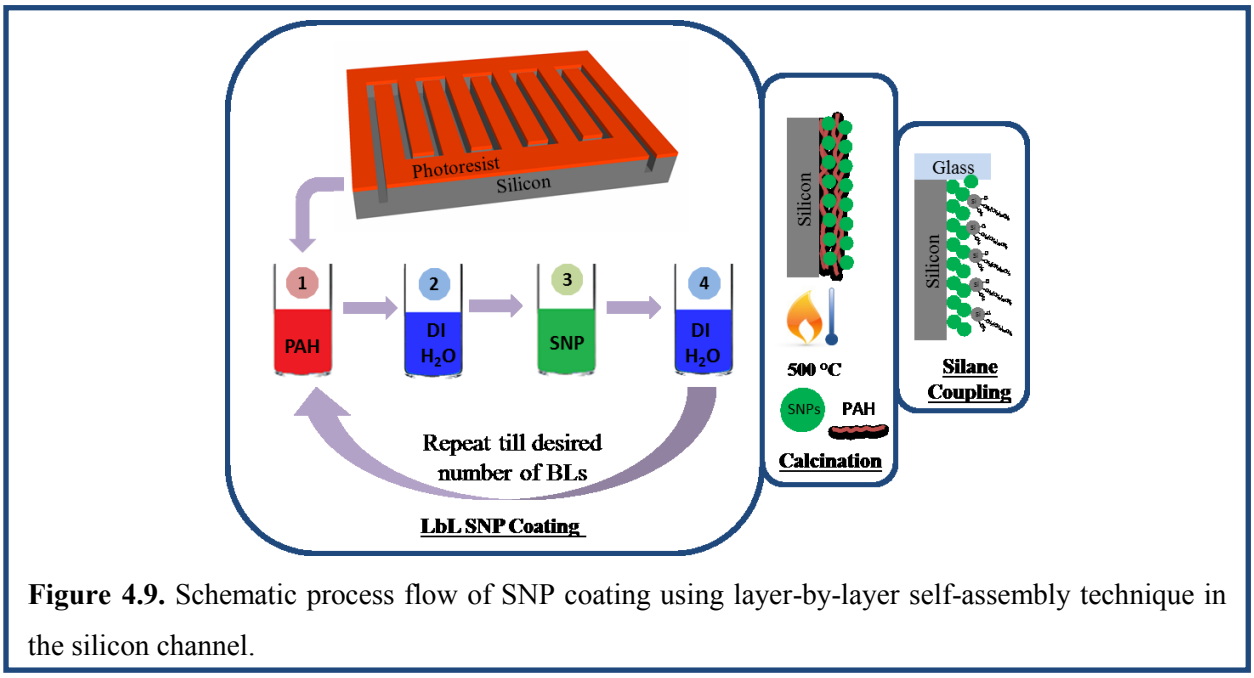

Figure 4.9. Schematic process flow of SNP coating using layer-by-layer self-assembly technique in the silicon channel.

4.2.2 The characterization of regular µSCs with thin film ISAM SNP as stationary phase

To validate the simplicity, repeatability, and robustness of the thin film ISAM SNP stationary phase deposition technique, the two HAR µGC column configurations (µSCC and

μMCC) were coated using SNP. The effect of the SNP coating thickness on chromatographic separations was also evaluated by coating μSCC devices with 5, 10 and 15 BL, respectively. The SEM micrographs (Figure 4.10 A-F) for the devices after calcination clearly show that the bottom and sidewalls of the trenches of μSCC were completely covered by an SNP layer of relatively uniform film thickness. Moreover, the lift-off procedure successfully removed the SNP from the top surface. The controllability of film thickness using the LbL approach is demonstrated by SEM micrographs of 5, 10 and 15 BL (Figure 3.10 G, F, H) deposited inside the silicon trenches, respectively. The thickness range measured on the surface inside the channel directly from the SEM at different locations are ~260 - 320 nm, ~400 - 490 nm, and ~560 - 610 nm for 5, 10, and 15 BL respectively. The range of each thickness (as high as a 20% deviation from the average thickness) is somewhat broader than what is typical for a commercial GC capillary coating (<5%). Nevertheless, this clearly demonstrates that film thicknesses are proportional to the number of coating steps and that the combination of microlithography and LbL self-assembly for selective SNP deposition on the interior surfaces of μGC columns can readily be achieved.

In addition to wide channel (150 μm) μSCC, the LbL coating method was used on narrow-width channels (30 μm) inside μMCC configurations. It was observed that the original concentration used for μSCC (20-21 wt.% in water) resulted in bulky nanoparticle "bridges" between the sidewalls due to the narrow channel widths in μMCC, resulting in channel clogging (Figure 4.11 C). The nanoparticle bridges were eliminated by reducing the original concentration of the SNP colloid (Figure 4.11 D) to 7 wt.%. Although a lower concentration of SNP colloid was used, the 10 BL coating inside the microfluidic channels has approximately the same thickness (380 nm, Figure 4.11 B) as the 10 BL coating inside the μSCC (Figure. 4.10 F). This

implies that a coating with SNP colloid at a lower concentration is sufficient to deposit a layer of SNP over the previous PAH layer to neutralize and reverse the surface charge, while the excess SNPs during the μSCC coating with the higher concentration colloid are most likely washed off during the rinsing steps.

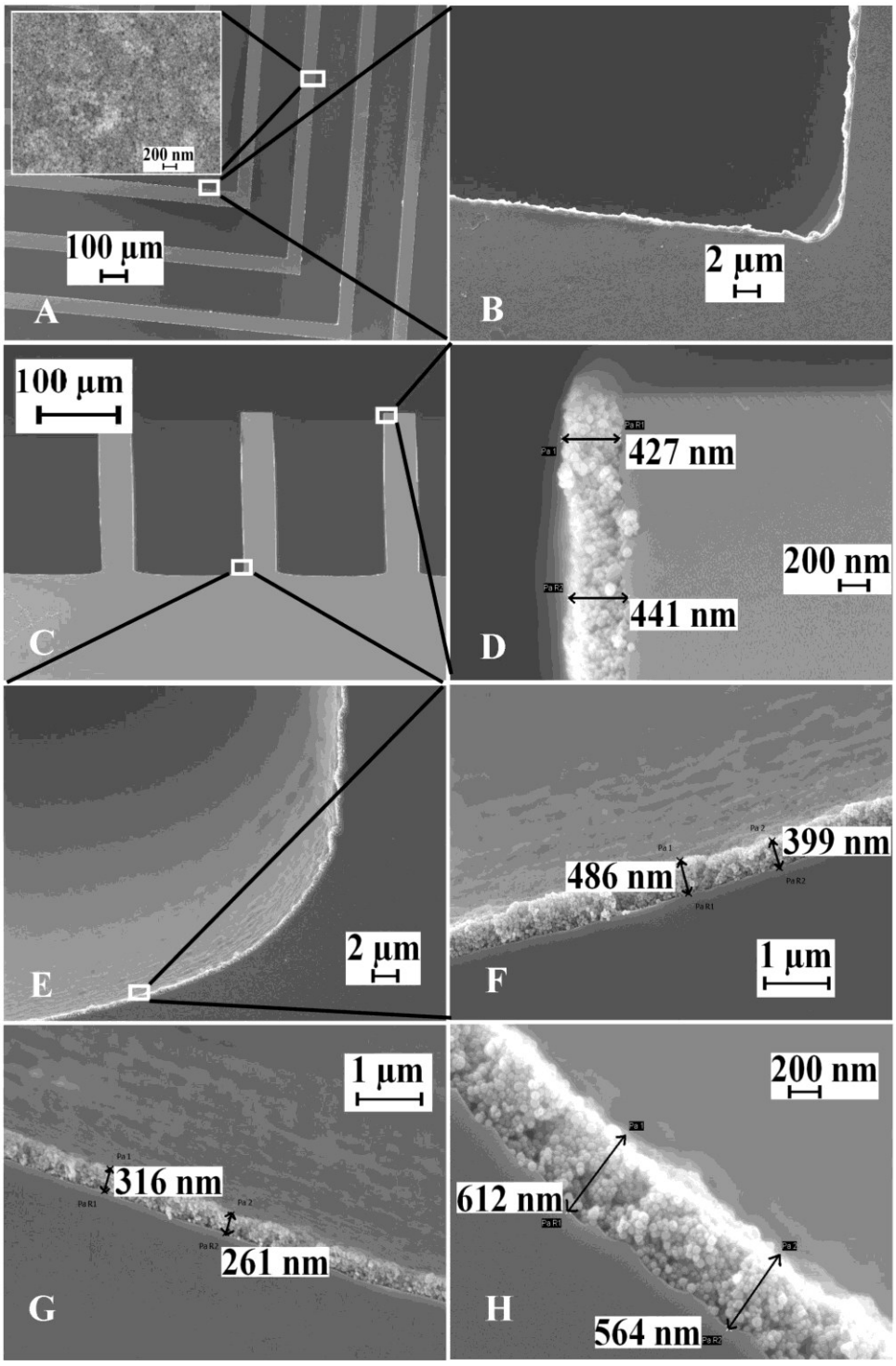

Figure 4.10. SEM images of the 10 BL SNP coated µSCC. (A) Top view and inset shows the coating on the bottom of the channel. (B) coating on the sidewall viewed from top. (C-F) cross-sectional view of channel with 10 BL SNP on the inner surfaces. (D) top of the sidewall, (E-F) bottom corner (F) 10, (G) 5 and (H) 15 BL SNP coating with thickness values.

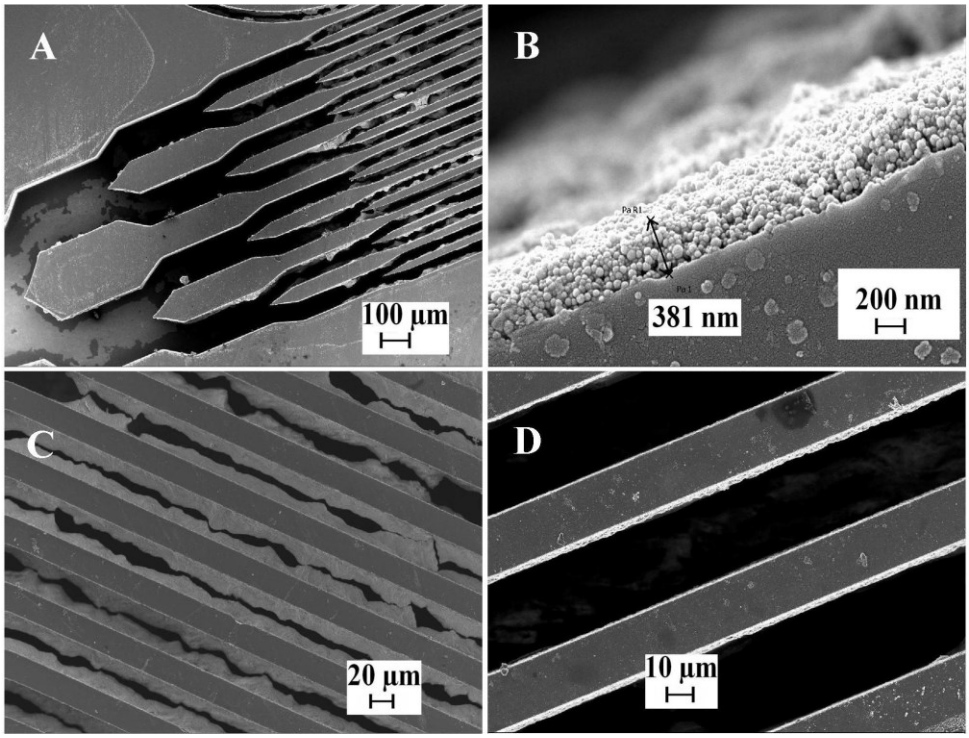

Figure 4.11. (A) SEM image of the inlet and 16 parallel channels of a µMCC and (B) its cross-section with 10 BL SNP coating on the sidewall of silicon channel with thickness value. Coatings on the sidewall of multi-capillary µGC column using SNP colloid with (C) original and (D) 7 wt.% concentration.

4.2.3 Separation results of regular µSCs with thin film ISAM SNP as stationary phase

The improvement in the separation performance from CDOS deactivation is illustrated in Figure 4.12; a mixture of C_{10}, C_{11} and C_{12} was used to test the µSCC before and after silane-coupling. The µGC column treated with silane clearly generated sharper and more symmetric peaks. The CDOS was specifically chosen for the deactivation, since the chlorinated end group readily reacts with active silanol groups on the SiO_2 surface to produce a covalent -Si-O-Si- bond. The long non-polar octadecyl chain also enhanced the column performance through interactions with the compounds being separated. Improvements in both chromatographic peak

symmetry and baseline were also observed for columns subjected to the deactivation process.

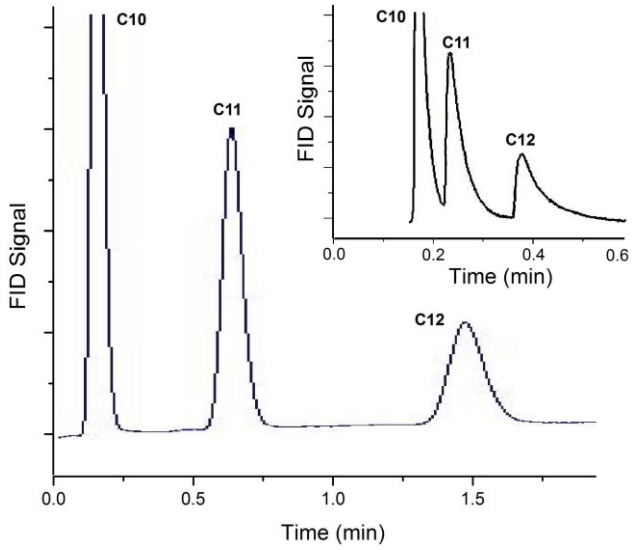

Figure 4.12. Improvement in separation performance after silane deactivation of 10 BL μSCC, inset shows column without silane treatment. Chromatographic conditions: 10 psi with 100:1 split injection ratio and 80 °C isothermal temperature.

As a first step of evaluation, the coating thickness for the reported μSCC was optimized using peak tailing/symmetry as a figure of merit. As discussed earlier, columns coated with 5, 10 and 15 BL of ISAM SNP provided different film thicknesses (Figure 4.10). All three columns were able to successfully resolve alkane test mixtures. Table V illustrates retention times for three alkanes on each device. As expected, the thickest film (15 BL) provided the longest retention times. However, 5 and 15 BL coated columns showed highly unsymmetric peaks, while the μSCC with 10 BL had highly symmetric peaks. Additional characterizations from this point for deviations due to variations in fabrication processes, coating stability and separation capabilities were therefore made with columns coated with 10 BL SNP. Deviations in fabrication processes were first considered, with ~10% variation in retention times observed for μSCC columns produced on two different wafers and coated with 10 BL of SNP (Table V). The separation results of the two devices closely resembled each other and had excellent peak

symmetry. Similarly, the long-term stability of the SNP coating under GC testing conditions was monitored by subjecting a 10 BL SNP coated µSCC to a conditioning process (constant flow at 7.5 psi at 160 °C for 24 hours). The SNP based coating was found to have a good stable baseline after this accelerated testing with only modest differences in peak quality and retention times. This demonstrated the ability to produce stable, consistent and robust stationary phases with small deviations in column performance.

Table V. Comparison of retention times (minutes) for three alkanes for 5, 10, 15 BL SNP coated µSCCs, and the same 10 BL µSCC after conditioning.

	C 10	C 12	C14
5 BL	0.01	0.05	0.92
10 BL	0.07	0.46	1.48
15 BL	0.11	0.68	1.65
2nd 10 BL	0.08	0.49	1.55
Conditioned 10 BL	0.05	0.30	1.40

The separation capability of an SNP coating with 10 BL for µSCC was successfully demonstrated using a series of alkanes (Figure 4.13) and a ten compound standard test mixture (Figure 4.14) containing a variety of commonly found volatile organic compounds (VOCs) to evaluate the resolving power of the SNP columns. The chromatograms obtained from these columns had excellent reproducibility from multiple injections.

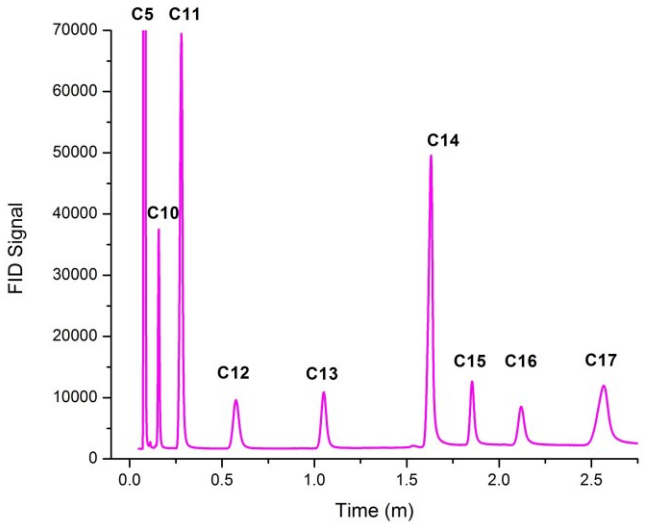

Figure 4.13. Separation of nine straight chain alkanes using a 10 BL SNP µSCC. Chromatographic conditions: 10 psi with 100:1 split injection ratio and temperature programming (50 °C - 120 °C at 70 °C /min).

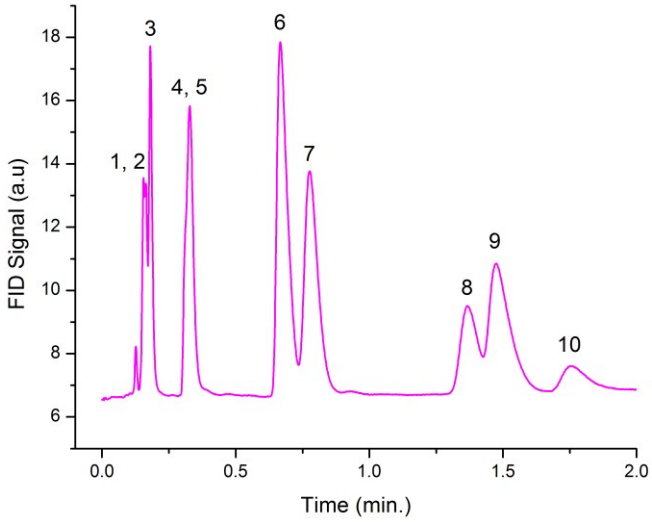

Figure 4.14. Separation of a ten component VOC mixture using a µSCC 10 BL SNP column. Chromatographic conditions: 10 psi with a 10:1 split injection ratio and temperature programming (30 °C - 50 °C at 10 °C /min). Compound identification: 1. dichloromethane; 2. chloroform; 3. carbon tetrachloride; 4. dibromomethane; 5. tetrachloroethylene; 6. toluene; 7. chlorobenzene; 8. bromobenzene; 9. p-xylene; 10. 1,1,2,2-tetrachloroethane.

In order to validate the proposed scheme using narrow channel dimensions, the LbL fabricated SNP coating was also used to functionalize a μMCC with reduced SNP concentrations as previously described. Figure 4.15 shows a chromatogram obtained from the alkane test mix using a 10 BL SNP coated 16 channel μMCC that was also silane treated. The reason for the shift in baseline has not been determined, but it is clear that retention times were markedly longer on the order of 3X compared to the μSCC in Figure 4.13) and potentially provide for greater separating capabilities. These results also indicated that these newly developed SNP coating schemes should be applicable to other channel geometries and column configurations.

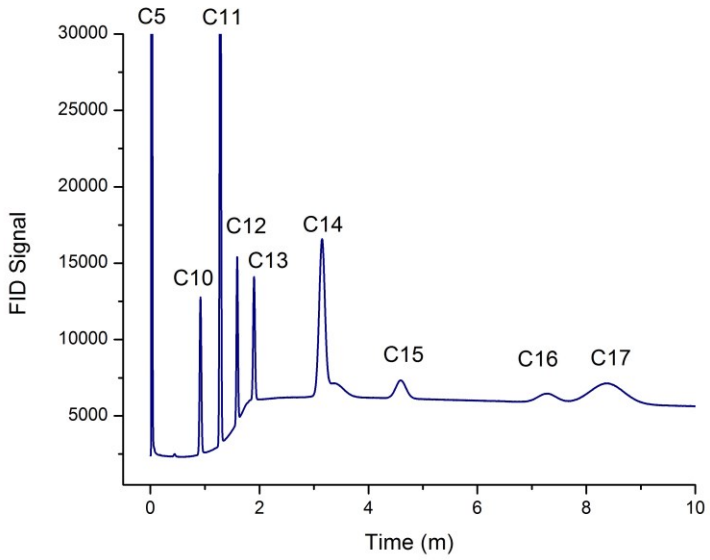

Figure 4.15. Separation performance of a 16 channel μMCC functionalized with 10 BL SNP using the alkane test mixture. Chromatographic conditions: 10 psi with 100:1 split injection ratio and temperature program (50 °C -120 °C at 70 °C /min).

As discussed in section 2.3.3, the figure of merit commonly used for column performance is height equivalent to a theoretical plate (HETP), $HETP=L/N$, where L is the length of the column and N is the number of plates in the column, as determined experimentally from peak retention times (t_r) and widths at half the peak height ($w_{1/2}$):

$$N = \left(\frac{t_r}{w_{1/2}}\right)^2 \qquad (4\text{-}1)$$

To evaluate the efficiency of the ISAM SNP functionalized μGC columns, the theoretical plate numbers were obtained over a range of column pressures using dodecane diluted in dichloromethane at 65 °C. The linear velocity of the mobile phase was estimated using methane injections. The maximum plate numbers for the 1 m-long μSCC and 25 cm-long μMCC columns were experimentally calculated to be 930/m and 4750/m respectively. The much larger plate number for the multi-capillary column is best explained by the narrower channels, which enhance interactions with the analytes and improves the overall capacity of the column. Plots showing the correlation of the inlet pressure to gas velocity and HETP versus gas velocity are shown in Figure 4.16. The linear velocity of the mobile phase was estimated from correlating the inlet pressure to the retention time obtained from methane injections, which was assumed to essentially be unretained. In addition to the much lower HETP values and higher plate numbers, the narrower channels of μMCC provide relatively flat Golay plots over a broader range of flow rates compared to μSCC. Golay plots show the dependence of HETP on the speed of carrier gas. They are used to determine the optimal flow speed to get lowest HETP and thus highest plate numbers.

The static coating of SNPs in ethanol suspension, reported earlier for capillary columns,[3] resulted in agglomeration of nanoparticles, affording a non-uniform film. The effect of this non-uniformity was also demonstrated in poor chromatographic performance. In the same article, the authors integrated IL with SNP to develop a uniform stationary phase (0.4 μm ~ 0.6 μm) with improved separation characteristics. Comparatively, 10 BL SNP coating scheme with a similar film thickness (0.4 μm ~ 0.5 μm) proposed here enable a homogeneous, stable, controllable and

conformal stationary phase bed. Moreover, by incorporating calcination and silane deactivation, the chromatographic performance (especially peak symmetry) of our LbL technique was superior compared to the reported static coating methods.[3]

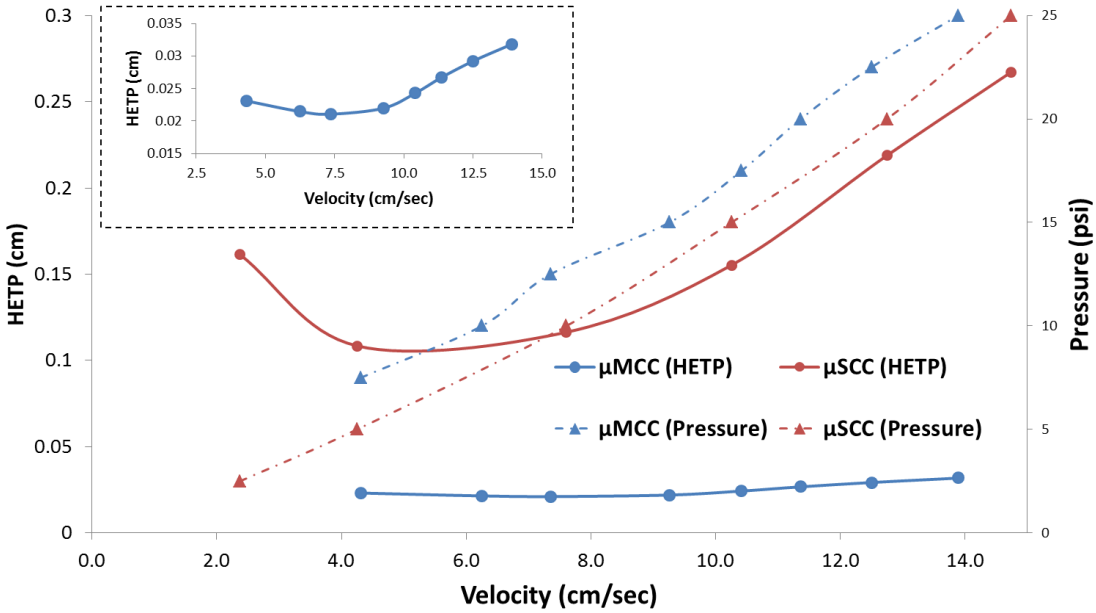

Figure 4.16. HETP-gas velocity-pressure plots for µSCC and µMCC with 10 BL SNP coating. The dashed lines with triangle markers are plots of inlet pressure against gas velocity using methane vapor as an unretained marker. The solid lines with circular markers are Golay plots (HETP versus gas velocity). Inset represents the µMCC results at zoomed in scale.

4.2.4 The design and fabrication of a new class of unidirectional width-modulated columns (µWMCs)

As mentioned in Section 4.2.3, the efficiency of a chromatographic column is expressed in terms of either a theoretical plate number (N) or height-equivalent-to-a-theoretical-plate ($HETP=L/N$). As a general rule, a high efficiency column has higher theoretical plates and less band-broadening (small HETP term). HETP could be further expanded to include the effects of

diffusion in the mobile phase and mass-transfer in the mobile and stationary phases. For rectangular channels, HETP is given by [4]

$$HETP = \frac{2D_g}{\bar{u}} f_1 f_2 + \left[\frac{(1+9k+25.5\,k^2)}{105(k+1)^2} \frac{w^2}{D_g} \frac{f_1}{f_2} + \frac{2}{3}\frac{k}{(k+1)^2}\frac{(w+h)^2 d^2_f}{D_s h^2}\right] \bar{u} \qquad (4\text{-}2)$$

In which D_g and D_s are the binary diffusion coefficients in the mobile and stationary phase, $\bar{u}$ stands for the linear gas velocity, f_1 and f_2 are the Giddings-Golay and Martin-James gas compression coefficients, respectively, k is a retention factor that is characteristic of a stationary phase, w stands for channel width and h for the channel height/depth.

To simplify the analysis, we ignore diffusion in the mobile phase (1st term) and also assume a very thin stationary phase film (small d_f -term). Therefore, we can neglect the contribution of band-broadening due to diffusion in the stationary phase (3rd term) in Eq. 4-2. Under these assumptions, the HETP becomes directly proportional to the square root of column width

$$HETP \propto w^2 \qquad (4\text{-}3)$$

It is clear from Eq. 4-3 that columns with smaller width will provide more efficient separations and column-width is one of the critical design parameters. Moreover, if the width of a column is gradually reduced along the length, then HETP will also decrease locally and effectively the overall HETP values will reduce. Therefore, modulation of the width of the column was carried out and two new micro-fabricated width modulated columns (μWMC) were introduced, as shown in Figure 4.17. The width of the linearly-variable-column (LVC) was modulated from 120 μm to 20 μm at 1 μm/cm (Fig. 4.17 b), and the step-gradient column (SGC)

was modulated in 5 steps (120 µm, 95 µm, 70 µm, 45 µm and 20 µm) each with 20 cm length (Fig. 4.17 c). Moreover, for the step gradient column, the interconnections between the steps were gradually varied over the length of 700 µm. The separation capabilities of these newly developed µWMCs were realized by utilizing the LbL self-assembly technique to get a highly-stable ISAM SNP stationary phase.

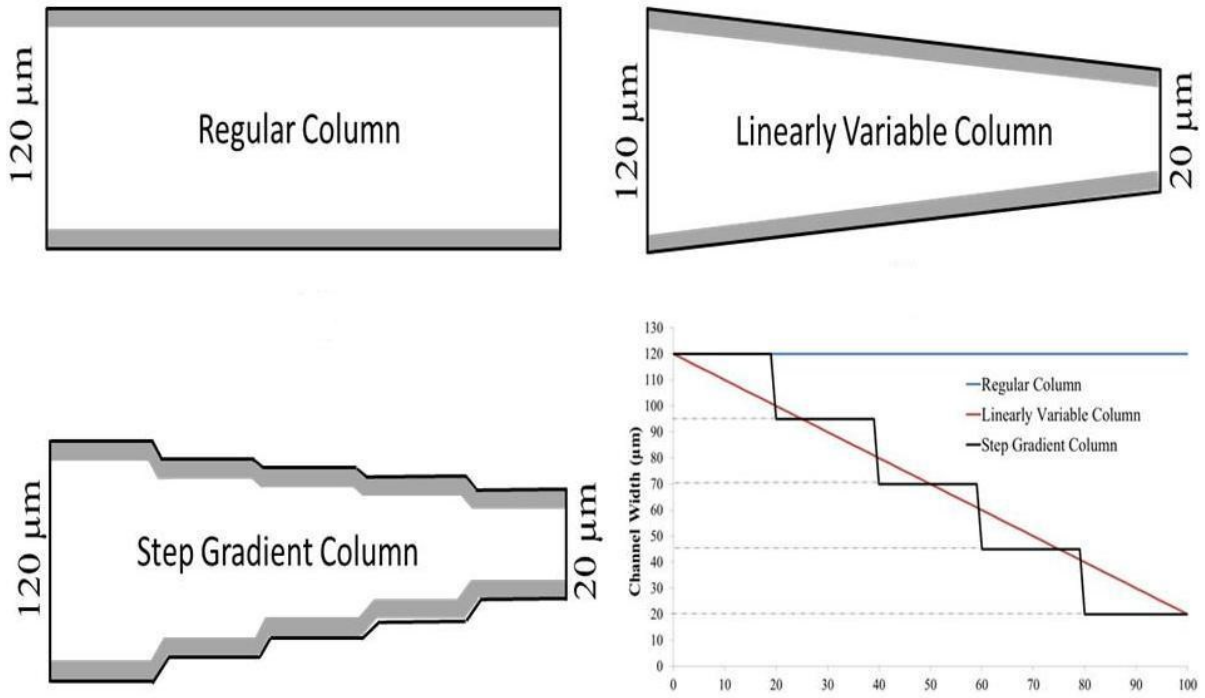

Figure 4.17. Channel profiles of 1 m-long regular, linearly variable, and step gradient columns. The graph shows the plot for channel width versus channel length.

The first several steps of the fabrication procedure for these µWMCs were almost the same as the one used for regular µSCs described in section 4.2.1. Then after etching, instead of being directly diced into individual devices with photoresist left on top, the etched silicon substrate was first cleaned with acetone and secondly by oxygen plasma to ensure the removal of photoresist and the residual passivation polymer deposited during etching. Following the cleaning steps, the etched wafer was sealed with a Pyrex wafer using an anodic bonding station at 400 °C and 1250

V for 45 minutes. Subsequently, the bonded wafer was diced to expose two micro-fluidic ports of a number of serially connected devices for a new simultaneous stationary phase coating technique to that we developed achieve high-throughput (Fig. 4.18, 1st cut).

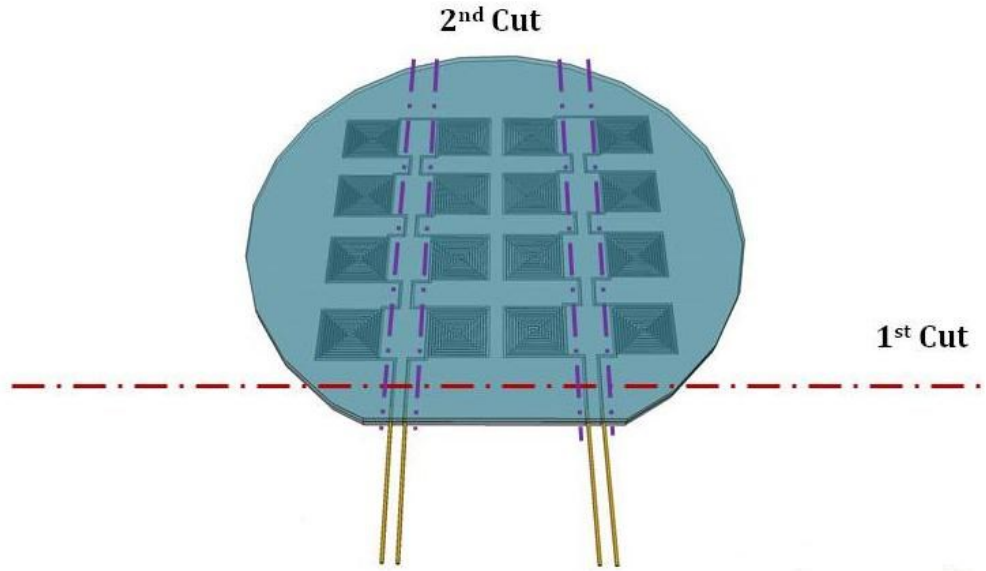

Figure 4.18. Schematic representation of newly developed method for serial stationary phase coating utilizing the LbL method to enable complete coverage of microchannel.

Due to the very narrow channel sections (20 μm) within these μWMCs, a different LbL self-assembly approach was applied to incorporate thin film ISAM SNP as the stationary state, because the surface tension of water prevents the solutions used in the regular LbL fabrication from getting into the very narrow channels. After the first dicing, 25 cm-long deactivated fused silica capillary tubes (outer diameter 220 μm, inner diameter 100 μm) were attached to the micro-fluidic ports with epoxy. Next, dry nitrogen and DI water were passed through the devices to remove any dust gathered during dicing. The LbL coating started by alternately passing a positively-charged PAH solution and negatively-charged SNP colloid through a number of serially connected multiple devices for three minutes to form one bilayer. Each PAH and SNP coating step was followed by a 3 minute DI water rinsing step. In the present work, this process

was terminated after 10 BL of PAH and SNP. Similar to the earlier work for narrow channel-width (30 µm) multicapillary columns discussed in section 4.3.2, the original concentration of the SNP colloid was reduced to a third of its original value in order to achieve a uniform film thickness. At the end, the devices were thoroughly purged by passing DI water and dry nitrogen at low pressure for 15 minutes. The process is demonstrated in Figure 4.19.

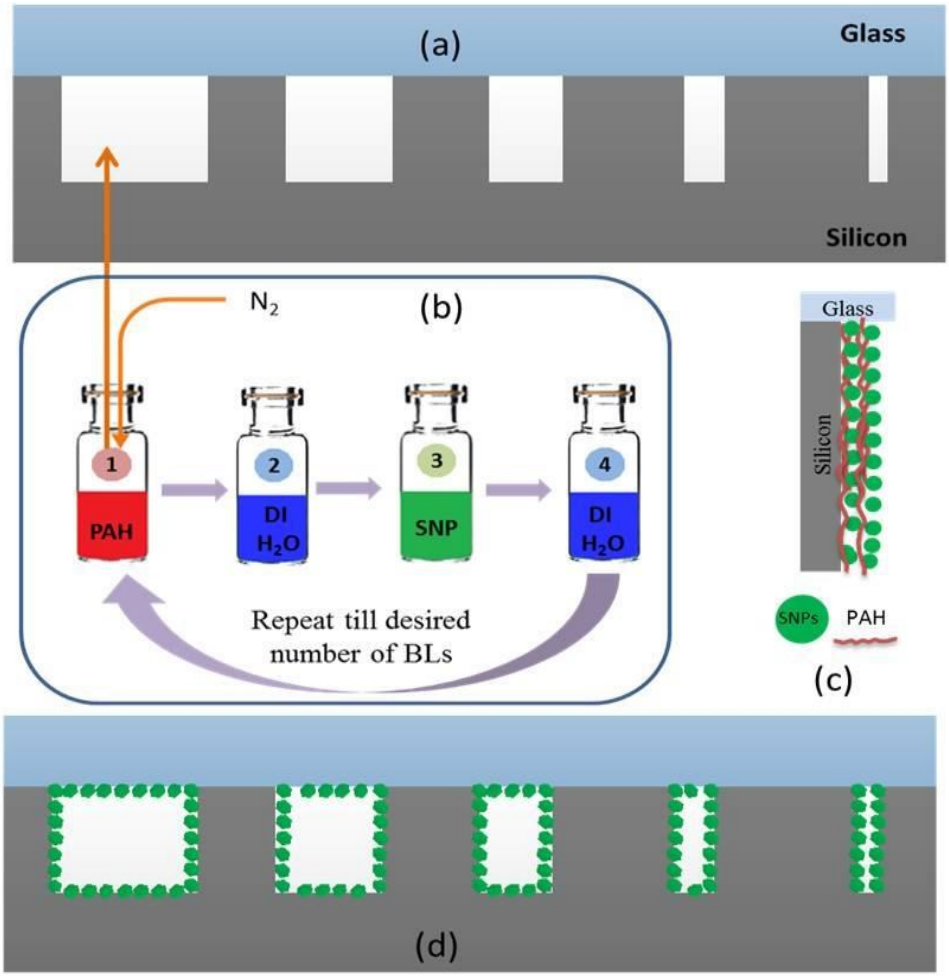

Figure 4.19. Process flow a) anisotropic etching followed by anodic bonding, b) LbL coating till 10 BL using SNP, c) 2 BL shown inside channel, and d) columns after calcination (500 °C) and silane coupling.

Next, the capillary tubes were removed and the serially connected columns were diced into individual devices (Figure 4.18, 2nd cut). Calcination was performed afterwards at 500 °C for 8

hours to remove the PAH layer and fuse SNP together, resulting in a stable and homogenous SNP film. Following the calcination step, deactivated capillary tubes were fixed to the inlet and outlet ports of individual columns using epoxy. Before performing chromatographic separations, the surface of the SNP was deactivated by filling each column with 10 mM CDOS diluted in toluene for 12 hours, which served as the deactivation process as discussed in section 4.2.1.

4.2.5 The characterization of μWMCs with thin film ISAM SNP as stationary phase

The characterization of μWMCs with a constant SNP stationary phase film was performed using SEM (Fig. 4.20). First, it was verified from the SEM images (top and cross-sectional views) that only the column width was modulated (Fig. 4.20 a-b) without effectively changing the channel depth. It is pertinent to note that the effect of modulation in column depth on chromatographic separation could also be studied in the future and easily achieved by changing the DRIE etch parameters. Moreover, by employing the newly developed LbL SNP coating method after anodic bonding, a complete coverage of the microfluidic channel including the glass surface was realized (Fig. 4.20 C). This complete coverage of the separation channel results in improved analyte-stationary phase interaction. The film thickness measured at different locations (top, bottom and sidewalls) inside the modulating microfluidic channel show that 10 BL of SNP yielded roughly a constant film thickness in the range of 400~500 nm (Fig. 4.20 C). This is also consistent with the LbL coating method reported in section 4.2.2 and demonstrates that the film thickness is proportional to the number of coating steps.

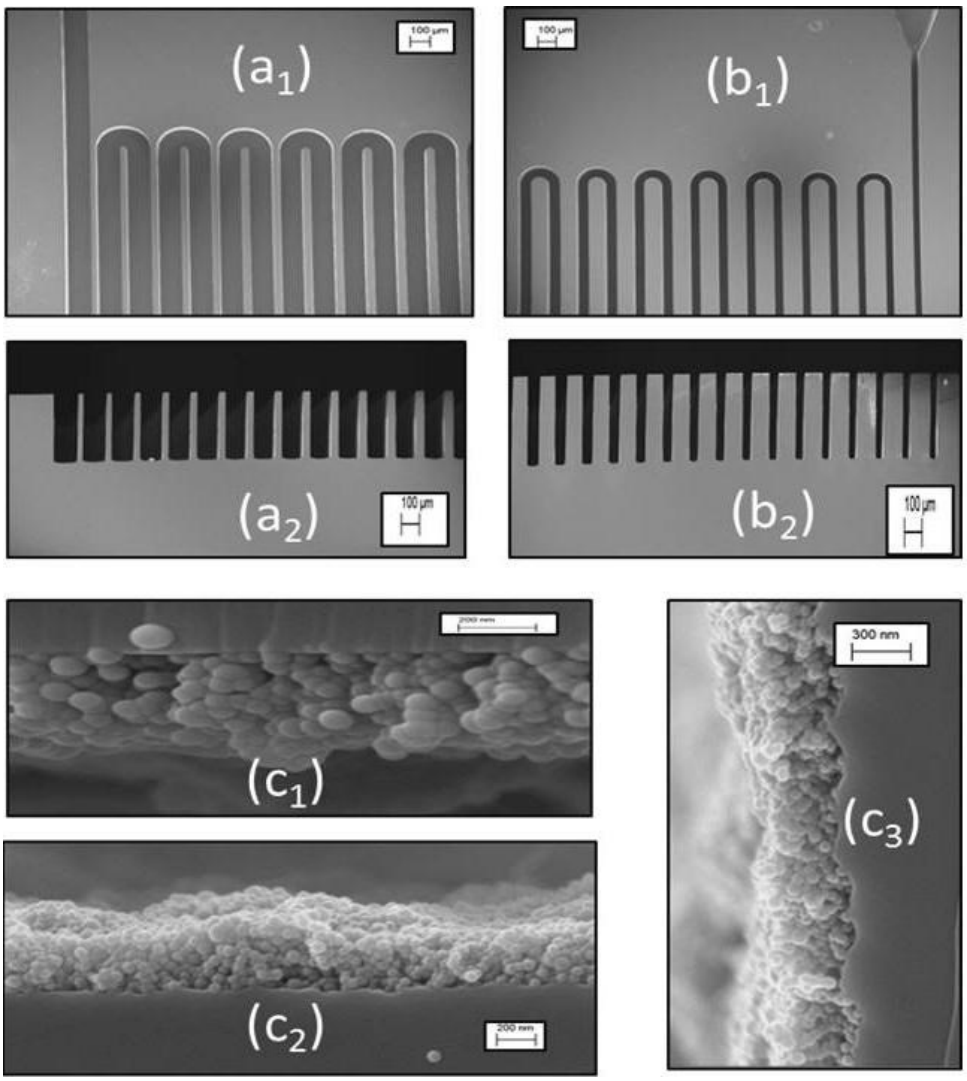

Figure 4.20. Scanning electron micrographs of µWMC before bonding and SNP coating (a-b), at 120 µm inlet (a1) top view and (a2) cross sectional view and at 20 µm inlet (b1) top view and (b2) cross-sectional view. LbL SNP coating after calcination and silane-coupling performed after bonding on (c1) glass surface (c2) bottom of the channel and along (c3) side-wall.

4.2.6 Separation results of µWMCs with thin film ISAM SNPs as stationary phase

Since the newly developed LVC and SGC (µWMCs) configurations have microfluidic ports with different dimensions (i.e., 20 µm and 120 µm), it can be expected that the chromatographic

response (retention times, flow rate, and plate number) using each port as an inlet will be different. Therefore, these μWMCs cannot be considered bidirectional like regular columns are. So the presented chromatographic parameters were first analyzed utilizing both inlets. The separation performance (plate number *N*) of the columns was evaluated by using eq. (4-1) in section 4.2.3.

It can be seen from Table VI that the inlet selection for μWMCs plays an important role, with a significant difference in the plate numbers and retention times. It is clearly demonstrated that the SGC provides a higher plate number (N_{max}=6859 plates/meter) compared to the LVC (N_{max}=5850 plates/meter). The higher plate numbers in the proposed μWMCs was attributed to a gradual change in the width of the column and the stationary phase thickness. The analytes experience either a gradual increase in solute-stationary phase interaction (using 120 μm as an inlet port) along the column length or get separated fast at the start of the column within the narrower column region when the injector is connected to a 20 μm column port. It was shown in Table VI that the latter scenario provides an enhanced separation performance especially for the SGC. Furthermore, the LVC provides longer retention times than the SGC. Therefore, in order to achieve faster separations, the SGC should be utilized, but the LVC provide better resolution. It can be further deduced that for both the μWMCs designs utilizing 20 μm ports as inlets provide better separation efficiencies. Therefore, all the chromatographic results presented hereafter utilize the 20 μm ports as column inlets.

Table VI: Retention times and plate numbers of µWMCs and regular columns at 0.3 ml/min flow rate using n-nonane as a probe.

Column Type		Retention time (min)	Maximum Plate Number (N_{max})
Regular		1.054	3522
Linearly Variable	20 µm Inlet	1.041	5580
	120 µm Inlet	0.778	5496
Step Gradient	20 µm inlet	0.457	6859
	120 µm inlet	0.643	5784

From the Golay plots (Fig. 4.21), it is apparent that both LVC and SGC show superior performance compared to the regular columns (N_{max}=3500 plates/m) for all flow rates.

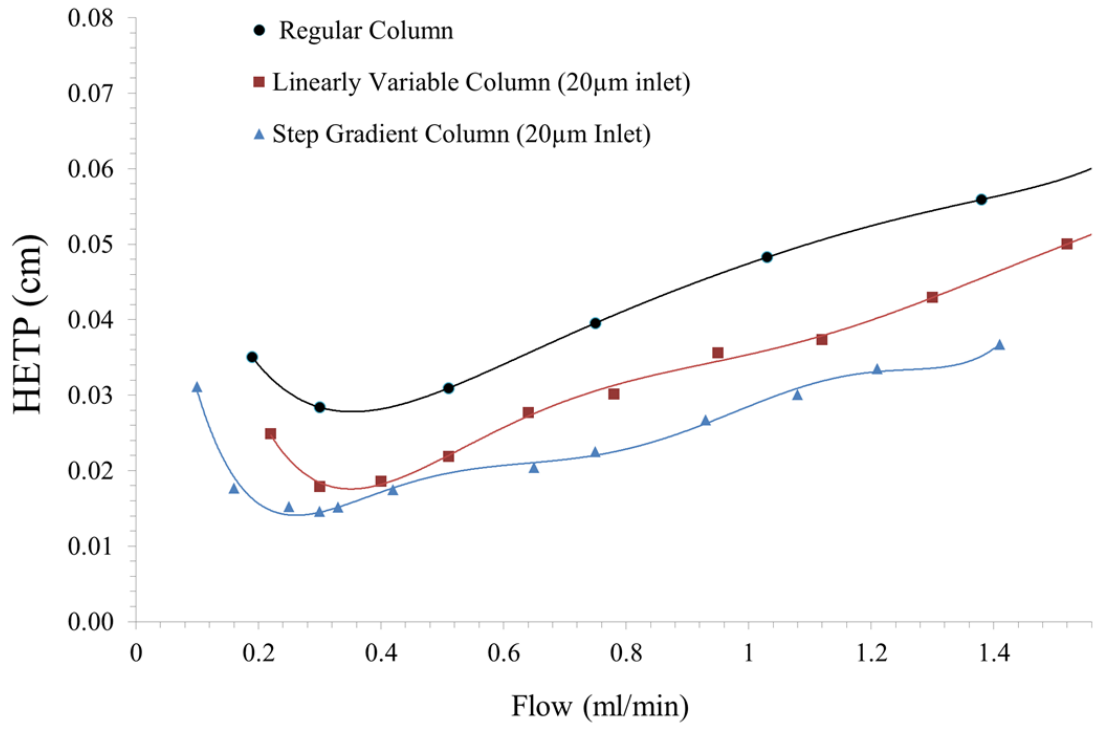

Figure 4.21. Golay plots for different inlets of µWMC and regular column using nonane as a marker under isothermal conditions at 50 °C and 1 µL sample injection.

In order to optimize the GC analysis, apart from the retention time and plate number, the resolution should also be characterized. Resolution, a characteristic of the separation of two adjacent peaks, is calculated according to [5]

$$\boldsymbol{R = 2 * \left\{ \frac{t_{r_b} - t_{r_a}}{w_b + w_a} \right\}} \qquad (4\text{-}4)$$

wherein R is the resolution, $\boldsymbol{t_{r_b}}$ and $\boldsymbol{t_{r_a}}$ are the retention times, and w_a and w_b are peak widths at half heights of corresponding compounds a and b, respectively.

Similar to HETP analysis, the μWMC outperformed the fixed dimensional regular columns in terms of resolution between *n*-nonane and *n*-decane under isothermal conditions (Fig. 4.22). The effect of peak resolution was further demonstrated by the separation of a custom-made hydrocarbon mixture with nine compounds. It is clear from the separation results (Fig. 4.23) that under the same flow rates the LVC was able to resolve all the nine compounds, while a regular microfabricated column was only able to resolve seven compounds in the test mixture. Moreover, it is concluded that μWMCs are more suitable for the separation of compounds with lower boiling points. Additionally, we mention that the SGC is only able to separate eight compounds in the sample test mixture (not shown).

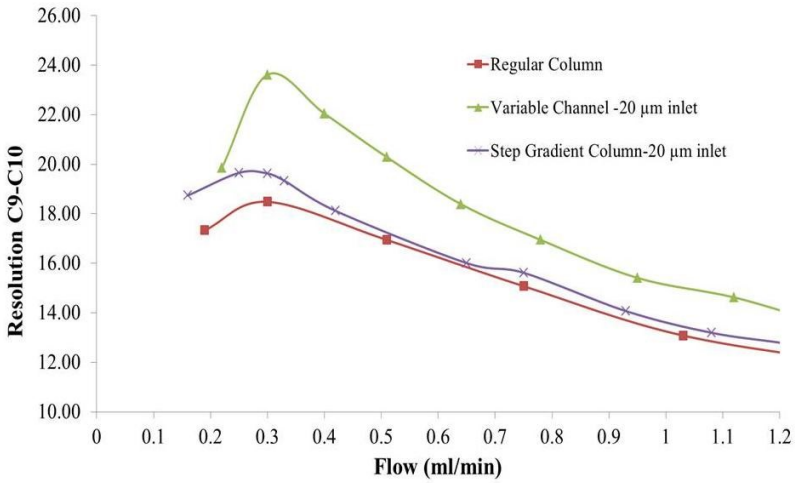

Figure 4.22. Resolution between *n*-nonane and *n*-decane under isothermal conditions at 50 °C for different types of µWMC and regular column.

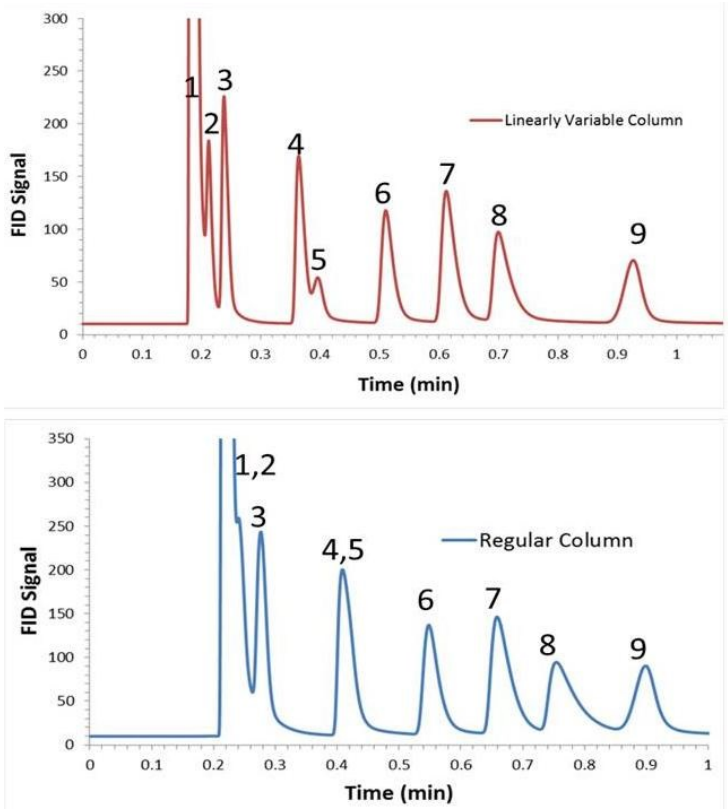

Figure 4.23. Separation results of a test mixture at 0.3 ml/min flow rate, 50 °C isothermal temperature and 100:1 split ratio. Compound identification in the order of elution (1) dichloromethane-solvent, (2) *n*-hexane, (3) benzene, (4) toluene, (5) tetrachloroethylene, (6) chlorobenzene, (7) ethylbenzene, (8) *p*-xylene, (9) *n*-nonane.

4.3 The application of thin film ISAM gold nanoparticle (GNP) coatings in μSC for incorporating thiol as stationary phase

4.3.1 The fabrication of micro semi-packed columns (μSPCs) with 3D undercutting profile

A new type SPCs with 3D undercutting profile that incorporate gold coatings including ISAM SNP for further thiol stationary phase was designed and fabricated by Shakeel of VT MEMS LAB. The undercutting profile (Figure 4.25) on the microposts of μSPC was found to assist the metal lift off from the top surface of the microposts for the Pyrex bonding.

The fabrication was through a modified anisotropic etching and lift-off process. Basically, as the first step, typical lithography procedure was still used for the μGC fabrication as described in section 4.1.1, only the wafer was not hard-baked after photoresist development; this further improved the metal lift-off process, which will be discussed in detail later. Although the micropillars (μ-pillars) were designed with 20 μm-diameters (Figure 4.24), anisotropic etching resulted in a ~3 μm lateral etching eventually producing ~17 μm μ-pillars (Figure 4.25 b). In the second step, the anisotropically etched silicon wafer was etched for 2 minutes using a Trion reactive ion etching (RIE) system to remove the passivation layer deposited on the etched surfaces during the previous DRIE process. It is important to note that without this step, undercutting of silicon was not possible since all the vertical surfaces were covered with passivated polymer from the first step. Similarly, a low-powered RIE system was found to be more suitable compared to a DRIE system for this step. Moreover, it was found during SEM imaging that the interface between the photoresist and top silicon surface was also cleared from residual photoresist/passivation polymer as shown in Figure 4.25 c. This helped in achieving the required undercut. In the last step, the undercutting of HAR microstructures was carried out using an isotropic etch recipe with fluorine based chemistry (SF_6) at 0 °C inside a DRIE. The overall

thickness of the µ-pillar was further reduced by ~3 µm due to isotropic etching. The detailed etch profile after 3D undercutting is shown in Figure 4.25 d. Keeping the photoresist intact, thin film ISAM GNP deposition was carried out in the next steps.

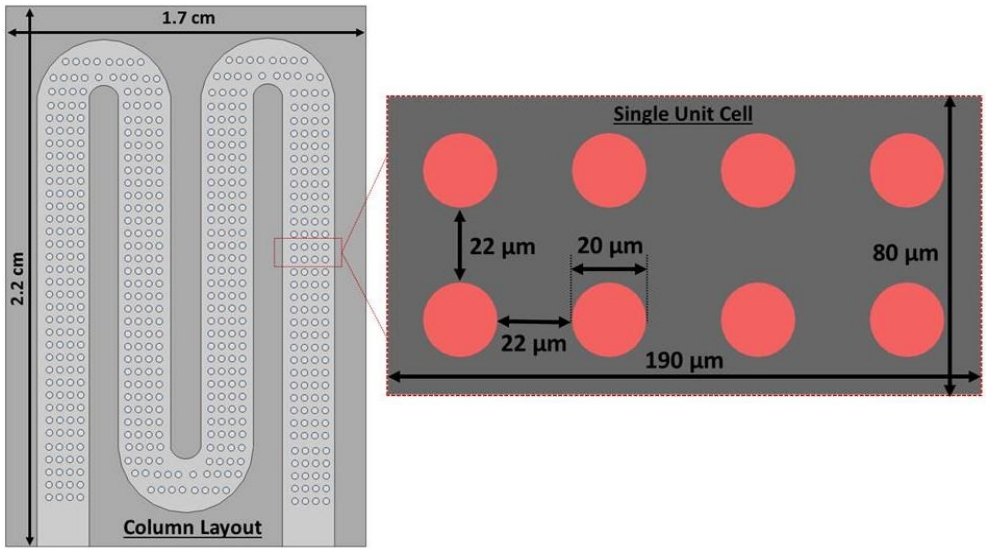

Figure 4.24. Layout (top view) of a 1 m-long µSPC showing critical dimensions.

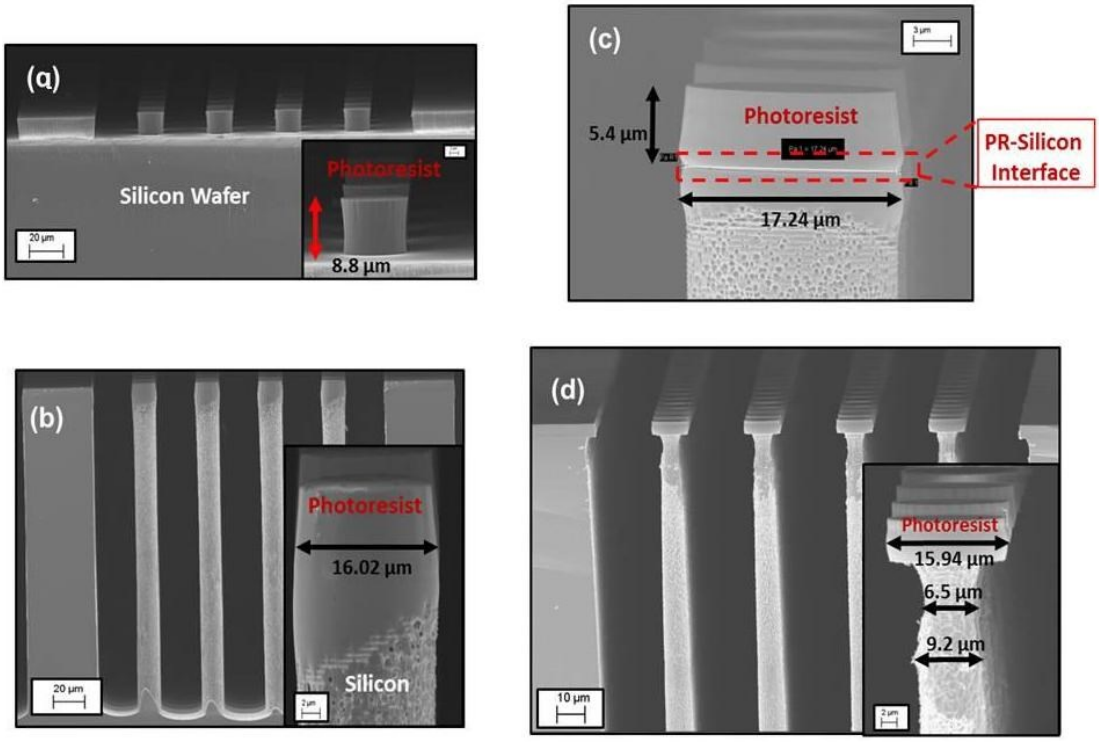

Figure 4.25. SEM micrographs of a device after different fabrication steps (a) after lithography (b) after anisotropic etching using DRIE (c) O_2 plasma etch of passivation polymer in Trion RIE (d) under-etching of high-aspect ratio micropillars in DRIE using isotropic etching. Insets show the images at magnified scale.

4.3.2 The incorporation of thin film ISAM GNP coating in the µSPCs with 3D undercutting profile

With the photoresist intact, the etched silicon wafer was first diced into the individual devices. Then, instead of the SNP colloid, GNP colloid (3 nm in diameter, Purest Colloids) as anionic material was used with PAH as polycation for the LbL self-assembly of thin film ISAM GNP coatings. The deposition procedure was the same as the one used for the CNC fabrication for ISAM bending actuators described in section 3.1.2.

In the current work, µSPCs were coated with 30, 50 and 100 BL of PAH/GNP. After LbL

coating, each device was dried with a low flux nitrogen gas and dipped in acetone followed by sonication for 5 minutes to achieve the metal lift-off. Similar to the ISAM SNP case, the devices were placed in an oven at 500 ºC for 4 hours to burn off the PAH, leaving behind only an evenly distributed GNP coating with nanoscale roughness on the desired microsurfaces.

As comparison, μSPCs with another type of thin film gold coating for the following incorporation of thiol as the stationary phase were also fabricated using e-beam evaporation.

4.3.3 Anodic bonding and functionalization

Following the thin film gold coating, each μSPC was sealed with a Pyrex wafer using a custom made anodic bonding station. Approximately 30 cm-long glass capillary tubing was glued using epoxy to each port of silicon-glass chip, providing a fluidic interface between the chip and GC oven.

Then, surface deactivation was performed to reduce the peak deformation/tailing during chromatographic separation. Similar to the procedure reported in section 4.2.1, each μSPC was first treated with a 10 mM CDOS (diluted in toluene) for 12 hours at room temperature to improve the peak symmetry. Following the deactivation, the self-assembly of octadecanethiol on a gold surface was exploited to create a gas-solid stationary phase [6].

$$C_{18}SH_{38} + Au^0 \xrightarrow{SAM} [C_{18}S^-H_{37} + Au^+] + {}^1/_2\, H_2$$

For the thiol self-assembly, each column was filled with 2 mM octadecanethiol ($C_{18}H_{37}SH$) in hexane, sealed at both ends using septa, and kept at room temperature for 6 hours. The entire fabrication procedure is illustrated in Figure 4.26.

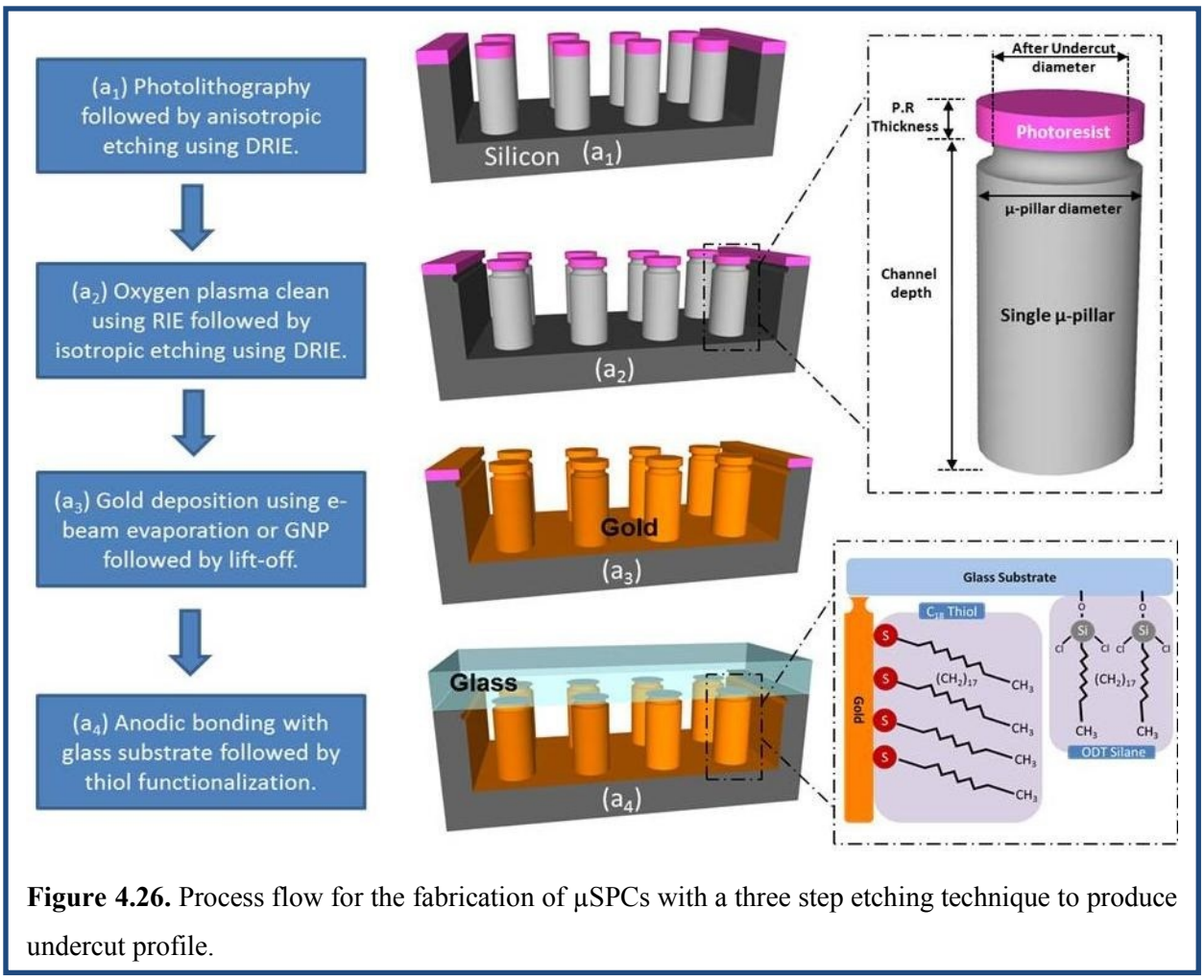

Figure 4.26. Process flow for the fabrication of μSPCs with a three step etching technique to produce undercut profile.

4.3.4 Performance of the μSPCs

The contribution of thin film ISAM GNP deposited using LbL self-assembly was first tested before any functionalization steps. Figure 4.27 clearly demonstrated that the GNP layer (an evaporated gold film shows similar behavior but is not shown) is inadequate for GC separations. Before performing any chromatographic separations on functionalized columns, each device was first purged with a constant flow of dry nitrogen for 30 minutes and connected to a conventional GC oven and slowly heated from room temperature to 150 ºC (2 ºC/min) with a constant inlet pressure of 7.5 psi until a stable signal baseline was observed. Figure 4.27 also

shows that µSPCs with thiol functionalized GNP (100 BL) coating were able to separate a simple alkane mixture. It is important to note that 30 and 50 BL GNP coated columns performed poorly in comparison to 100 BL due to incomplete coverage of the etched channels with nanoparticles. Therefore, only 100 BL coated columns were used for further GC analysis along with evaporated gold columns.

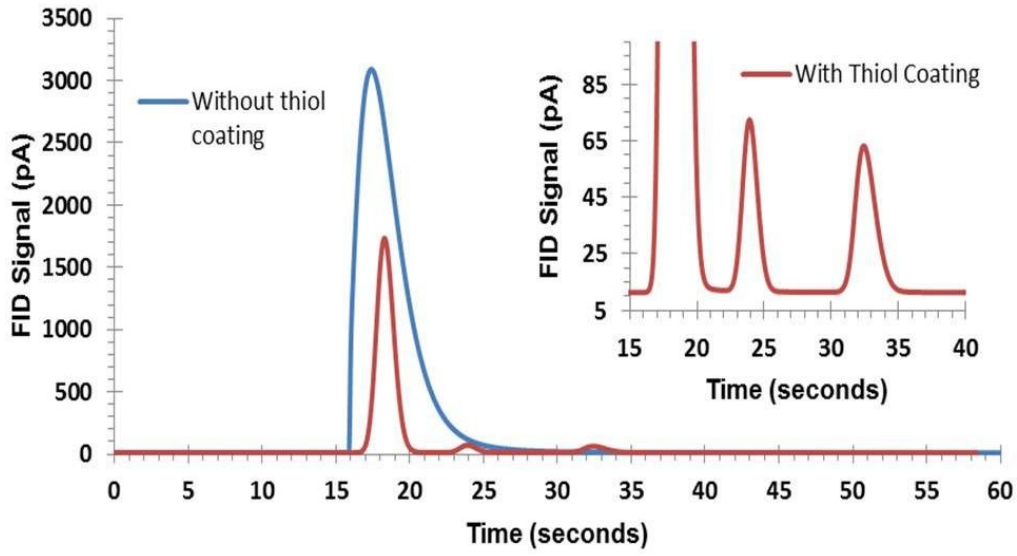

Figure 4.27. Separation performance of an uncoated and a thiol coated GNP column using n-nonane and *n*-decane (diluted in dichloromethane) as probes. Column tested at 50 ºC, 5 psi head pressure, 200:1 split ratio and 0.1 µL sample injection.

Both kinetic and thermodynamic properties of µSPCs with thiol stationary phases were evaluated using Golay and Van't Hoff plots. Figure 4.28 shows Golay plots of both GNP and evaporated gold µSPCs, generated using *n*-decane as a probe under isothermal conditions (35 ºC, 0.1 µL injection volume, split ratio 200:1). The optimum linear carrier gas velocity of 37 cm/sec was calculated providing a minimum $HETP_{eff}$ value of 0.0376 cm (evaporated gold). It is desirable to operate columns at higher linear velocities in order to reduce the analysis time. The flatness of the HETP curve above optimum linear velocities, a characteristic of µSPCs, shows

that there is small loss in separation efficiencies at high velocities. Figure 4.28 also shows a linear correlation between the inlet/head pressure and the corresponding calculated linear carrier gas velocity. Both gold-thiol coatings were found to be highly stable under GC testing conditions (maximum pressure of 30 psi and temperature up to 175 °C) and after multiple sample injections (200).

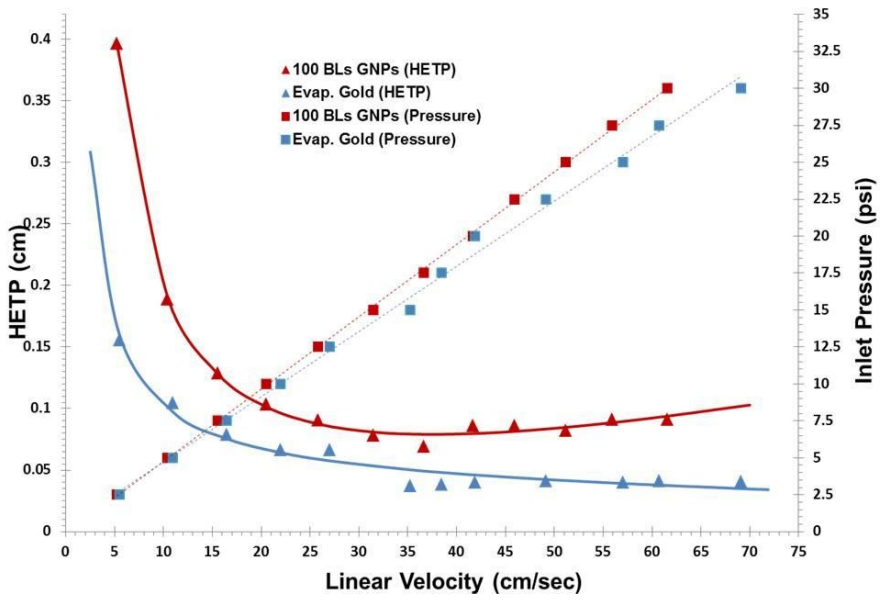

Figure 4.28. Golay plots of evaporated gold (blue color) and GNP (red) based SPCs using *n*-decane as a marker under isothermal conditions (35 °C) with 0.1 µL sample injection and 200:1 split ratio (head pressure varied from 2.5 psi to 30 psi). Triangular markers represent HETP (solid lines) values, while square markers represent pressure (dotted lines).

In general, the chromatographic performance of thiol functionalized evaporated gold and 100 BL of GNP thin films was found to be comparable, with evaporated gold coated columns demonstrating slightly better separation efficiencies. The deposition of ISAM SNP in µSPCs as stationary phase or anchoring sites for thin layer silane stationary phase incorporation would be an interesting follow-up.

References

1 S. E. Yancey, W. Zhong, J. R. Heflin, and A. L. Ritter, Journal of Applied Physics **99,** 034313 (2006).

2 A. D. Radadia, R. I. Masel, M. A. Shannon, J. P. Jerrell, and K. R. Cadwallader, Analytical Chemistry **80,** 4087 (2008).

3 N. Na, X. Cui, T. De Beer, T. Liu, T. Tang, M. Sajid, and J. Ouyang, Journal of Chromatography A **1218,** 4552 (2011).

4 G. E. Spangler, Journal of Microcolumn Separations **13,** 285 (2001).

5 H. M. McNair and J. M. Miller, *Basic gas chromatography* (John Wiley & Sons, 2011).

6 A. Ulman, Chemical reviews **96,** 1533 (1996).

CHAPTER 5 SUMMARY

In this dissertation, the fabrication of thin film ISAM GNP and SNP coatings using the LbL self-assembly technique and their application in IPMC electromechanical bending actuators and μGC devices were reported. More specifically, ISAM GNP were deposited on both sides of ionomer membranes as the CNC layers of the IPMC actuator; while ISAM SNP were incorporated inside the μTPCs either directly as adsorbent or as novel nanotemplate for a conventional polymer adsorbent, and inside the μGC columns as functionalization material. Besides, ISAM GNP were also applied to newly designed SPCs for incorporating thiols as the stationary phase. The processes of applying the LbL technique to deposit ISAM nanoparticle thin films on the planar surfaces and micro 3D structures of these devices were reported. The quality of the coating, as well as the device performance and modeling were also discussed. The key aspects covered in this dissertation are summarized in detail below, and future work that could be performed is also proposed.

5.1 LbL self-assembly used for ISAM nanoparticle thin film coating fabrication

All the thin film ISAM nanoparticle coatings used in the studies reported in this dissertation were fabricated via the conceptually simple, operationally straightforward, economical and versatile LbL self-assembly technique. By utilizing the Coulomb attraction force, layer-by-layer of positively and negatively charged materials dissolved in a liquid phase can be deposited on substrates with a wide range of configurations, resulting in a homogeneous and conformal coating with easy fine thickness control.

I reported a newly designed "zip-loc" frame to help prevent degradation of the GNP colloid during the LbL process. This improved the coating quality of the ISAM GNP CNC for the IPMC actuators, and resulted in a fabrication procedure with better cost and time efficiency. For the μGC devices, an approach combining LbL self-assembly and conventional photolithography process was developed to selectively deposit ISAM nanoparticles inside the micro 3D structure of these devices while leaving the top surface clean for the following sealing step. Moreover, a new LbL fabrication scheme was also proposed for the μGC devices whose features are too small for the regular LbL process. ISAM SNP thin films thus fabricated showed good conformal coating quality and thickness consistency.

5.2 The application of ISAM GNP thin films in IPMC bending actuators

5.2.1 Summary

IPMC actuators made from Nafion ionomer membrane as backbone, IL as electrolyte, and ISAM GNP CNC layers for extra ion storage were extensively studied. With high porosity and conductivity, a CNC provides more space for ions to accumulate on either side of the actuator while minimizing the potential drop in the CNC. By investigating the charge storage, bending curvature and blocked force of both anodic bending and cathodic bending, it was found that the GNP CNC significantly enhanced the performance of the IPMC actuator, and a thicker CNC generally generated larger bending curvature and blocked force.

Because the ion conductivity of a Nafion membrane closely relates to the water content, the RH of the environment also plays an important role in the performance of IPMC actuator. The higher RH, the more water adsorbed in the Nafion membrane and the faster the ions transport,

which results in a faster and larger bending. The incorporated water also brings along the electrolysis effect, which led to a modified equivalent circuit model to simulate the electrical property of the IPMC actuator. With a leakage resistor (relating to the electrolysis current) added to two branches of a parallel RC circuit (corresponding to anodic and cathodic bending), the charging and discharging behaviors were analytically deduced and tested by fitting the charging and discharging behavior of the IPMC actuators. The general agreement between the fitting parameters obtained showed the approximate validity of the proposed model.

To further validate the correlation between the microscopic cation/anion motion and macroscopic bidirectional actuation, the ion mobility of another IL (EMIMm-Bf_4) in a Nafion membrane, and the bending performance of IPMC actuators made from them were measured. It was discovered that, as the water content increases, the ratio of the diffusion coefficient of cations and anions dropped from above 1 to below 1. This corresponding transition was successfully observed in the bending tests of IPMC actuators prepared with the same configuration in the varying RH environment. With the confirmation of the relation between RH and the water adsorption in the actuator, the proposed causality between the ion motion within the actuator and its mechanical response under external voltage was demonstrated.

Besides Nafion, several newly synthesized ionomer membranes from the group of Prof. Tim Long were also reported in this dissertation as fabricated into actuators with ISAM GNP CNC. Comparable and even better performance was obtained from the IPMC actuators from them as compared to the ones made from Nafion membrane. They not only offered a wider selection of ionomer membrane backbone suitable for IPMC actuator fabrication, but also provide more control over several key parameters which affect the electrical and mechanical properties of the actuator.

5.2.2 Future work

The first and probably biggest improvement that could be applied to the current IPMC actuator design is to find a better outer electrode other than gold foil. Within the five-layer structure of the IPMC actuator, the gold foil electrode has the largest modulus and is the only one that does not contribute to the bending. Thus, to get a less dense and softer, but still highly conductive electrode would be beneficial to the actuation performance. For example, thin films of gold can be deposited onto outer surfaces of the actuator instead of hot pressing with gold foil. This could generate a thinner electrode with lower modulus. As a feasibility test, a Nafion membrane with GNP CNC and IL electrolyte was sputter coated with ~50 nm thick gold as outer electrodes on both sides. IPMC actuators made this way experienced smaller but faster bending. The smaller amplitude may result from electrolyte loss during the high vacuum sputtering procedure, though the much faster response could be useful to the high frequency AC application as discussed below.

All the work on the IPMC actuators reported in this dissertation concerned the response to a DC step input. However, the response to an AC input could also be valuable to investigate applications such as oscillators or even mimicking the wing vibration of insects. Above certain frequency, only the fast cations would be able to respond to the polarity oscillation of the input, while the slow anions basically would act like a nearly stable background. Example AC responses of an IPMC actuator (with gold foil outer electrode) with 100 BL GNP CNC and 40 wt.% EMIm-Tf IL to 0.5 Hz and 1.0 Hz 4 V square wave input can be watched in **Video 5.1** and **Video 5.2** multimedia files, respectively. As a preliminary study on alternate outer electrode, the Nafion IPMC actuator with 50 nm thick sputtered gold as outer electrode was tested with a 4 V AC square wave input at even higher frequency, and the oscillation response can be observed up

to a 20 Hz input (video can be watched in **Video 5.3** multimedia file), while the actuator with gold foil electrode did not showing response to the same input. With further optimization, this novel form of electrical-mechanical oscillation coupling could achieve a higher frequency with larger amplitude, and is worthy of a more extensive investigation.

And theoretically, although the proposed modified equivalent circuit model successfully showed general agreement with the electrical and mechanical fitting parameters, the actual IPMC actuator is far more complex and can be influenced by many factors. Thus, a more complex and detailed model also needs to be proposed and tested by numerical simulation in future work.

5.3 The application of ISAM SNP and GNP thin films in μGC devices

5.3.1 Summary

ISAM SNP thin film coatings are ideal for GC applications due to their large surface area and good thermal stability. The LbL self-assembly technique was found to be a simple and feasible approach to achieve an evenly distributed conformal coating on the micro 3D structure of μGC devices with good versatility and consistency.

An ISAM SNP coating applied in the μTPC cavity greatly increased the surface roughness. When used directly as adsorbent, it showed interesting pseudo-selective adsorbing ability with much higher retention to a very polar compound. Besides, a novel approach for enhancing the adsorption capacity of Tenax TA-coated μTPC using ISAM SNP as a surface template was also demonstrated. A promising improvement was attained under similar conditions over ones coated only with thin film Tenax TA. The better capturing ability was attributed to the larger surface

area provided by the ISAM SNP coating, thus increasing the interaction of analytes with the adsorbent surface.

The same SNP coating was also been incorporated into μGC separation columns with different configurations to be utilized as the stationary phase. The μGC columns (both regular and multicapillary) with this stationary phase showed good separation for alkanes with a wide range of boiling points with excellent consistency and repeatability. A more complex standard test mixture with ten VOCs was also successfully separated.

Moreover, two designs of unidirectional μWMCs were introduced for the first time to provide better resolution, plate numbers, retention times and chromatographic separations than the regular fixed dimensional column. A modified LbL self-assembly procedure was used to solve the inefficient coating problem in the very narrow channel and to process multiple serially-connected columns at the same time.

Besides SNPs, ISAM GNP thin films were also applied in modified SPC devices for thiol stationary phase incorporation. For comparison, evaporated gold was also deposited in the SPCs. The chromatographic performance of thiol functionalized 100 BL thin film ISAM GNP and evaporated gold was found to be comparable to evaporated gold coated columns demonstrating slightly better separation efficiencies. Moreover, thermodynamically both phases showed similar behavior, with evaporated gold film showing slightly better retention.

5.3.2 Future work

For the μGC devices with ISAM SNP thin film coatings as adsorbent or functionalization material, both the surface area and intra-granular porosity can be controlled by changing the size

and shape of the SNP. The current study has utilized SNP with an average diameter of 45 nm. There are other types of commercially-available SNP with 10-20 nm, 20-30 nm, and 70-100 nm average diameters, as well as in different shapes that can be explored for the adsorption and separation performance. Besides SNP, I also envision incorporating ISAM thin films of other nanoparticles, such as lead sulfide (PbS), titanium dioxide (TiO_2) or cadmium sulfide (CdS), and the investigation of their impact on the performance of μGC devices. The functionalization of different nanoparticles could also provide a unique opportunity for selective adsorption of species of interest or enable a more efficient separation for a certain range of gas compounds as well.